HZDR-087

HYDROGEN BURNING: STUDY OF THE $^{22}Ne(p,\gamma)^{23}Na$, $^{3}He(\alpha,\gamma)^{7}Be$ AND $^{7}Be(p,\gamma)^{8}B$ REACTIONS AT ULTRA-LOW ENERGIES

Marcell Péter Takács

Wissenschaftlich-Technische Berichte
HZDR-087 · ISSN 2191-8708

WISSENSCHAFTLICH-
TECHNISCHE BERICHTE

HZDR
HELMHOLTZ
ZENTRUM DRESDEN
ROSSENDORF

Wissenschaftlich-Technische Berichte
HZDR-087

Marcell Péter Takács

HYDROGEN BURNING: STUDY OF THE ^{22}Ne(p,γ)^{23}Na, ^{3}He(α,γ)^{7}Be AND ^{7}Be(p, γ)^{8}B REACTIONS AT ULTRA-LOW ENERGIES

HZDR

HELMHOLTZ
ZENTRUM DRESDEN
ROSSENDORF

Druckausgabe: ISSN 2191-8708

Elektronische Ausgabe: ISSN 2191-8716

Die elektronische Ausgabe erscheint unter Creative Commons License (CC BY 4.0):

https://www.hzdr.de/publications/Publ-27110

urn:nbn:de:bsz:d120-qucosa-233508

Die vorliegende Arbeit wurde sowohl als Dissertation an der Fakultät Mathematik und Naturwissenschaften der Technischen Universität Dresden sowie als Wissenschaftlich-Technischer Bericht des Helmholtz-Zentrum Dresden – Rossendorf mit der Berichtsnummer **HZDR-087** veröffentlicht.

2018

Herausgegeben vom

Helmholtz-Zentrum Dresden - Rossendorf

Bautzner Landstraße 400

01328 Dresden

Germany

TECHNISCHE UNIVERSITÄT DRESDEN

HELMHOLTZ ZENTRUM DRESDEN ROSSENDORF

Hydrogen burning: Study of the ^{22}Ne(p,γ)^{23}Na, ^{3}He(α,γ)^{7}Be and ^{7}Be(p,γ)^{8}B reactions at ultra-low energies

DISSERTATION

zur Erlangung des akademischen Grades

Doctor rerum naturalium (Dr. rer. nat.)

vorgelegt

der Fakultät Mathematik und Naturwissenschaften der Technischen

Universität Dresden

von

MSc. Marcell Péter Takács

geboren am 13. 02. 1989 in Debrecen, Ungarn

Verteidigt am 12.09.2017

Diese Dissertation wurde in der Zeit von September 2013 bis April 2017 an dem Institut für Kern- und Teilchenphysik der Technische Universität Dresden und dem Institut für Strahlenphysik am Helmholtz-Zentrum Dresden-Rossendorf angefertigt.

1. Gutachter: Prof. Dr. Kai Zuber
2. Gutachter: Prof. Dr. Paolo Prati
3. Gutachter: PD Dr. Daniel Bemmerer

The most remarkable discovery in all of astronomy is that the stars are made of atoms of the same kind as those on the earth.

Richard P. Feynman

Abstract

The neon-sodium cycle (NeNa cycle) of hydrogen burning is active in stars of the Asymptotic Giant Branch, in classical novae, and in supernovae of type Ia. The thermonuclear reaction rate of the ^{22}Ne$(p,\gamma)^{23}$Na reaction is determined by a large number of resonances, and it represents the most uncertain rate in the NeNa cycle.

This PhD thesis reports on an experiment to study tentative ^{22}Ne$(p,\gamma)^{23}$Na resonances at $E_p^{\rm lab} = 71$ keV and 105 keV, as well as the direct capture component of the reaction rate for $E_p^{\rm lab} \leq 400$ keV.

The measurements were performed deep underground at the Laboratory for Underground Nuclear Astrophysics - LUNA (Gran Sasso, Italy), taking advantage of the strong reduction in the cosmic ray induced background. The LUNA-400-kV electrostatic accelerator and a differentially pumped, windowless gas target of isotopically enriched ^{22}Ne gas were used. The γ-rays from the reaction were detected with a 4π bismuth germanate scintillator.

The data show upper limits on the strengths of the resonances at $E_p^{\rm lab} = 71$ keV and 105 keV of 5.8×10^{-11} eV and 7.0×10^{-11} eV respectively. The resonances at $E_p^{\rm lab} = 156.2$, 189.5 and 259.7 keV have been re-studied and show 20% higher strength than the literature. The present experiment did not show any evidence for the direct capture process at the low energies studied.

In addition to the experimental work at LUNA, the ^{3}He$(\alpha,\gamma)^{7}$Be and ^{7}Be$(p,\gamma)^{8}$B reactions were studied using the most recent solar neutrino data available. Based on the standard solar model and the experimentally measured fluxes of solar ^{7}Be and ^{8}B neutrinos, the astrophysical S-factors of both reactions were evaluated directly in the solar Gamow peak.

Zusammenfassung

Der Neon-Natrium-Zyklus (NeNa-Zyklus) des Wasserstoffbrennens tritt in Roten Riesensternen, klassischen Novae und Supernovae vom Typ Ia auf. Die thermonukleare Reaktionsrate der ^{22}Ne$(p,\gamma)^{23}$Na Reaktion ist von vielen Resonanzen bestimmt, und sie gilt als die unsicherste Rate in dem NeNa-Zyklus.

Die vorliegenden Dissertation berichtet über ein Experiment, zur Untersuchung von möglichen ^{22}Ne$(p,\gamma)^{23}$Na Resonanzen bei $E_p^{\rm lab} = 71$ keV und 105 keV und des ,,Direct Capture"-Prozesses für $E_p^{\rm lab} \leq 400$ keV.

Die Messungen sind tief unter Tage im ,,Laboratory for Underground Nuclear Astrophysics - LUNA" (Gran Sasso, Italien) durchgeführt worden, um die starke Reduzierung der kosmischen Strahlung auszunutzen. Der LUNA-400-kV Beschleuniger und ein fensterloses Gastarget, gefüllt mit ^{22}Ne-Gas wurden verwendet. Die γ-Strahlen von der ^{22}Ne$(p,\gamma)^{23}$Na Reaktion wurden mit einem 4π Bismutgermanat-Szintillator nachgewiesen.

Die Daten ergaben obere Schranken von 5.8×10^{-11} eV und 7.0×10^{-11} eV für die Stärken von Resonanzen bei $E_p^{\rm lab} = 71$ und 105 keV. Die Resonanzen bei $E_p^{\rm lab} = 156.2$, 189.5 und 259.7 keV wurden ebenfalls untersucht, und die Messungen zeigen 20% höhere Werte für die Resonanzstärke als die Literatur. In dem untersuchten Energiebereich wurde kein Beleg für einen ,,Direct Capture"-Prozess gefunden.

Außer der experimentellen Arbeit an LUNA wurden die Reaktionen ^{3}He$(\alpha,\gamma)^{7}$Be und ^{7}Be$(p,\gamma)^{8}$B mit Hilfe der Sonnenneutrinoflüsse untersucht. Anhand des Standard-Sonnenmodels und der gemessen Flüsse von ^{7}Be und ^{8}B Neutrinos wurde der astrophysikalische S-Faktor von beiden Reaktionen im solaren Gamow-Peak bestimmt.

The work described in Section 5.1 was already published in a peer-reviewed journal:

Marcell P. Takács, Daniel Bemmerer, Tamás Szücs, and Kai Zuber
Constraining big bang lithium production with recent solar neutrino data
Physical Review D 91 (2015) 123526

Contents

1 Introduction **13**

2 Astrophysics of the ^{22}Ne(p,γ)^{23}Na reaction **23**

3 Experimental setup for the ^{22}Ne(p,γ)^{23}Na study at LUNA **31**
3.1 LUNA 400 kV accelerator 32
3.2 Gas target system 33
3.2.1 Target chamber 35
3.2.2 Calorimeter 36
3.2.3 Density profile 37
3.2.4 Beam heating correction 41
3.3 BGO detector and DAQ 43
3.4 Detector efficiency 45

4 Results of the ^{22}Ne(p,γ)^{23}Na experiment at LUNA **50**
4.1 Detector background 51
4.2 Resonant capture reaction 54
4.2.1 71 keV resonance 55
4.2.2 105 keV resonance 61
4.2.3 156.2 keV resonance 64
4.2.4 189.5 keV resonance 68
4.2.5 259.7 keV resonance 71
4.3 Non-resonant capture reaction 75
4.4 Astrophysical reaction rate 87
4.5 Error analysis 92
4.5.1 Statistical uncertainties 92
4.5.2 Systematic uncertainties 93

5 Study of the *pp*-chain with the help of solar neutrinos **96**
5.1 S-factor of the ^{3}He(α,γ)^{7}Be reaction 97
5.1.1 Determination of S_{34} at the solar core temperature 98
5.1.2 Implications for the BBN reaction rate and production of ^{7}Li . 102
5.2 S-factor of the ^{7}Be$(p,\gamma)^8$B reaction 105

6 Discussion **111**
6.1 Discussion of the present new LUNA results 111
6.2 Discussion of solar neutrino based results 119

7 Summary **120**

A Tail contributions to the non-resonant S-factor **123**
A.1 Breit-Wigner cross section for sub-threshold resonances 123
A.2 Breit-Wigner cross section for broad resonances above the Coulomb threshold 124
A.3 Determination of $P_l(E)$ and $S_l(E)$ 124

B ^{22}Ne$(p,\gamma)^{23}$Na reaction rate (tabulated) **125**

C ^{3}He$(\alpha,\gamma)^{7}$Be reaction rate (tabulated) **127**

D Certificate of the ^{22}Ne target gas **129**

Bibliography **130**

List of Figures

1.1 Energy scheme of a charged particle induced nuclear reaction 14
1.2 Gamow peak for the ^{22}Ne$(p,\gamma)^{23}$Na reaction at T= 100 MK 17
1.3 *pp*-I-III chain of hydrogen burning 19
1.4 The three cold CNO cycles 20
1.5 Break-out reactions towards the hot CNO cycles 20
1.6 The NeNa and the MgAl cycle 22

2.1 Inner structure of an AGB star with Hot Bottom Burning 24
2.2 Low energy levels in the spectrum of ^{23}Na 26
2.3 Evaluations of the thermonuclear reaction rate of ^{22}Ne$(p,\gamma)^{23}$Na . . . 29

3.1 Overview of the Gran Sasso National Laboratory (Italy) 31
3.2 LUNA-400 accelerator 32
3.3 Schematic overview of the gas target system 34
3.4 Target chamber design with its dimensions 35
3.5 Calibration of the calorimetric current measurement 37
3.6 "Flute chamber" for pressure and temperature profile measurement . 38
3.7 Pressure profile in the gas target 38
3.8 Temperature profile in the target chamber 39
3.9 Gas density profile along the beam axis 41
3.10 BGO detector with target chamber 43
3.11 Cross section of the BGO detector 43
3.12 Scheme of the data acquisition system 44
3.13 Decay of an excited state E_x through two possible γ-cascades 46
3.14 Source holder for efficiency measurement 48
3.15 Modified end flange and positioning rod for efficiency measurement . 48
3.16 Efficiency as function of position, measured with a point-like ^{137}Cs radioactive source 49
3.17 Measured and simulated single sum spectra obtained on the $E_p^{\mathrm{lab}} =$ 278 keV resonance in ^{14}N(p,γ)^{15}O 49

4.1 4-phase experimental procedure 50
4.2 Natural background seen by the BGO detector in add-back mode . . 51
4.3 Beam induced background at $E_p^{\mathrm{ini}} = 165$ keV and 265 keV in argon gas 52
4.4 Illustration of the adopted background normalization approach 53
4.5 Experimental spectra at $E_p^{\mathrm{ini}} = 72.1$ keV 56
4.6 Experimental spectra at $E_p^{\mathrm{ini}} = 74.0$ keV 56
4.7 Experimental spectra at $E_p^{\mathrm{ini}} = 76.0$ keV 57
4.8 Experimental spectra at $E_p^{\mathrm{ini}} = 80.3$ keV 57
4.9 Upper limits on the strength of resonance E_p^{lab}= 71 and 105 keV . . . 60

4.10 Experimental spectra at $E_p^{\rm ini} = 105.5$ keV 62
4.11 Experimental spectra at $E_p^{\rm ini} = 110.5$ keV 62
4.12 Experimental spectra at $E_p^{\rm ini} = 115.5$ keV 63
4.13 Scan of the resonance at $E_p^{\rm lab} = 156.2$ keV 64
4.14 Experimental spectrum at $E_p^{\rm ini} = 163.9$ keV for the study of the resonance at $E_p^{\rm lab} = 156.2$ keV. 66
4.15 Comparison between the experimental NET and simulated spectra for the resonance at $E_p^{\rm lab} = 156.2$ keV 66
4.16 Simulated single-sum spectra for the resonance at $E_p^{\rm lab} = 156.2$ keV . 67
4.17 Scan of the resonance at $E_p^{\rm lab} = 189.5$ keV 68
4.18 Experimental spectra at $E_p^{\rm ini} = 196.4$ keV for the study of the resonance at $E_p^{\rm lab} = 189.5$ keV. 70
4.19 Comparison of experimental NET and simulated add-back peak for the resonance at $E_p^{\rm lab} = 189.5$ keV 70
4.20 Simulated single-sum spectra for the resonance at $E_p^{\rm lab} = 189.5$ keV . 71
4.21 Experimental spectra at $E_p^{\rm ini}$= 265.0 keV for the study of the resonance at $E_p^{\rm lab} = 259.7$ keV. 72
4.22 Simulated single-sum spectra for the resonance at $E_p^{\rm lab} = 259.7$ keV . 74
4.23 Comparison of the observed and simulated direct capture transitions at $E_p^{\rm ini} = 310$ keV 77
4.24 Simulated add-back detection efficiency for the direct capture process 78
4.25 Experimental spectrum at $E_p^{\rm ini} = 188.0$ keV 81
4.26 Experimental spectrum at $E_p^{\rm ini} = 205.0$ keV 81
4.27 Experimental spectrum at $E_p^{\rm ini} = 250.0$ keV 82
4.28 Experimental spectrum at $E_p^{\rm ini} = 310.0$ keV. 82
4.29 Contributions to the non-resonant S-factor from broad resonances near the proton threshold 85
4.30 Non-resonant S-factors of ^{22}Ne(p,γ)^{23}Na reaction 86
4.31 ^{22}Ne$(p,\gamma)^{23}$Na thermonuclear reaction rate 90
4.32 ^{22}Ne$(p,\gamma)^{23}$Na reaction rate from the LUNA-BGO phase, normalised to the STARLIB-2013 rate 91

5.1 Energy spectrum of solar neutrinos 97
5.2 The ^{3}He(α,γ)^{7}Be reaction and resulting two branches of solar neutrinos 98
5.3 Experimental cross section of the ^{3}He(α,γ)^{7}Be reaction, parameterized as the astrophysical S-factor. 99
5.4 Thermonuclear reaction rate of the ^{3}He$(\alpha,\gamma)^7$Be reaction 104
5.5 Experimental cross sections of the ^{7}Be$(p,\gamma)^8$B reaction, parametrized as the astrophysical S-factor. 106

6.1 Comparison of the experimental resonances strengths for the resonances at $E_p^{\rm lab} = 156.2$, 189.5 and 260 keV 116
6.2 Comparison of the LUNA-BGO and LUNA-HPGe reaction rate . . . 117
6.3 Comparison of the TUNL and LUNA-HPGe reaction rate 117
6.4 Comparison of the LUNA-BGO reaction rate to the previous compilations 118

List of Tables

2.1 ^{22}Ne$(p,\gamma)^{23}$Na resonance strengths values, important for AGB-HBB and classical novae . . . 30

3.1 Main parameters of the CAEN V1724 digitizer with their typical value 45
3.2 Properties of the radioactive calibration sources . . . 46

4.1 Common contaminant reactions in the gas target . . . 52
4.2 Experimental parameters for the resonance at $E_p^{\rm lab} = 71$ keV . . . 58
4.3 Registered events compared to the expected number of counts from the natural background . . . 58
4.4 Add-back detection efficiencies for the resonances at $E_p^{\rm lab} = 71$ and 105 keV . . . 60
4.5 Upper limits on the $\omega\gamma$ for the resonance at $E_p^{\rm lab} = 71$ keV . . . 60
4.6 Experimental parameters for the resonance at $E_p^{\rm lab} = 105$ keV . . . 61
4.7 Upper limits on the $\omega\gamma$ for the resonance at $E_p^{\rm lab} = 105$ keV . . . 63
4.8 Branching ratios for the resonance at $E_p^{\rm lab} = 156.2$ keV . . . 65
4.9 Branching ratios for the resonance at $E_p^{\rm lab} = 189.5$ keV . . . 69
4.10 Branching ratios for the resonance at $E_p^{\rm lab} = 259.7$ keV . . . 73
4.11 Experimental parameters for the resonances at $E_p^{\rm lab} = 156.2$, 189.5 and 259.7 keV . . . 74
4.12 Direct capture ^{22}Ne(p,γ)^{23}Na transitions at $E_p^{\rm ini} = 1.22$, 0.425 and 0.310 MeV . . . 76
4.13 ^{22}Ne(p,γ)^{23}Na non-resonant S-factor . . . 83
4.14 Parameters of the resonances near the proton threshold . . . 83
4.15 Input for ^{22}Ne(p,γ)^{23}Na reaction rate calculation . . . 88
4.16 Overview of the statistical and systematic uncertainties for the resonance strengths . . . 94
4.17 Overview of the statistical and systematic uncertainties for the derived S-factors . . . 95

5.1 Logarithmic partial derivatives . . . 101
5.2 Predicted solar neutrino fluxes from the SSM . . . 102
5.3 Determination of $S_{34}(0)$ from recent experimental data . . . 103
5.4 Estimated 1σ uncertainties of SSM model parameters and computed logarithmic partial derivatives . . . 108
5.5 $S_{17}(0)$ from recent experimental data . . . 110

6.1 Comparison of the most recent low energy $\omega\gamma$ values . . . 114
6.2 Branching ratios for the resonances at $E_p^{\rm lab} = 156.2$, 189.5, and 259.7 keV . . . 115

List of Symbols

Y	yield
$\omega\gamma$	resonance strength
$\sigma(E)$	reaction cross section
$S(E)$	astrophysical S-factor
$N_A\langle\sigma v\rangle$	thermonuclear reaction rate
Q	Q-value of a nuclear reaction
E_p^{ini}	initial proton beam energy
E_p^{lab}	proton energy (laboratory frame)
E_{target}	beam energy at the center of the target chamber (laboratory frame)
E_x	level energy (center-of-mass)
J^π	spin and parity of a level
λ	de Broglie wavelength
η_{eff}	add-back detection efficiency
ϵ	stopping power
t	time
q	electric charge
p	pressure
T	temperature
n	density

Chapter 1

Introduction

The stars have fascinated mankind from the very beginning of history, but for a long time it was not so evident that the Sun is one of them. Around 450 B.C, the Greek philosopher Anaxagoras already theorised that all the stars in the night sky are probably similar objects to the Sun, and only the vast distances make them look different. However, his idea got forgotten, and it was only a millennium later, when Giordanio Burno came again to the realization that the universe is infinitely large, and "fixed stars" are in fact suns. Unfortunately, this rather radical thought also led to his demise in the year 1600.

Only a couple of years later, the invention of the telescope by some Dutch opticians launched a whole new era, hallmarked by the names of Galilei, Kepler, Huygens and Newton. The shift from the geocentric to the heliocentric model was a huge step in the history of astronomy. While the celestial mechanics of the Solar system was explained by Newton's theory of gravity, it did not provide a direct confirmation that stars are suns, and vice versa. The final argument was then provided by Bessel in 1838, who successfully determined the distance between the Sun and another star (61 Cygni) by the method of parallax. The calculated distance was incredible huge, and thus confirmed the original idea of Anaxagoras.

By the end of the 19^{th} century, a lot was already known about the Sun, however, the origin of its heavenly fire was still a mystery. As Lord Kelvin pointed out, chemical burning in the classical sense would allow the Sun to shine only for a couple of thousand years. Even the more sophisticated idea of energy generation due to gravitational contraction suggested by Helmholtz failed to reproduce a reasonable lifetime for the Sun. It was only with the dawn of nuclear physics that the correct answer was found.

In 1917, Ernest Rutherford was doing various experiments at the University of Manchester, when he realised that he could produce hydrogen ions from air (nitrogen gas) by bombarding it with alpha particles from a radioactive source. This observation, which was in fact the first intentionally induced nuclear reaction, not only lead to the discovery of the proton, but opened a whole new chapter in physics. Three years later, in his precise measurement Francis William Aston concluded that the mass of the helium atom is slightly smaller than the sum of four hydrogen atom masses.

The significance of this discovery was then realized by Arthur Eddington, who speculated that the energy production of the Sun relies on the nuclear transformation of hydrogen into helium. Indeed, Eddington managed to come up with the right idea,

despite the fact that classically such fusion would not be possible: The protons are positively charged particles and therefore experience electrostatic repulsion. In order to induce a nuclear fusion between two protons, they have to be pushed so close together that their classical radii overlap. The amount of energy required is determined by the Coulomb potential, which can be expressed as

$$V_c = k_E \frac{q_1 q_2}{r} = k_E \frac{Z_1 Z_2 e^2}{r} \approx \frac{Z_1 Z_2}{r} 1.440 \text{ MeV fm} \tag{1.1}$$

where k_E is the Coulomb constant, $q_1 = Z_1 e$, $q_2 = Z_2 e$ are the electrical charges of the interacting nuclei, and r is the distance separating them [1]. As a typical physical radius of the proton, one can assume its root mean square charge radius, which is roughly 1 fm. This means that the minimal energy required to fuse two protons is about 1.4 MeV. The temperature of the solar core is $T_c = 16 \times 10^6$ K. If one imagines the Sun as a giant gas ball of hydrogen at temperature T_c, the typical proton energy can be estimated as the average kinetic energy of the gas particles based on the kinetic theory of ideal gases:

$$\langle E_{kin} \rangle = \frac{3}{2} k_B T \tag{1.2}$$

where k_B is the Boltzmann constant. Surprisingly, this calculation yields only $\langle E_{kin} \rangle \approx 2$ keV, which means the energy of the protons falls three orders of magnitude short. The Sun seems to be too cold, because the protons classically cannot cross the Coulomb-barrier (see Fig. 1.1).

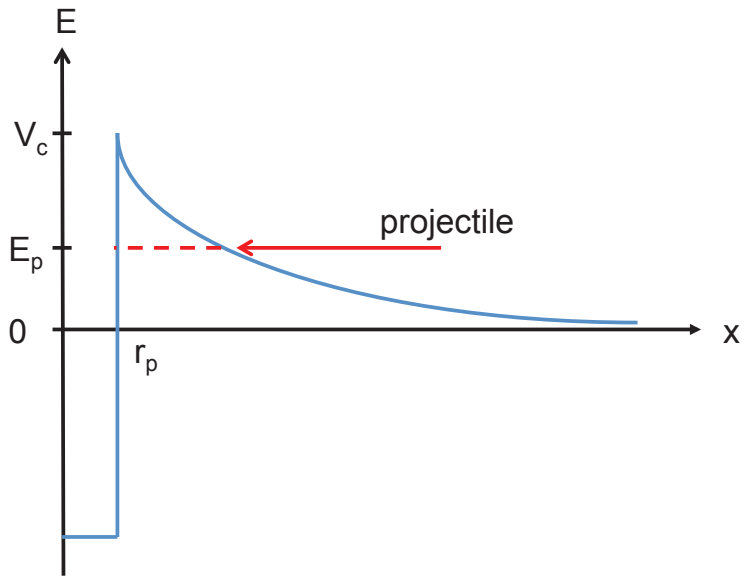

Figure 1.1: Energy scheme of a charged particle induced nuclear reaction: classically the reaction is only allowed if $E_p \geq V_c$, but in the framework of quantum mechanics the projectile can tunnel through the Coulomb barrier with a finite probability.

The way out from this dilemma was provided by G. Gamow in 1928 [2], who managed to find an explanation for the radioactive alpha decay by the introduction of the quantum mechanical tunnel effect. The same phenomenon which allows the alpha particles to exit the nucleus, grants the passing for the protons through the Coulomb barrier in the Sun. For the general case of charged particle induced nuclear

reaction, the tunneling probability (also known as the Gamow-factor) at zero angular momentum can be expressed as

$$P = e^{-2\pi\eta} \tag{1.3}$$

where $\eta = Z_1 Z_2 e^2/(\hbar\nu)$ is the Sommerfeld parameter with the atomic numbers of two interacting nuclides Z_1, Z_2, and the magnitude of their relative velocity v. In practice, the Sommerfeld parameter is usually approximated with the following numerical expression [3]:

$$-2\pi\eta = -31.29\ Z_1\ Z_2\ \left(\frac{\mu}{E}\right)^{1/2} \tag{1.4}$$

where μ is the reduced mass of the two-body system (consisting of masses m_1 and m_2) expressed in units of amu

$$\mu = \frac{m_1 m_2}{m_1 + m_2} \tag{1.5}$$

and E is the total kinetic energy of center-of-mass system in keV.

It is evident that the cross section of the nuclear reaction $\sigma(E)$ must be proportional to the Gamow-factor:

$$\sigma(E) \propto \exp(-2\pi\eta) \tag{1.6}$$

By definition, the cross section is the effective geometrical area that quantifies the likelihood of the nuclear reaction taking place. In the semiclassical description of nuclear reactions, this effective area is determined by the impact parameter of the two interacting nuclei, which is linked to the de Broglie wavelength of the particles in the center-of-mass frame: $\lambda = h/p$. (In the center-of-mass frame, the two-body system of target and projectile is characterised by only one de Broglie wavelength, because the magnitude of their momenta is equally p.) The cross section thus becomes

$$\sigma(E) \propto \pi\lambda^2 \propto \frac{1}{E} \tag{1.7}$$

where E is again the total kinetic energy of the target-projectile system in center-of-mass frame. Taking into account these properties of the reaction cross section, in nuclear astrophysics $\sigma(E)$ is usually expressed as follows

$$\sigma(E) = S(E)\frac{1}{E}\exp\left(-2\pi\eta\right) \tag{1.8}$$

In this way, the cross section is separated into three parts, from which the "nuclear" part is represented by $S(E)$, the so-called S-factor. Since most of the energy dependence due to kinematics (E^{-1}) and the Coulomb-barrier ($\exp(-2\pi\eta)$) is taken away, usually $S(E)$ has only a mild dependence on the energy.

With the help of the cross section, it is possible to express the rate of nuclear reactions in the stellar plasma where particles with relative velocity v and distribution $P(v)$ interact with each other

$$\langle\sigma v\rangle = \int \sigma(v)P(v)v dv \tag{1.9}$$

For non-degenerate plasmas, which are in thermal equilibrium at temperature T, $P(v)$ follows the well-known Maxwell-Boltzmann distribution

$$P(v) = P_{MB}(v) = \left(\frac{\mu}{2\pi k_B T}\right)^{3/2} \exp\left(\frac{-\mu v^2}{2k_B T}\right) 4\pi v^2 \tag{1.10}$$

which means that the number of particle pairs that are interacting with a relative velocity between v and $v + dv$ is

$$P_{MB}(v) \cdot dv = \left(\frac{\mu}{2\pi k_B T}\right)^{3/2} \exp\left(\frac{-\mu v^2}{2k_B T}\right) 4\pi v^2 dv \tag{1.11}$$

Since the cross section was expressed in Eq. 1.8 as a function of the energy, it is better to write also Eq. 1.9 as a function of energy. The conversion can be accomplished by noting that $E = \mu v^2/2$ and $dv/dE = 1/\sqrt{2E\mu}$

$$P_{MB}(E) \cdot dE = \frac{2}{\sqrt{\pi}}\left(\frac{1}{k_B T}\right)^{3/2} \exp\left(\frac{-E}{k_B T}\right) \sqrt{E} dE \tag{1.12}$$

Substituting this expression into Eq. 1.9 and integrating it over all possible energies the total reaction rate can be determined

$$\langle \sigma v \rangle = \int_0^\infty \sigma(E) \sqrt{\frac{2E}{\mu}} P_{MB}(E) dE = \sqrt{\frac{8}{\pi\mu}}\left(\frac{1}{k_B T}\right)^{3/2} \int_0^\infty \sigma(E) \exp\left(\frac{-E}{k_B T}\right) E dE \tag{1.13}$$

By using the definition of the S-factor (Eq. 1.8), the stellar thermonuclear reaction rate takes its final form

$$\langle \sigma v \rangle = \sqrt{\frac{8}{\pi\mu}}\left(\frac{1}{k_B T}\right)^{3/2} \int_0^\infty S(E) e^{-2\pi\eta} \exp\left(\frac{-E}{k_B T}\right) dE \tag{1.14}$$

As it was mentioned before, the S-factor has only a mild energy dependence, therefore the energy dependence of the integrand in Eq. 1.14 is determined by the interplay of the two exponential expressions: With increasing energy the tunnelling probability increases. On the other hand, the number of available particle pairs at a certain energy is decreasing, because of their Maxwell-Boltzmann statistics. The result of these two opposing tendencies is that nuclear reactions only take place in a limited interval of energy, the so-called Gamow peak.

The Gamow peak is usually described with the E_0 energy at which the integrand takes its maximum value, and its approximated Gaussian width Δ [1]:

$$E_0 = 0.1220\left(Z_1^2 Z_2^2 \mu T_9^2\right)^{1/3} \text{ [MeV]} \tag{1.15}$$

$$\Delta = \frac{4}{\sqrt{3}}\sqrt{E_0 k_B T} = 0.2368\left(Z_1^2 Z_2^2 \mu T_9^5\right) \text{ [MeV]} \tag{1.16}$$

Consequently, the cross section (or equivalently the astrophysical S-factor) has to be determined within the bounds of $E_0 - \Delta/2$ and $E_0 + \Delta/2$. However, it is important to note, that the smoothly varying picture of the cross section is not always the case. The presence of isolated narrow resonances might greatly enhance

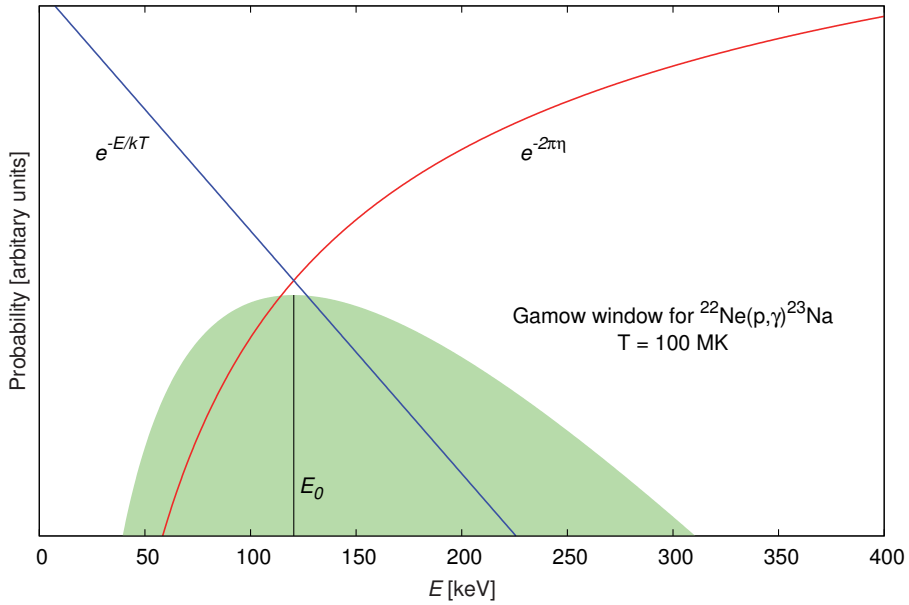

Figure 1.2: Gamow peak for the $^{22}\mathrm{Ne}(p,\gamma)^{23}\mathrm{Na}$ reaction at T= 100 MK, as product of the penetrability of the Coulomb barrier and the Maxwell-Boltzmann energy distribution

the cross section for certain energies. Therefore, Eq. 1.14 only describes one part of the picture, the non-resonant reaction rate.

A resonance can happen if the E_r center of mass energy of the projectile satisfies the following condition:

$$E_x = Q + E_r \tag{1.17}$$

where Q is the Q-value of the reaction and E_x is the energy of one of the excited states of the nucleus in the exit channel of the nuclear reaction. In the case of a resonance at E_r, the reaction rate has to be evaluated using the Breit-Wigner shape of the resonance

$$\sigma_{BW}(E) = \frac{\lambda^2}{4\pi}\frac{2J+1}{(2j_1+1)(2j_2+1)}(1+\delta_{12})\frac{\Gamma_a\Gamma_b}{(E-E_r)^2+(\Gamma/2)^2} \tag{1.18}$$

which is determined by the λ de Broglie wavelength of the projectile, the spins of the interacting particles (j_1, j_2) and the excited state (J), moreover the partial widths of the entrance and exit channels (Γ_a, Γ_b), and last but not least the total width of the resonance (Γ). This last quantity is defined as the sum of the widths of all possible decay channels: $\Gamma = \sum_i \Gamma_i$.

For narrow resonances ($\Gamma < E_r$), the expression of the reaction rate can be simplified, because the Maxwell-Boltzmann part of the integrand can be assumed to be constant over the width of the resonance [1]. Therefore, it can be evaluated at the resonance energy and moved in front of the integral:

$$\langle\sigma v\rangle_{res} = \sqrt{\frac{8}{\pi\mu}}\left(\frac{1}{k_BT}\right)^{3/2}\exp\left(\frac{-E_r}{k_BT}\right)E_r\int_0^\infty \sigma(E)_{BW}dE \tag{1.19}$$

The remaining integrand can be evaluated analytically:

$$\int_0^\infty \sigma(E)_{BW} dE = \frac{\lambda^2}{2} \frac{2J+1}{(2j_1+1)(2j_2+1)}(1+\delta_{12})\frac{\Gamma_a \Gamma_b}{\Gamma} \tag{1.20}$$

where it is customary to introduce the definition of the resonance strength $\omega\gamma$, which represents the integrated cross section.

$$\omega\gamma = \omega\frac{\Gamma_a \Gamma_b}{\Gamma} = \frac{2J+1}{(2j_1+1)(2j_2+1)}(1+\delta_{12})\frac{\Gamma_a \Gamma_b}{\Gamma} \tag{1.21}$$

Thus, the reaction rate for narrow resonance can be written as

$$\langle \sigma v \rangle_{res} = \left(\frac{2\pi}{\mu k_B T}\right)^{3/2} \hbar^2 \exp\left(\frac{-E_r}{k_B T}\right)\omega\gamma \tag{1.22}$$

where the definitions $\lambda_r = h/\sqrt{2\mu E_r}$ and $\hbar = h/2\pi$ have been used.

For stellar hydrogen burning, there are two major reaction paths depending on the star's initial mass - and thus its core temperature - which have to be studied [4].

In 1937, Weizsäcker suggested a reaction mechanism starting with the fusion of two protons into deuterium via the weak interaction [5], which hence became known as the *pp*-chain. The proper description of the process was developed one year later by Bethe and Crichfield [6]. As it is shown in Fig. 1.3, after the formation of ^{2}H another radiative proton capture takes place which leads to ^{3}He. In most cases the reaction chain proceeds from this point with the fusion of two ^{3}He nuclei via the ^{3}He(^{3}He,2p)^{4}He reaction. This is the *pp*-I chain.

However, if there is already some ^{4}He present, another reaction pathway, called the *pp*-II chain, becomes possible, where ^{7}Be is created. ^{7}Be is an unstable isotope and it decays into ^{7}Li by electron capture. The ^{7}Li nucleus then captures a proton and emits an alpha particle, leaving behind ^{4}He. The original ^{4}He necessary for the initiation of the *pp*-II is thus conserved, while similarly to the *pp*-I path one additional ^{4}He nucleus is obtained at the end. A third reaction sequence (*pp*-III) can be triggered via a (p,γ) reaction on ^{7}Be. In this case instead of ^{7}Li, the radioactive isotope of ^{8}B is created. The β^+ decay of ^{8}B results in ^{8}Be, which instantly decays into two ^{4}He nuclei. The net result of all three pp-chains is the same: four protons are converted into one ^{4}He.

The first generation of stars consisted only of hydrogen and helium produced by the Big Bang. Therefore, in their case the only possible way of hydrogen burning was provided by the above described *pp*-chain. On the other hand, from the second generation onwards stars could also use the ashes from the previous stars to engage in other ways of hydrogen burning. The so-called CNO cycles use the isotopes of carbon, nitrogen and oxygen as catalysts to produce ^{4}He. The first such catalytic cycle (CNO-I) was proposed by Bethe [7] and Weizsäcker [8] independently from each other, therefore it is often referred to as the Bethe-Weizsäcker-cycle:

$$^{12}\mathrm{C}(p,\gamma)^{13}\mathrm{N}(\beta^+\nu)^{13}\mathrm{C}(p,\gamma)^{14}\mathrm{N}(p,\gamma)^{15}\mathrm{O}(\beta^+\nu)^{15}\mathrm{N}(p,\alpha)^{12}\mathrm{C} \tag{1.23}$$

The result is the same as for the *pp*-chain, because four hydrogen nuclei are converted into one helium nucleus. However, there is an important difference: in case of the reactions of the *pp*-chain, the fusion process has to take place against a relatively low Coulomb barrier, while the CNO-cycle is characterised by an elevated

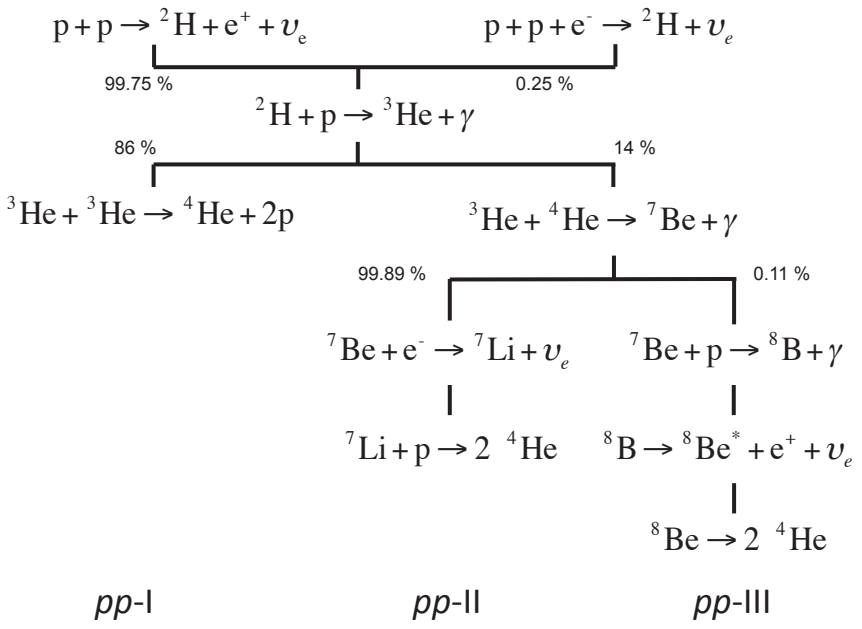

Figure 1.3: *pp*-I-III chain of hydrogen burning

Coulomb-repulsion due to the presence of elements with higher Z. This means that CNO cycle can only ignite at higher temperatures compared to the pp-chain. The temperature dependence of the overall energy production exhibits a much steeper slope for the CNO cycle ($\epsilon \propto T^{18}$), while for the *pp*-chain it follows a slower one ($\epsilon \propto T^4$). As a result, the CNO-I cycle will dominate energy production for core temperatures $T_c \geq 20 \times 10^6$ K. Since the core temperature has a direct link to the initial mass of the star, one can also say that stars with approximately $< 1.5 M_\odot$ initial mass will mainly burn hydrogen via the reactions of the *pp*-chain, while the heavier ones will rely on the CNO cycle.

If the core temperature increases further (50-100 MK) alternative CNO processes will become possible, however, it is important to note that the energy contribution of these side cycles to the total budget is lower than the one of the main Bethe-Weizsäcker-cycle. The second CNO cycle, which was first described in the famous B^2FH paper of stellar nucleosynthesis [4], branches off from the first cycle via the $^{15}N(p,\gamma)^{16}O$ reaction. Consequently, the cross section of this reaction at a certain stellar core temperature will determine the contribution to the energy production by the CNO-II reaction path:

$$^{15}N(p,\gamma)^{16}O(p,\gamma)^{17}F(\beta^+\nu)^{17}O(p,\alpha)^{14}N(p,\gamma)^{15}O(\beta^+\nu)^{15}N \tag{1.24}$$

By the radiative proton capture on ^{17}O, a third cycle becomes also possible which was first described by Rolfs and Rodney [9] in the mid-1970s. The path of this cycle goes through the radioactive ^{18}F isotope, that decays into ^{18}O, on which a (p,α) reaction takes place:

$$^{17}O(p,\gamma)^{18}F(\beta^+\nu)^{18}O(p,\alpha)^{15}N(p,\gamma)^{16}O(p,\gamma)^{17}F(\beta^+\nu)^{17}O \tag{1.25}$$

The above mentioned three reaction cycles traditionally referred to as the cold

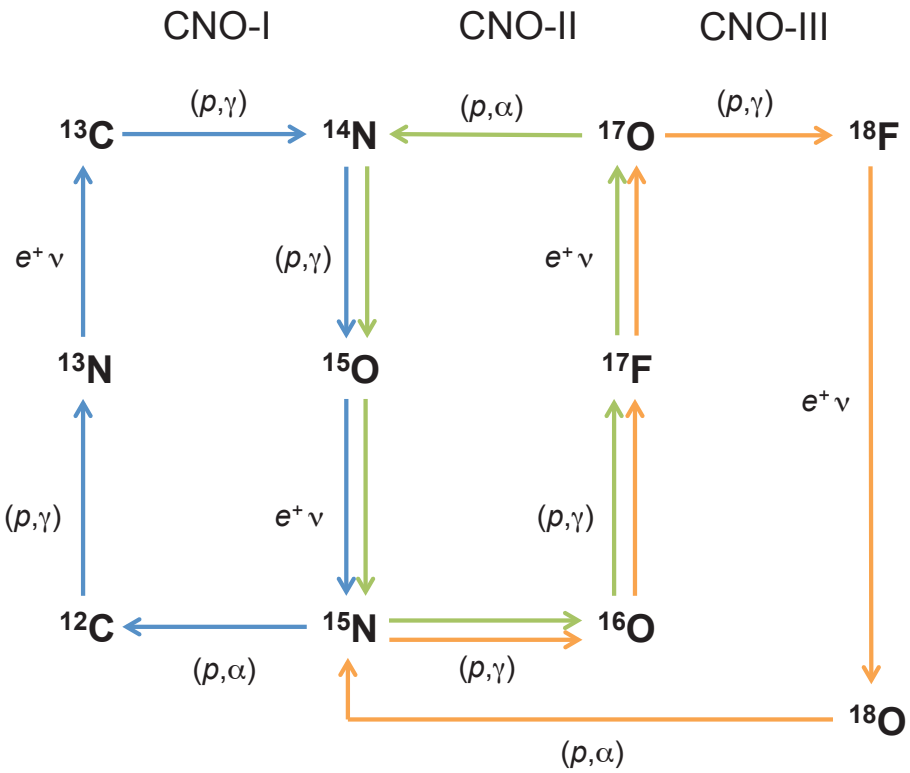

Figure 1.4: The three cold CNO cycles

CNO cycles, in order to set them apart from the so-called hot CNO-cycles, which require stellar core temperatures larger than 150 MK. The mechanism of these high order ways of hydrogen burning relies on the fact, that at these energies the (p, γ) reaction on ^{13}N (also ^{17}F and ^{18}F) can effectively compete with the radioactive β^+ decay. These breakouts from the cold-CNO cycles open up alternative pathways of catalytic hydrogen burning.

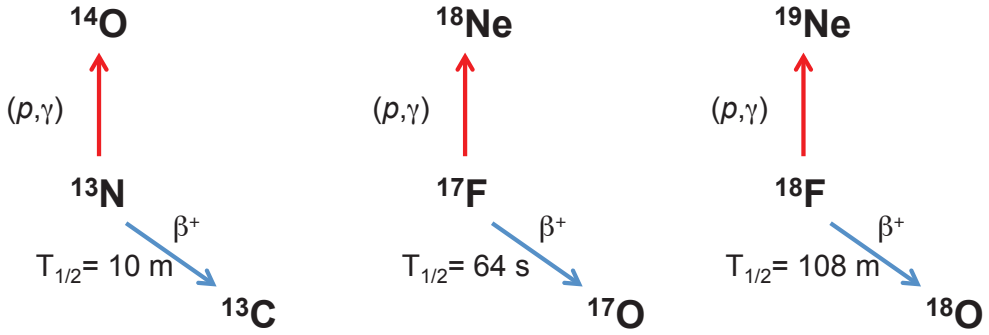

Figure 1.5: Break-out reactions towards the hot CNO cycles

While the stars with initial mass $M > 1.5 M_\odot$ produce energy mostly by the CNO processes, radiative proton capture processes can also happen on other isotopes of the stellar core, and form more exotic ways of catalytic hydrogen burning. The NeNa and MgAl cycles (shown in Fig. 1.6) function the same way as the CNO cycles do: they consist of a sequence of 3 (p, γ) reactions, 2 β^+ decays and one (p, α) reaction.

The NeNa cycle starts with a proton capture on the ^{20}Ne, followed by the

β^+ decay of ^{21}Na into ^{21}Ne. From ^{21}Ne the second proton capture reaction produces ^{22}Na, which acts as a branching point in the cycle. The competition between the β^+ / electron capture decay of ^{22}Na and the (p,γ) reaction opens up two possible reaction paths:

$$^{20}\mathrm{Ne}(p,\gamma)^{21}\mathrm{Na}(\beta^+\nu)^{21}\mathrm{Ne}(p,\gamma)^{22}\mathrm{Na}(p,\gamma)^{23}\mathrm{Mg}(\beta^+\nu)^{23}\mathrm{Na}(p,\alpha)^{20}\mathrm{Ne} \tag{1.26}$$

$$^{20}\mathrm{Ne}(p,\gamma)^{21}\mathrm{Na}(\beta^+\nu)^{21}\mathrm{Ne}(p,\gamma)^{22}\mathrm{Na}(\beta^+\nu)^{22}\mathrm{Ne}(p,\gamma)^{23}\mathrm{Na}(p,\alpha)^{20}\mathrm{Ne} \tag{1.27}$$

The link towards the MgAl cycle is provided by the ^{23}Na$(p,\gamma)^{24}$Mg reaction. Starting with proton capture on ^{24}Mg, the conversion of ^{1}H into ^{4}He proceeds in a similar fashion as in the NeNa cycle. As can be seen in Fig. 1.6, the cycle branches into two alternative reaction paths at the radioactive ^{26}Al isotope:

$$^{24}\mathrm{Mg}(p,\gamma)^{25}\mathrm{Al}(\beta^+\nu)^{25}\mathrm{Mg}(p,\gamma)^{26}\mathrm{Al}(p,\gamma)^{27}\mathrm{Si}(\beta^+\nu)^{27}\mathrm{Al}(p,\alpha)^{24}\mathrm{Mg} \tag{1.28}$$

$$^{24}\mathrm{Mg}(p,\gamma)^{25}\mathrm{Al}(\beta^+\nu)^{25}\mathrm{Mg}(p,\gamma)^{26}\mathrm{Al}(\beta^+\nu)^{26}\mathrm{Mg}(p,\gamma)^{27}\mathrm{Al}(p,\alpha)^{24}\mathrm{Mg} \tag{1.29}$$

Due to the even higher Coulomb barrier, the NeNa and MgAl cycles represent only a negligible addition to the total energy production. Their true importance lies in the synthesis of elements between ^{20}Ne and ^{27}Al, where they have a considerable impact.

With the scheme of stellar hydrogen burning laid out, the task falls to the experimentalist to provide precise cross section data in the astrophysically relevant energy range for the model calculations. The fact that the reactions take place at much lower energies than the Coulomb barrier, pushes the cross sections to the nano- or femtobarn region. In this sense, the energy production in stars is very inefficient. The only reason why they can still shine is their immense mass, which allows a reasonable number of reactions to take place even at these low cross sections. In the laboratory, however, it is hard to gather enough statistics at stellar energies within a practical time frame. In addition to this, the signal under study often gets simply buried under the background caused by environmental radioactivity or by cosmic radiation.

In principle, it is possible to measure the cross section at higher energies, where the cross section is higher, and then extrapolate to the Gamow peak. This approach, however, has a number of pitfalls and might lead to completely wrong results. The key to measure in the astrophysically relevant energy range is to improve on the statistics by radically reducing the number of background events (several orders of magnitude). This could be achieved by a careful choice of materials with low natural radioactivity, and most importantly by relocating the experiment to a deep underground location, where the effect of the cosmic rays is considerably reduced by the rock overburden.

This thesis is intended to improve the available knowledge on stellar hydrogen burning by adopting two different approaches: The first part of this work is dedicated to the experimental study of the ^{22}Ne$(p,\gamma)^{23}$Na reaction at the Laboratory for Underground Nuclear Astrophysics (LUNA), while in the second part an indirect idea is explored using the latest available neutrino fluxes and the Sun as nuclear laboratory to constrain the S-factors of the ^{3}He$(\alpha,\gamma)^{7}$Be and ^{7}Be$(p,\gamma)^{8}$B reactions at solar temperatures.

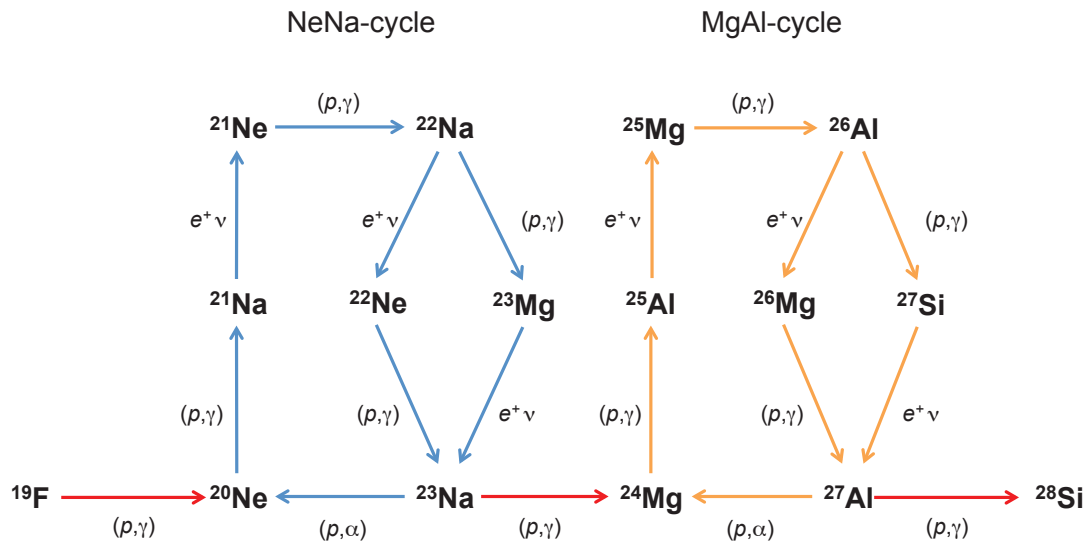

Figure 1.6: High order catalytic cycles of the hydrogen burning: the NeNa and the MgAl cycle

Chapter 2

Astrophysics of the ^{22}Ne(p,γ)^{23}Na reaction

The NeNa cycle represents a way of catalytic hydrogen burning. Recent astronomical observations regarding the chemical composition of globular clusters have drawn attention to its impact on nucleosynthesis. Globular clusters are spherical concentrations of stars, usually found in the halo of our galaxy. Such systems consist of thousands (sometimes millions) of stars, which due to their close proximity are assumed to share a similar chemical composition, and to have been formed at approximately the same time. The average age of some globular clusters is estimated to be at least 10 billion years, which means that these gravitationally bound systems contain some of the oldest stars (mostly low mass Red Giants) in the Milky Way.

Recent astronomical measurements using high resolution optical spectroscopy revealed that stars inside globular clusters are not as uniform as it was traditionally believed: not only the stars inside the cluster belong to multiple generations [10], but the abundances of elements of the CNO, NeNa and MgAl cycles show considerable variations from star to star [11]. Most interestingly, there is a puzzling anti-correlation between the abundance of O and Na [12]. In order to create such anti-correlation, both the CNO and the NeNa cycle have to be active in the stellar interior [13]. This requirement, however, is in contradiction with the rather low core temperature of the currently observed stars in globular clusters. Consequently, the abundance variations must originate from the ashes of previous generations of stars.

There are several possible astrophysical sites for such a "self-enrichment" scenario: Asymptotic Giant Branch (AGB) stars [14–16], fast rotating massive stars [17], supermassive stars [18] and massive stellar binary system [19]. Currently, AGB stars with $M > 4M_{\odot}$ represent the most promising candidate: they effectively pollute the interstellar medium with material created in the so-called Hot Bottom Burning (HBB) process.

The AGB stars represent the second red giant phase of stellar evolution, which occurs after core helium burning but before the ignition of carbon burning. Thus, they are characterised by an inert C-O core, which is surrounded by shells of He- and H-burning and a convective envelope. Depending on the mass of the AGB star, the convective envelope can extend to different depths. For stars with $M > 4M_{\odot}$, the bottom of the convective zone produces an overlap with the outer hydrogen burning shell of the core. The H-shell provides enough energy that within this overlap region radiative proton capture reactions are initiated on the material of the

convective envelope. This process is called Hot Bottom Burning (HBB) [20].

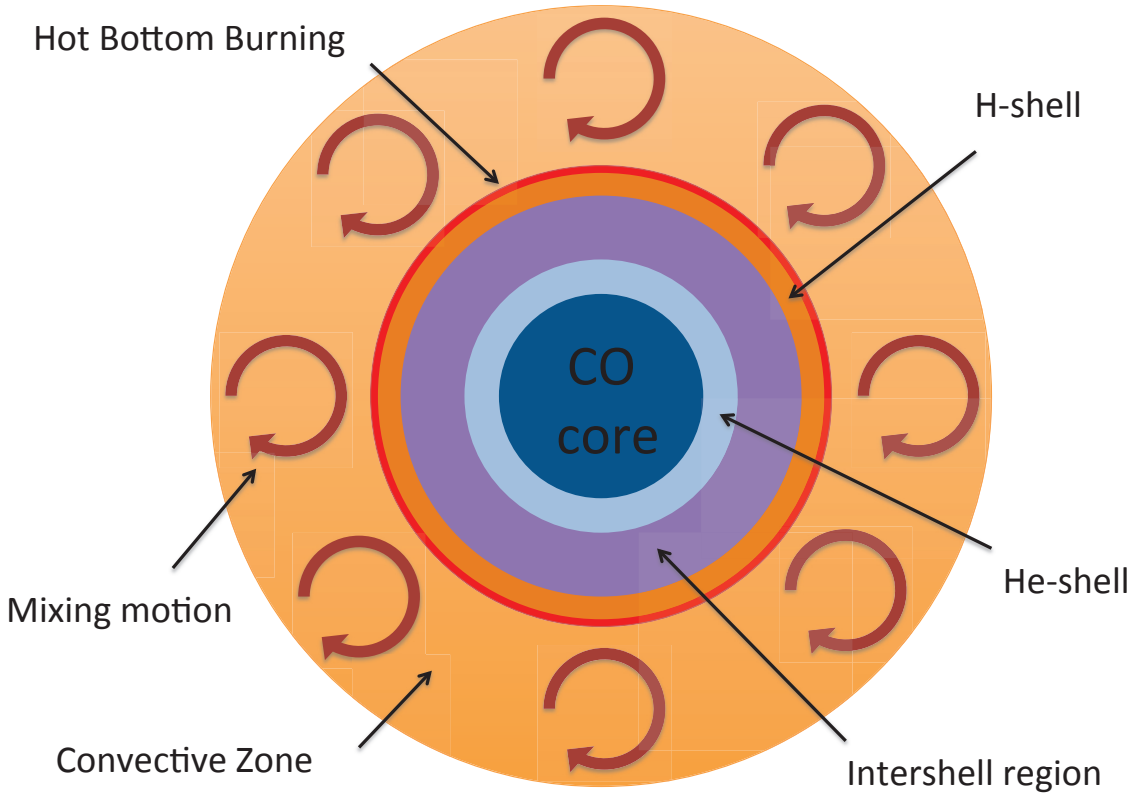

Figure 2.1: Inner structure of an AGB star with Hot Bottom Burning

The nucleosynthesis in HBB has a great impact on the surface chemical abundances of AGB stars. Due to the convective mixing motion, its products are effectively transported from the bottom of the convective envelope to the stellar surface. The temperatures in HBB are considered high enough ($T \approx 100$ MK), that the NeNa-cycle is also activated, which could lead to an increase in the abundances of Na, Al and Mg on the surface, from where it could be carried away by stellar winds. This, in combination with the oxygen depleting effect of the CNO-II cycle, might count for the O-Na anticorrelation observed in globular clusters.

In addition to HBB in AGBs, the NeNa cycle is also active in explosive scenarios such as classical novae and supernovae of type Ia. Classical novae develop from a binary system of two main-sequence stars, where it is required that one of binary companions is a star with mass $M < 13M_{\odot}$, so that after its red giant phase it will end up as white dwarfs. Depending on its initial mass and thus its last burning stage (helium- or carbon-burning) the star might form a carbon-oxygen (CO) or an oxygen-neon (ONe) white dwarf. Meanwhile, the second star can stay either on the main-sequence or develop into a red giant.

Due to its extreme gravity, the white dwarf will draw hydrogen rich material from its larger companion through the first Lagrangian point, and increase its mass by accretion. If the accretion rate is slow ($< 10^{-8} M_{\odot}$/yr), the hydrogen will gradually accumulate on the surface. As the new material is slowly compressed to degenerate conditions, its temperature will become high enough to ignite hydrogen burning via the CNO-cycle. Since degenerate matter does not expand as its temperature rises,

the burning cannot regulate itself, and it will result in a thermonuclear runaway with temperatures 0.15 GK $< T <$ 0.45 GK. The explosion blows away the accreted envelope of the white dwarf, but it is not powerful enough to fragment the massive core. Therefore, the whole process can repeat itself several times. Consequently, nova explosions can very effectively enrich the interstellar media with material processed through the CNO, NeNa, and MgAl cycles.

Supernovae of type Ia can result either from white dwarf - white dwarf mergers, or from a scenario similar to the above described one. In the latter case, the accretion rate is higher than for classical novae, and the white dwarfs increases its mass up to the Chandrasekhar limit (about 1.44 $M_{\odot}$). At this point the electron degeneracy pressure cannot outbalance the gravitation any more, and it starts to collapse. The compressional heating fires up nuclear fusion reactions, leading to a violent type Ia supernova explosion, which eventually disrupts the white dwarf. During the explosion temperatures higher than 1 GK are reached, enabling high order processes of hydrogen burning.

In order to estimate the impact of the NeNa cycle in the above mentioned astrophysical scenarios, one has to have precise information on the rate of the nuclear reactions involved. The reactions with the most uncertain reaction rate in the temperature range of interest are the ^{22}Ne$(p,\gamma)^{23}$Na and ^{23}Na$(p,\gamma)^{24}$Mg reactions [21, 22]. This thesis focuses on the ^{22}Ne$(p,\gamma)^{23}$Na reaction.

In the NeNa cycle, ^{22}Ne is produced by the β^+ decay of radioactive ^{22}Na ($T_{1/2}$ = 2.6027 yrs). As it was recently shown [23], for temperatures present in AGBs and supernovae of type Ia ($T >$ 70 MK), proton capture on ^{22}Na may bypass its radioactive decay. Because of this bypass, ^{22}Ne is excluded from the catalytic cycle, thus its destruction via the ^{22}Ne$(p,\gamma)^{23}$Na reaction is not compensated anymore. However, ^{22}Ne is still very abundant in the above mentioned scenarios, because in helium burning it is produced on the ashes of the CNO cycle via the ^{14}N$(\alpha,\gamma)^{18}$F$(\beta^+\nu)^{18}$O$(\alpha,\gamma)^{22}$Ne reaction chain [24].

The present uncertainty on the ^{22}Ne$(p,\gamma)^{23}$Na reaction rate results in six orders of magnitude uncertainty in the ^{22}Ne yield of an ONe nova explosion. In case of a CO nova, the variation of ^{22}Ne yield is "only" two orders of magnitude. On the other hand, about one order of magnitude uncertainty propagates also into the abundance of elements from ^{22}Ne to ^{27}Al [25]. The ^{22}Ne$(p,\gamma)^{23}$Na reaction can also affect the nucleosynthetic outcome of type Ia supernova explosions, because during the pre-explosion phase, when temperatures are still $T <$ 0.6 GK it might deplete ^{22}Ne [26], which may have consequences in the production of ^{18}O, ^{23}Na and ^{24}Na [27]. Moreover, as it was recently pointed out [28], the ^{22}Ne$(p,\gamma)^{23}$Na reaction rate might even have its implications for the core-collapse supernovae, since the ^{22}Ne nucleus also acts as a neutron source for the neutron capture nucleosynthesis (s-process and r-process) via the ^{22}Ne$(\alpha,n)^{25}$Mg reaction.

The ^{22}Ne$(p,\gamma)^{23}$Na reaction (Q = 8794.11 keV) is characterized by a large number of resonances. As can be seen in Fig. 2.2, the thermonuclear reaction rate in case of the AGB stars and classical novae is determined by the resonances below 480 keV center-of-mass energy, while resonances at higher energies become important for the nucleosynthesis in type Ia supernovae. Until the last couple of years, most of the information regarding the lowest energy resonances ($\leq$ 400 keV) originated from indirect measurements using the ^{22}Ne$(^3$He$,d)^{23}$Na reaction [29, 30].

However, the interpretation of such indirect data is not without ambiguities. Al-

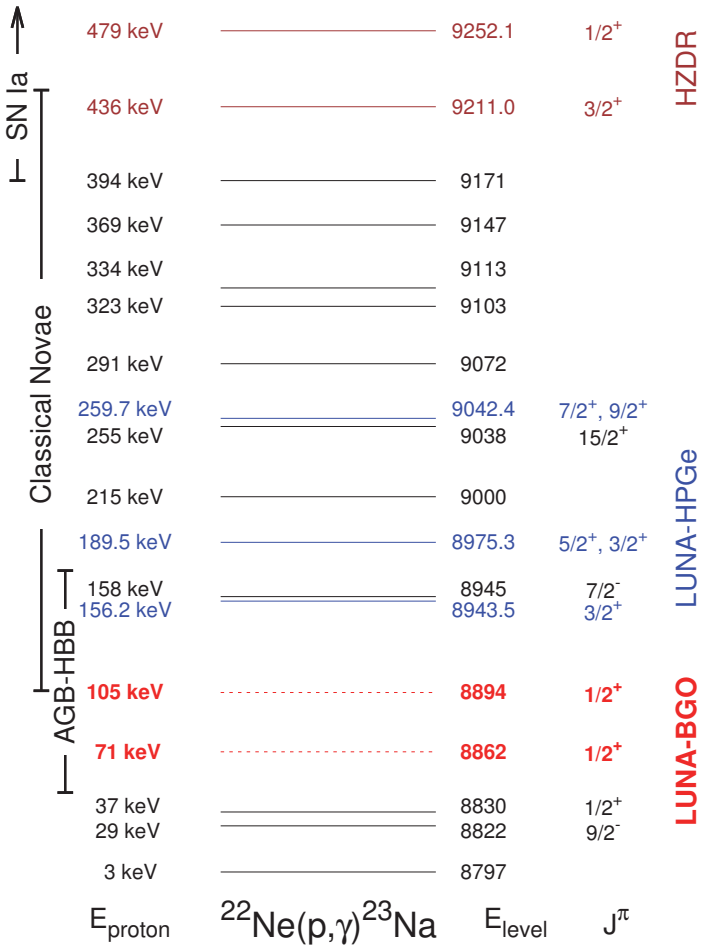

Figure 2.2: Low energy levels in the spectrum of ^{23}Na and their relevance for different astrophysical scenarios. Level energies are taken from [31–33]. The three newly discovered resonances from the previous LUNA experimental campaign [33] are shown in blue, while the two lowest energy points from the measurement at HZDR [34] are plotted in brown. The two low energy resonances shown in red represent the main focus of this thesis (the second LUNA experimental campaign).

ready, the analysis of the deuteron spectra obtained by magnetic spectrometers is not straightforward due to background effects and the presence of contaminant peaks. Moreover, in order to obtain the corresponding resonance strength, knowledge of spin assignment and the partial widths is required (see Eq. 1.21).

These difficulties are well illustrated by the levels at 8862 and 8894 keV. These resonances corresponding to a proton energy of 71 and 105 keV, respectively, were first reported in 1971 by Powers *et al.* [29]. However, they were labeled as tentative, because their signature in the $(^3\mathrm{He}, d)$ spectrum was not clear. Thirty years later Hale *et al.* [30] used the same technique to study the spectrum of ^{23}Na. Despite the lower background and higher resolution, neither of the two levels was observed. A spin/parity assumption was made (denoting both states as $J^\pi = \frac{1}{2}^+$) in order to obtain an upper limit on their resonance strength.

Implementing a direct measurement at such low energies is often more challenging (if possible at all) than an indirect approach, but it does have the advantage that no information is required on the spin and parity of the levels in order to obtain

the resonance strength. The only requirement is that the resonance under study should be narrow - meaning that its total width Γ is considerably smaller than the total energy loss of the proton beam inside the target ΔE. (For more details refer to Section 4.2.)

Already in 1982, efforts were made [35] to measure the ^{22}Ne$(p,\gamma)^{23}$Na low energy resonances ($E_p^{\mathrm{lab}} = 70 - 355$ keV) in this way. Unfortunately, none of the expected resonances were directly observed and only upper limits were provided on the resonance strengths. Thus, for more than three decades the low lying resonances seemed to be inaccessible via direct measurements.

In 2015 a breakthrough was achieved by the Laboratory for Underground Nuclear Astrophysics (LUNA), located in Gran Sasso, Italy. The LUNA collaboration reported a successful observation of the resonances at $E_p^{\mathrm{lab}} = 156.2$, 189.5, 259.7 keV along with their resonances strengths [33]. The key to the success was the experiment's deep underground location. Due to the shielding provided by the 1400 m overburden of the Gran Sasso massive, the cosmic ray induced background is six orders of magnitude lower than at the surface.

The experimental setup was based on a differentially pumped windowless gas target system utilizing isotopically enriched (99.9%) ^{22}Ne gas. The gas pressure in the target chamber was kept at 1.5 mbar by a feedback valve system. In order to minimize the gas consumption, the gas pumped away was collected and after chemical purification was led back to the target chamber. The proton beam was provided by a single-ended 400 kV electrostatic accelerator, with beam intensities up to 250 μA. The beam reached the target chamber through a series of collimators with decreasing diameter, where the induced gamma photons were detected by two large high purity germanium detectors, placed at 90° and 55° with respect to the beam axis. Due to the large number of secondary electrons induced in the target gas, the beam current was determined by a calorimetric approach.

In the energy range of $E_p^{\mathrm{lab}} = 70 - 300$ keV all previously suspected resonances [32] were investigated, but a clear signature was only found for the above mentioned three resonances. Since the spin/parity assignment of the corresponding levels in ^{23}Na is still under debate [31], it was assumed that the gamma photons from the (p,γ) reaction are emitted isotropically, and thus the weighted average of the measurements by the two HPGe detectors under different angles were accepted as final result.

The obtained resonance strength for $E_p^{\mathrm{lab}} = 156.2$, 189.5, 259.7 keV resonances were consistent with the previously reported direct upper limits [35]. On the other hand, there was, interestingly, a strong discrepancy with the indirect upper limits reported in the literature. In case of the tentative resonances at $E_p^{\mathrm{lab}} = 71$, 105 and 215 keV no clear evidence was found, but their upper limits could be reduced by up to three orders of magnitude.

Parallel to the low energy measurements at LUNA, the strength of several higher energy resonances (436, 479, 639, 661, and 1279 keV) contributing to the nucleosynthesis in supernovae of type Ia, was also remeasured at the 3 MV tandetron of the Helmholtz-Zentrum Dresden-Rossendorf, Germany [34]. The resonances at 436 and 479 keV are in the overlap energy region between supernovae and classical novae, as shown in Fig. 2.2.

In addition to the efforts made by LUNA, the TUNL group (Triangle Universities Nuclear Laboratory) has recently also measured the strength of resonances at

$E_p^{\rm lab}$ = 156.2, 189.5, 436 and 479 keV. The new data were included in the PhD thesis of K. J. Kelly at University of North Carolina [36]. Most recently, the results of the same experiment were also published as a paper in Physical Review C [37]. However, the reported $\omega\gamma$ for the resonance at $E_p^{\rm lab}$ =156.2 keV had been considerably revised from $(5.9 \pm 0.7_{\rm stat} \pm 1.0_{\rm sys}) \times 10^{-7}$ to $(2.03 \pm 0.18_{\rm stat} \pm 0.35_{\rm sys}) \times 10^{-7}$ eV.

Using the newly obtained direct experimental data on low energy resonances, both the LUNA collaboration and the TUNL group redetermined the thermonuclear reaction rate of ^{22}Ne$(p,\gamma)^{23}$Na in the energy range important for hot bottom burning in AGB stars and classical novae [37,38]. In Fig. 2.3, the two new rates are compared to the previous NACRE [21] and STARLIB-2013 [39] compilations. All compilations are in a relatively good agreement for temperatures $T \geq 0.3$ GK. On the other hand, large discrepancies are evident below 0.3 GK.

These temperatures correspond exactly to the energy range where the strengths of the low energy resonances (71, 105, 156.2, 189.5, 215, 259.7 keV) have an impact on the reaction rate. In the NACRE compilation from 1999, these resonances were considered with their at the time known upper limits from the experiments of Görres *et al.* [35, 40]. These values were higher than the ones provided by the LUNA experiment, thus the estimated central curve of the reaction rate is also considerably higher. On the other hand, the updated reaction rate by LUNA and its smaller uncertainty fits well within the large error margin of the NACRE rate.

The evaluation provided by the STARLIB group also uses the data from [35], but updates the upper limits on the resonances at $E_p^{\rm lab}$ = 29, 37, 156.2 and 259.7 keV with the newer results from Hale *et al.* [30]. One more important difference is that in this compilation the resonances at 71, 105 and 215 keV are considered as non-existent. Consequently, they do not contribute to the error budget. This explains why uncertainty of the STARLIB narrows down around 0.08 GK, which is exactly the energy range corresponding to the 105 keV resonance. The difference between the LUNA and STARLIB rates are mostly due to the three newly discovered resonances. The new, precise resonance strength values greatly reduced the rate uncertainty between 0.1 and 0.3 GK. The enhancement of the rate itself in this region is dominated by the new strength of the 156.2 keV resonance, which proved to be more than one order of magnitude stronger than previously believed. Last but not least, similar to the NACRE compilation, in the LUNA rate all low energy resonances are considered with their upper limits, which leads to a higher rate at low temperatures.

The reaction rate by TUNL is an updated version of the STARLIB-2013 implementing the new experimental data on resonances at $E_p^{\rm lab}$ = 156.2, 189.5 and 436 keV [37]. Due to the higher $\omega\gamma$ values measured, the TUNL rate is slightly higher than the one by LUNA for temperatures above 0.14 GK. On the other hand, in case of $T \leq 0.14$ GK, the TUNL rate is considerably lower than the LUNA rate due to the fact that the tentative resonance at $E_p^{\rm lab}$ = 71 and 105 keV are excluded from the compilation. Below 0.6 GK, the STARLIB-2013 and TUNL data predicts the same rate.

The present doctoral thesis was motivated by these large discrepancies among the various thermonuclear reaction rate compilations below 0.2 GK. Since the description of AGB stars with respect to the nucleosynthesis in the NeNa-cycle is mainly limited by our knowledge on the low-lying resonances at $E_p^{\rm lab}$ = 71 and 105 keV, the determination of their resonance strength (or alternatively the further reduction of

the present upper limits on $\omega\gamma$) is of paramount importance. Therefore, shortly after the completion of HPGe-based measurements in 2014, the LUNA collaboration continued the study of ^{22}Ne$(p,\gamma)^{23}$Na reaction in a second experimental campaign taking advantage of a high-efficiency BGO detector in near 4π geometry.

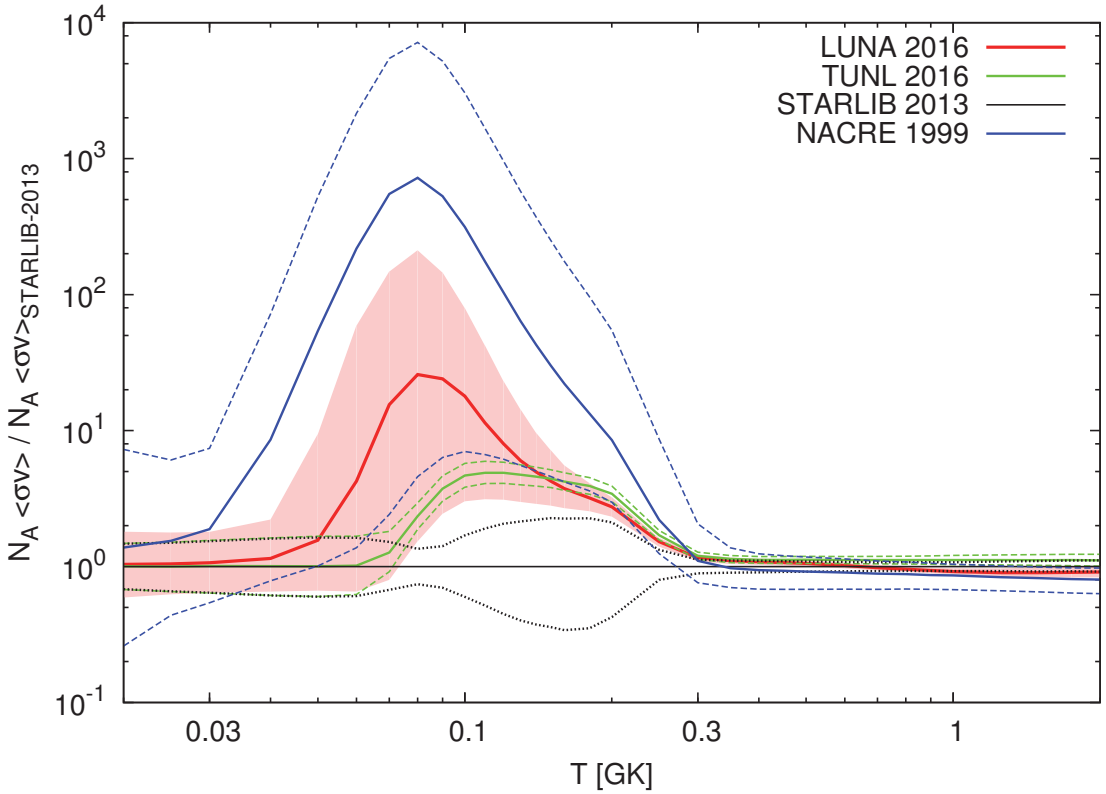

Figure 2.3: Different evaluations of the thermonuclear reaction rate of ^{22}Ne$(p,\gamma)^{23}$Na normalised to the STARLIB-2013 rate. In case of the LUNA-HPGe rate [38], the red area represent the rate uncertainty, while in case of the NACRE [21], STARLIB-2013 [39] and TUNL [37], it is indicated by the dashed lines with the same color.

Table 2.1: ^{22}Ne$(p,\gamma)^{23}$Na resonance strengths values, important for AGB-HBB and classical novae - adopted in different reaction rate calculations

	Resonance strength $\omega\gamma$ [eV]							
$E_p^{\rm lab}$ [keV]	NACRE [21]		STARLIB-2013 [39]		TUNL [37]		LUNA-HPGe [38]	
29	-		$\leq 2.6 \times 10^{-25}$	[30]	$\leq 2.6 \times 10^{-25}$	[30]	$\leq 2.6 \times 10^{-25}$	[41]
37	$(6.8 \pm 1.0) \times 10^{-15}$	[40]	$(3.1 \pm 1.2) \times 10^{-15}$	[30]	$(3.1 \pm 1.2) \times 10^{-15}$	[30]	$(3.1 \pm 1.2) \times 10^{-15}$	[41]
71	$\leq 4.2 \times 10^{-6}$	[40]	-		-		$\leq 1.5 \times 10^{-9}$	[33, 38]
105	$\leq 0.6 \times 10^{-6}$	[40]	-		-		$\leq 7.6 \times 10^{-9}$	[33, 38]
156.2	6.5×10^{-7}	[40]	$(9.2 \pm 3.7) \times 10^{-9}$ a)	[30]	$(2.03 \pm 0.40) \times 10^{-7}$ b)	[37]	$(1.48 \pm 0.10) \times 10^{-7}$	[33, 38]
189.5	$\leq 2.6 \times 10^{-6}$	[35]	$\leq 2.6 \times 10^{-6}$	[35]	$(2.32 \pm 0.32) \times 10^{-6}$	[37]	$(1.87 \pm 0.06) \times 10^{-6}$	[33, 38]
215	$\leq 1.4 \times 10^{-6}$	[35]	-		-		$\leq 2.8 \times 10^{-8}$	[33]
259.7	$\leq 2.6 \times 10^{-6}$	[35]	$\leq 1.3 \times 10^{-7}$	[30]	$\leq 1.3 \times 10^{-7}$	[30]	$(6.89 \pm 0.16) \times 10^{-6}$	[33, 38]
291	$\leq 2.2 \times 10^{-6}$	[35]	$\leq 2.2 \times 10^{-6}$	[35]	$\leq 2.2 \times 10^{-6}$	[35]	$\leq 2.2 \times 10^{-6}$	[35]
323	$\leq 2.2 \times 10^{-6}$	[35]	$\leq 2.2 \times 10^{-6}$	[35]	$\leq 2.2 \times 10^{-6}$	[35]	$\leq 2.2 \times 10^{-6}$	[35]
334	$\leq 3.0 \times 10^{-6}$	[35]	$\leq 3.0 \times 10^{-6}$	[35]	$\leq 3.0 \times 10^{-6}$	[35]	$\leq 3.0 \times 10^{-6}$	[35]
369	-		$\leq 6.0 \times 10^{-4}$	[30]	$\leq 6.0 \times 10^{-4}$	[30]	$\leq 6.0 \times 10^{-4}$	[30]
394	-		$\leq 6.0 \times 10^{-4}$	[30]	$\leq 6.0 \times 10^{-4}$	[30]	$\leq 6.0 \times 10^{-4}$	[30]
436	0.07 ± 0.02	[42]	0.065 ± 0.015	[43]	0.088 ± 0.010	[37]	0.079 ± 0.006	[34]
479	0.49 ± 0.13	[42]	0.45 ± 0.1	[43]	0.583 ± 0.043	[44]	0.594 ± 0.038	[34]

a) Contrary to Hale *et al.* [30], in STARLIB-2013 [39] $C^2S = 0.0011$ was adopted based on Hales PhD thesis

b) Originally $\omega\gamma = (5.9 \pm 0.7_{\rm stat} \pm 1.0_{\rm sys}) \times 10^{-7}$ eV was reported in the PhD thesis of K. J Kelly (University of North Carolina) [36]

Chapter 3

Experimental setup for the ^{22}Ne(p,γ)^{23}Na study at LUNA

The Laboratory for Underground Nuclear Astrophysics (LUNA) is located in the Gran Sasso National Laboratory (LNGS), Italy, where due to the 1400 m overburden of rocks the background induced by cosmic muons is six orders of magnitude lower than on the surface [45]. The neutron background is also significantly reduced, by about three orders of magnitude. These conditions provide an excellent environment for measurement of nuclear cross sections at astrophysical energies.

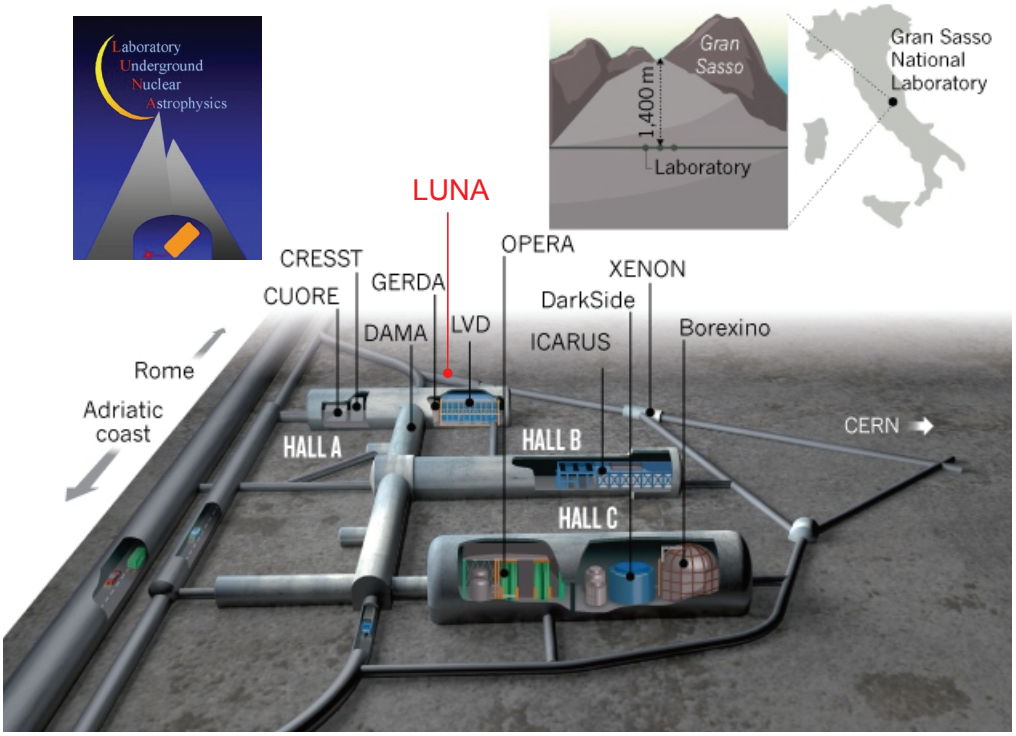

Figure 3.1: Overview of the Gran Sasso National Laboratory (Italy)

3.1 LUNA 400 kV accelerator

The beam for the LUNA experiments is supplied by a 400 kV single-ended electrostatic accelerator which was produced by High Voltage Engineering Europe. The accelerator is embedded in a 2 m^3 steel tank, filled with a gas mixture of N_2 (75%), CO_2 (20 − 25%) and SF_6 (1 − 5%). The high voltage terminal is charged by an inline Cockcroft-Walton generator equipped with an RC filter at its output. In order to further improve the stability of the high voltage, an active feedback loop based on a chain of resistors is also incorporated. The accelerator features a radio-frequency ion source, which is directly mounted on the accelerator tube. The ion source can provide either proton or alpha beams. In both cases, the maximum beam intensity is about 500 μA.

Figure 3.2: LUNA-400 accelerator

At astrophysical energies below the Coulomb barrier, the cross sections exhibits an exponential energy dependence (see Chapter 1), therefore, a precise knowledge of the beam energy and its stability is of paramount importance. The accelerator was calibrated using the non-resonant capture reaction $^{12}C(p,\gamma)^{13}N$ [46]. The obtained calibration function is the following:

$$E_p^{\mathrm{ini}} = (0.9933 \pm 0.0002) \cdot (TV + PV)\frac{\mathrm{keV}}{\mathrm{kV}} - (0.41 \pm 0.05)\ \mathrm{keV} \qquad (3.1)$$

where TV stands for the terminal voltage of the accelerator, while PV is the voltage applied to the anode of the ion source. The statistical uncertainty of the beam energy is 0.3 keV, and it is dominated by the systematic uncertainty on the Q-value of the $^{12}C(p,\gamma)^{13}N$. The statistical uncertainty due to the beam spread is only about 0.1 keV. Moreover, the beam energy also has an excellent long term stability, which is better than 5 eV/h [46].

In the currently used layout, there are two beam lines in the LUNA laboratory; one of them is used with a conventional solid target, while the other one accommodates a differentially pumped, windowless gas target system. With the help of two 45° analysing magnets the beam can be guided in either of the two beam lines. The beam parameters are afterwards tuned so that the beam current loss on the series of collimators inside the beam line is minimal.

3.2 Gas target system

Many nuclear physics experiments rely on the use of solid targets. However, for nuclear astrophysics where the cross sections are small and the beam energies are low, they might not represent the best choice: If the target material is not solid in its elemental form, one has to use its compounds or an implanted target, which may lead to some difficulties: e.g. the degradation of the target under intense bombardment of the beam. Instability, or uncertainties in the chemical composition are also common problems. Moreover, the straggling of the beam in the solid material decreases the precision of the beam energy.

In order to avoid these problems, the ^{22}Ne(p,γ)^{23}Na LUNA experiment was based on a differentially pumped gas target system, which consists of three pumping stages (see Fig. 3.3). The stages are connected by long apertures ($L_{AP3} = 80$ mm, $L_{AP2} = 80$ mm, $L_{AP1} = 40$ mm), whose diameter decreases along the path of the beam ($d_{AP3} = 25$ mm, $d_{AP2} = 15$ mm, $d_{AP1} = 7$ mm). Since these apertures also act as collimators to define the beam geometry, water-cooling is necessary.

The first pumping stage is connected to a large volume Leybold RUVAC WS 2001 roots pump, which removes most of the gas ($\geq 90\%$). The second pumping stage is evacuated by three Leybold turbo molecular-pumps: two TMP1000 pumps on the side (TP2L, TP2R), and one higher capacity TMP1500 pump in the center (TP2M). The negligible amount of gas that still reaches the third pumping stage is collected by a Leybold TURBOVAC 361 pump. All pumps are backed by a Leybold RUVAC WS 501 roots pump, which is connected via an additional ECODRY pump to the laboratory's exhaust pipeline. The well chosen impedance of the apertures allows it to maintain pressures in the mbar range inside the target chamber, while in the third stage of the pumping system the pressure is in the 10^{-7} mbar range.

The experiment relies on the use of isotopically enriched (99.9%) ^{22}Ne gas (the certificate can be found in Appendix D). This isotope of neon only amounts to 9.25% of natural neon gas. In order to conserve the expensive target gas, the gas target system was designed to be able to operate also in recirculation mode. In this mode, the output of RUVAC WS 501 pump is redirected to an Alcatel ACP28 dry vacuum pump, which collects the gas and pumps it through a chemical getter into a reinforced stainless steel buffer of 1 liter volume. From here the gas can be let back into the target chamber.

The use of a chemical getter is necessary, since it is difficult to keep a vacuum system completely free from leaks. Thus, the repeated use of the same amount of gas would otherwise lead to loss of its purity. In order to avoid such effects, a MonoTorr II PS4-MT3-R-2 purifier with PF4-C3-R-2 chemical getter cartridge designed for noble gases was incorporated into the setup. The purification process is based on the fact that noble gases are chemically passive: The cartridge is filled with a special mixture of metal powder, that is heated up to high temperatures.

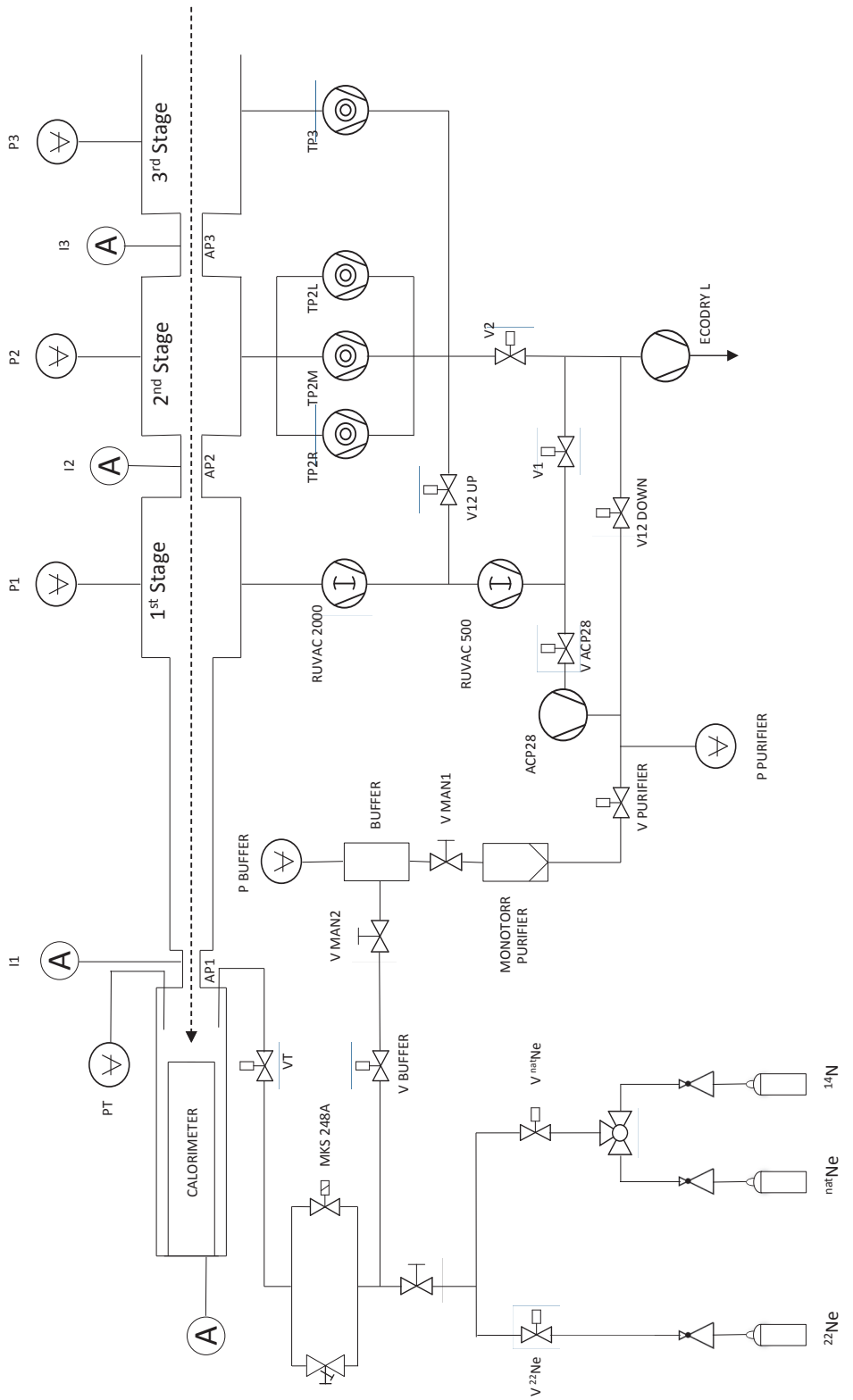

Figure 3.3: Schematic overview of the gas target system (beam enters from the right)

When the target gas passes through this filter, any contamination of nitrogen or oxygen will be bound inside it by chemical reaction, while noble gases - such as neon - are let through.

3.2.1 Target chamber

The target chamber was manufactured from stainless steel and it has a total length of 475 mm with an inner diameter of 54 mm. The actual reaction volume is only 108 mm long, because the rest of the space inside the target chamber is occupied by a copper beam stop, which is used for the calorimetric measurement of the beam current. (See the following section.) The beam enters the target chamber through a 40 mm long water-cooled copper collimator which has an inner diameter of 7 mm. The connection to the gas target system is provided by a 360 mm long stainless steel tube with 36 mm inner diameter.

The target chamber was electrically insulated from the rest of the gas target system, therefore it could be used as a Faraday-cup to measure the beam current. The target collimator was also insulated from the chamber itself. In this way, these two current readings could be used to optimize the beam transport and focusing in vacuum. Since the bombarding by the beam liberates a large number of secondary electrons from the copper beam stop, which could compromise the charge collection, the chamber was equipped with a secondary electron suppression electrode. This thin, ring shaped electrode was positioned just after the target collimator and a negative potential of typically -100 V was applied to it.

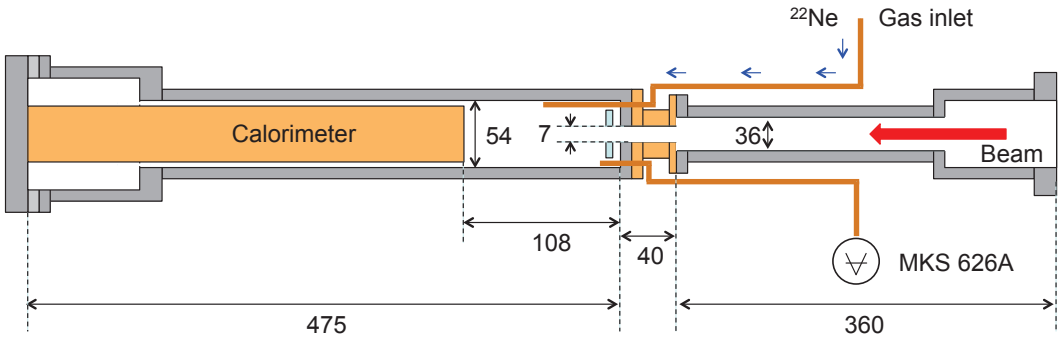

Figure 3.4: Target chamber design with its dimensions in mm (beam enters from the right)

The gas entered the chamber through a copper pipeline on its front side near the collimator. For the better distribution of the gas, the pipe extended to the center of the chamber. A similar, but slightly shorter copper pipeline was used for the pressure measurement. The pressure inside the chamber was monitored by an MKS Baratron 626A type absolute pressure transducer. The gauge was read out by an MKS Valve Controller unit, which also regulated an MKS 248A flow control valve (thermal leak) on the gas inlet. This feedback system was used to keep the target pressure stable during the measurement.

Due to the limited dynamic range provided by the thermal leak, the pressure first had to be adjusted by the two manual valves to a level which was about 0.4 mbar lower than the desired target pressure. The final target pressure was then set on the MKS Valve controller unit.

3.2.2 Calorimeter

If there is gas inside the target chamber, an electrical beam current monitoring cannot be used, because of the vast amount of secondary electrons liberated from the gas. Therefore, a calorimetric measurement method was adopted, based on the fact that the beam deposits most of its energy in the beam stop, thus heats it up during the irradiation. In order to quantify this effect, a constant temperature gradient calorimeter was constructed: The front side (also called hot side) of the calorimeter consists of a thick copper disk, which is heated by a number of power resistors up to 70°C. The back side (cold side) of the calorimeter was cooled by circulation of cooling liquid with subzero temperature.

During the experiment two different cold side temperatures were used: Since the precision of the calorimetric current measurement benefits from a large temperature gradient between the hot and cold side, the temperature of the cooling liquid was initially set to −20°C. This led to a cold side temperature of −3°C. Unfortunately, this led to some condensation issues and ice build-up near the electrical connections of the calorimeter. From this reason, the temperature of the cooling liquid was increased to −5°C, which resulted in a milder cold side temperature of 7°C.

Commercially available Pt100 platinum resistance temperature sensors were used to monitor the temperature of the calorimeter. (Their name refers to the fact that at 0°C they have a nominal resistance of 100 Ω.) Three of these sensors were mounted on the hot side in different positions, while on the cold side only one Pt100 was used. The readout of the sensors was done by a LabView system utilising NI CompactRIO hardware. Based on the temperature readings, the system also regulated the power supply of the heating resistors so that the temperature of the hot side stayed constant.

In the absence of the beam, the resistors have to deposit a power of W_0 to keep the hot side at 70°C. During an irradiation, however, the beam also contributes to the heating of the beam stop, therefore the power supply has to provide less power W_I. The power deposited by the beam is the difference between these two values:

$$W_{beam} = W_0 - W_I \tag{3.2}$$

With the help of W_{beam}, the beam intensity can be expressed as the following:

$$I = \frac{W_{beam}}{E_p - \Delta E} q_e \tag{3.3}$$

where E_p is the proton beam energy before entering the gas target, ΔE is the total beam energy loss up to the surface of the calorimeter, and q_e is the electric charge of the bombarding particles.

In order to check the validity of the beam intensities obtained by the calorimetric approach, the calorimeter was calibrated against the Faraday-cup method, where the beam current was measured by an ORTEC 439 digital current integrator and an ORTEC 994 counter. The measurements were carried out in vacuum. The calibration curve was determined separately for the two different cold side temperatures, but since obtained results were in good agreement with each other, the two datasets were combined to obtain the final calibration:

$$W_{elec} = (1.040 \pm 0.008) W_{calo} \tag{3.4}$$

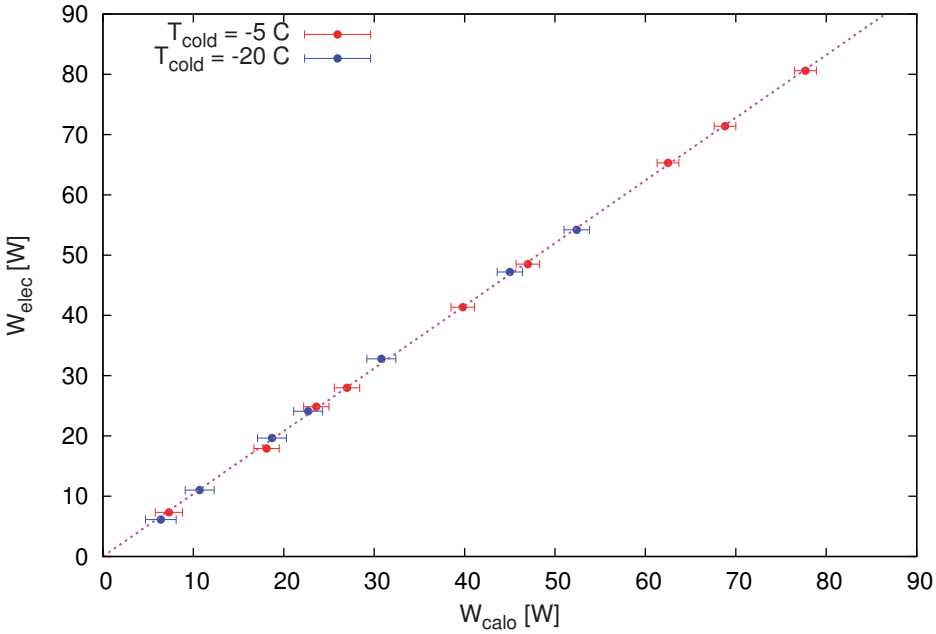

Figure 3.5: Calibration of the calorimetric current measurement

3.2.3 Density profile

For a gas target system, the knowledge of the gas density profile inside the target is crucial for the interpretation of the experimental yield data. According to the ideal gas law, the density of an ideal gas can be determined by the measurement of its temperature and pressure:

$$n = \frac{N}{V} = \frac{p}{kT} \tag{3.5}$$

For this purpose, a modified version of the original target chamber was designed. This so called "flute chamber" was identical to the original target chamber in its dimensions, but had seven additional KF25 flanges welded on its side. Four of these flanges were mounted on the chamber part, while the other three were on the interconnection tube between the chamber and first pumping stage of the gas target system. The flanges could accommodate either pressure or temperature sensors. In addition to this, three holes were drilled on the side of the 4 cm long target collimator, which made it possible to study the pressure drop inside the collimator. They are labelled as measurement point K1, K2 and K3. Due to the limited space available, the pressure gauges could not be directly mounted on these measurement points. Therefore, an about 30 cm long, thin copper pipeline was soldered to each measurement point on the collimator. These copper pipes ended in KF25 flanges, so that the pressure gauges could be connected easily.

For the pressure measurement four pressure sensors were used: two MKS Baratron 626A absolute pressure transducers with 10 torr (13.3 mbar) range (0.25% accuracy), and two Pfeiffer CMR 363 ceramic capacitive gauges with 10 mbar range (0.20% accuracy). The Baratrons were used in combination with the MKS Valve Controller unit, while the Pfeiffer gauges were connected to a Pfeiffer MaxiGauge controller unit. As with the actual target chamber, one of the MKS Baratrons was

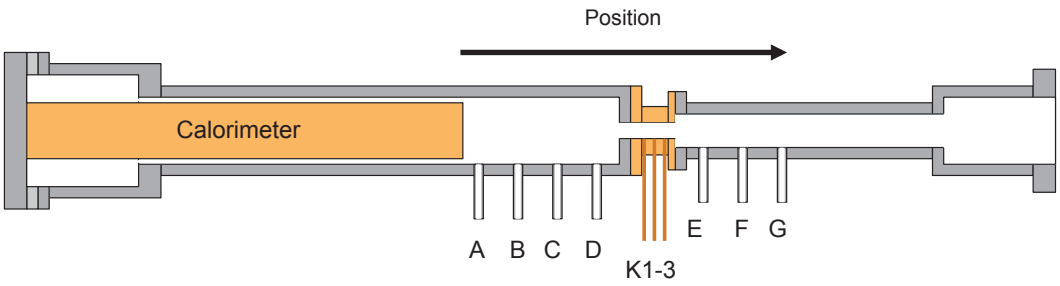

Figure 3.6: "Flute chamber" for pressure and temperature profile measurement (drawing is not to scale)

mounted on the copper pipeline which serves as a reference point for the pressure measurement during the experiment, while the rest of the gauges was moved around on the flanges A-G to map the pressure inside the target chamber. At a time, only one sensor was moved, which made the intercalibration of the measurements possible. In order to avoid venting the chamber each time a pressure sensor was moved, manual valves were mounted on all flanges of the flute chamber. The pressure profile was studied in 0.5 mbar steps from a nominal target pressure of 0.5 mbar to 5 mbar using enriched ^{22}Ne gas.

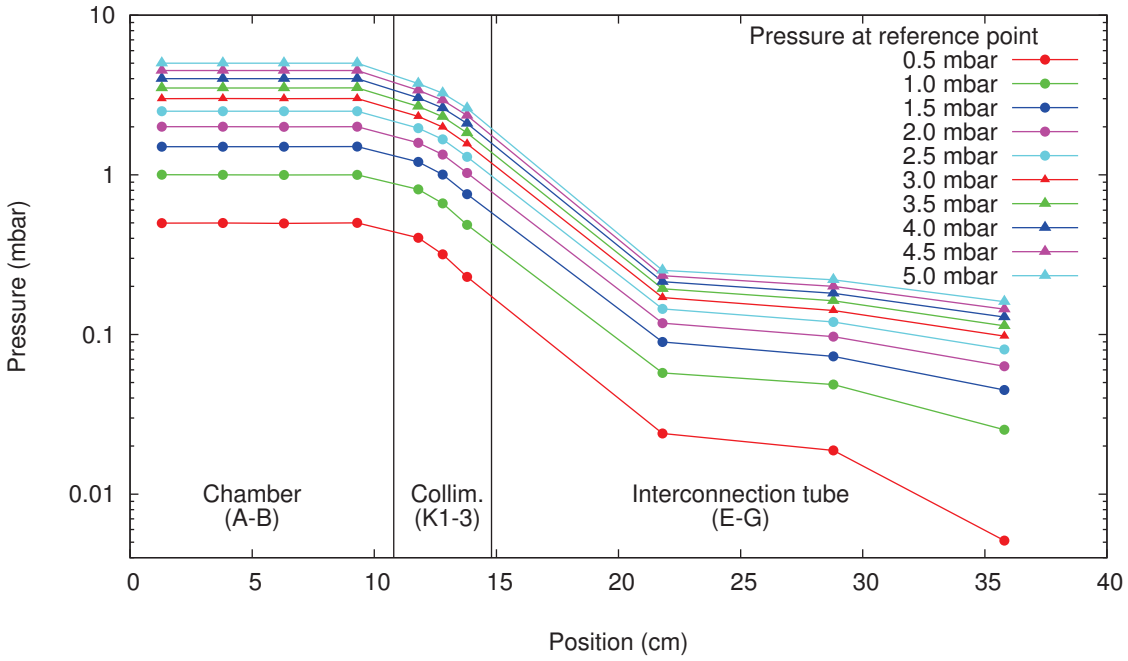

Figure 3.7: Pressure profile in the gas target. The lines are just to guide the eye.

As can be seen in Fig. 3.7, the pressure profile inside the chamber is flat, with almost no fluctuations. The agreement between the four pressures measured inside the chamber and the reference pressure was better than 0.5%. Between the two ends of the collimator the pressure drops about one order of magnitude, then it slowly decreases towards the first pumping stage of the gas target system. The general shape of the pressure trend is similar at all nominal pressures. The overall uncertainty of the pressure profile was estimated to be 1%.

Due to the presence of the calorimeter and water cooled collimator the temper-

ature inside the chamber cannot be expected to be constant even without beam. The front face (hot side) of the calorimeter is kept at 70°C by a LabView controlled system, while the temperature of the collimator is maintained at around 13°C by the circulation of cooling water. Moreover, the heat transport in the chamber is also affected by the amount of gas inside, which could lead to a different temperature gradient at different target pressures. Therefore, a detailed study of the temperature profile had to be carried out in the same nominal pressure range (0.5 mbar to 5 mbar).

For the temperature measurements, the already mentioned Pt100 sensors were used. The sensors were mounted on modified KF25 blind flanges, with an electrical feed-through. Each sensor was sitting on an approx. 5 cm long, stiff cable which was connected to the inner side of the feed-through on the blind flanges. In this way, the sensors were reaching to the axial center of the target chamber when mounted. The resistance of the Pt100 sensors was measured by two NI 9217 modules. The same modules also converted the measured resistance (based on their inner calibration) into temperature readings for the LabView system.

The temperature gradient was only measured in the target chamber. The temperature of the small amount of gas present in the interconnection tube could be safely assumed to be equal to the room temperature since in this section of the target chamber no heat sources or sinks are present. The room temperature was logged by a Pt100 sensor, which was hanging freely in the accelerator room, near the gas target setup. Last but, not least an additional sensor was glued on the outer surface of the water cooled collimator.

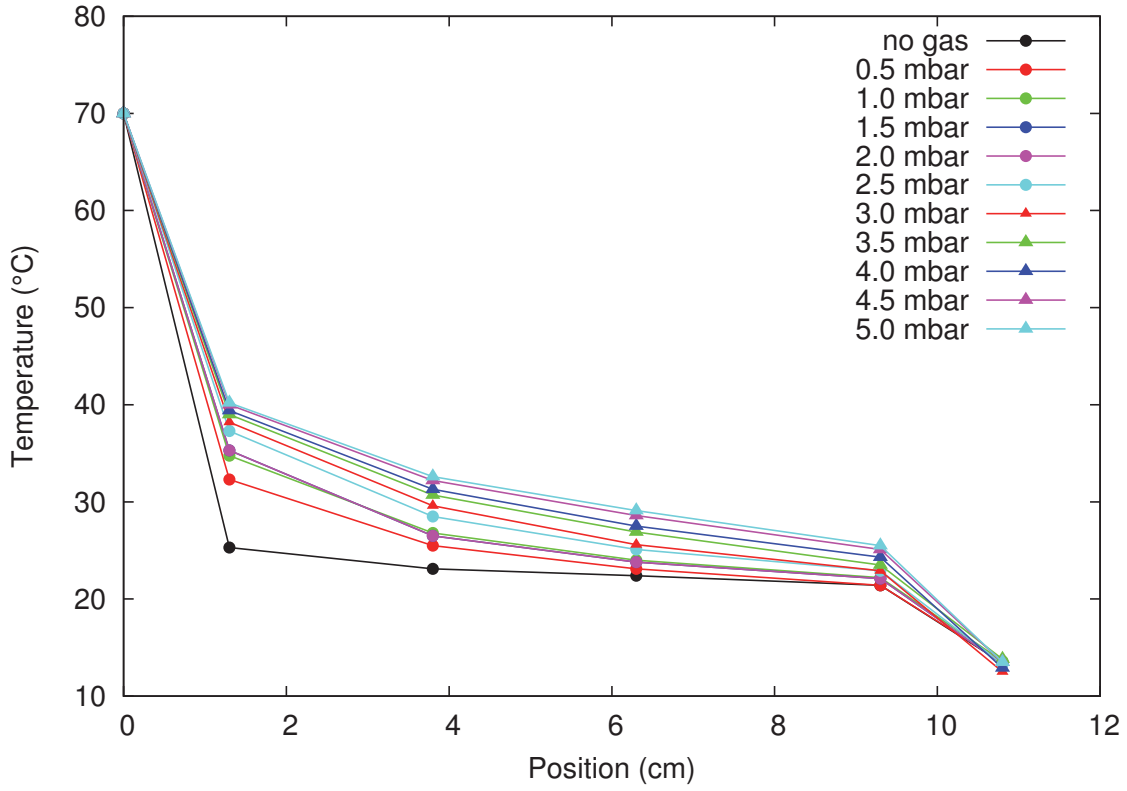

Figure 3.8: Temperature profile in the target chamber for several different target pressures. The lines are just to guide the eye.

According to their data sheet, the Pt100 sensors have an accuracy of 0.3°C, or equivalently 0.3 K. However, as it was observed the measured temperature values show some dependence on the orientation of the sensor. This effect is due to the housing of the sensor and introduces an uncertainty of approximately 1 K. Thus, the total uncertainty was assumed to be the quadratic sum of these two components, amounting to 1.1 K. Based on this value 0.4% uncertainty was assigned to the temperature values expressed in Kelvin.

During the experiments the target pressure was set to 2 mbar, thus one can obtain the density profile by combining the corresponding curves from Figs. 3.7 and 3.8. The uncertainty of the obtained density values amounted to 1.1%, by combining the uncertainties of the pressure and temperature measurement in quadrature.

As it is evident from Fig. 3.9, the density shows different trends in the three sections of the target: In the chamber, the gas density slowly increases from the calorimeter towards collimator as the gas cools down. Inside the collimator, there is a quick drop in the density, which continues with a linear decrease in the interconnection tube.

Due to the design of the flute chamber, no measurement point is available at the beginning and end of the collimator. Therefore, one has to resort to the extrapolation of the density trend inside the chamber and the interconnection tube. A linear drop between these extrapolated values was expected inside the collimator, but the actual measurement resulted in a somewhat higher density. This issue is probably caused by the fact that in case of the collimator the pressure gauges could not be mounted directly to the flute chamber due to geometrical constraints. Instead, they were connected via thin copper tubes. It is possible that due to the small diameter and relatively large length of these tubes, some gas was trapped in front of the pressure gauges,which led to an overestimation of the pressure.

It is useful to define the so-called effective target length L_{eff} for a reference density n_{ref}. Since the adopted target pressure during the measurement was 2 mbar, it was convenient to base reference density on this pressure value. The typical room temperature inside the accelerator room during the experiment was 23°C. However, some variations were possible depending on the amount of electric equipment switched on, and other activities in the accelerator room. Therefore, the uncertainty on the temperature measurement in this case was considered to be 1%. Assuming 1% uncertainty on the pressure, this led to 1.4% uncertainty on the reference density.

By integrating the density profile from the first pumping stage to the front face of the calorimeter, the effective target length was found to be

$$L_{\text{eff}} = 14.5 \pm 0.5 \text{ cm} \tag{3.6}$$

from which the chamber contributes 10.6 cm, the collimator 2.7 cm and the interconnection tube 1.3 cm. This means that the beam has to travel a path of 9.3 cm to reach the center of the target. The 0.5 cm uncertainty is estimated considering alternative density profiles inside the collimator (see Fig. 3.9).

With the help of the effective target length L_{eff} and the reference target density n_{ref}, the total energy loss in the gas target can be expressed as

$$\Delta E = n_{\text{ref}} \epsilon L_{\text{eff}} \tag{3.7}$$

where ϵ is the stopping power.

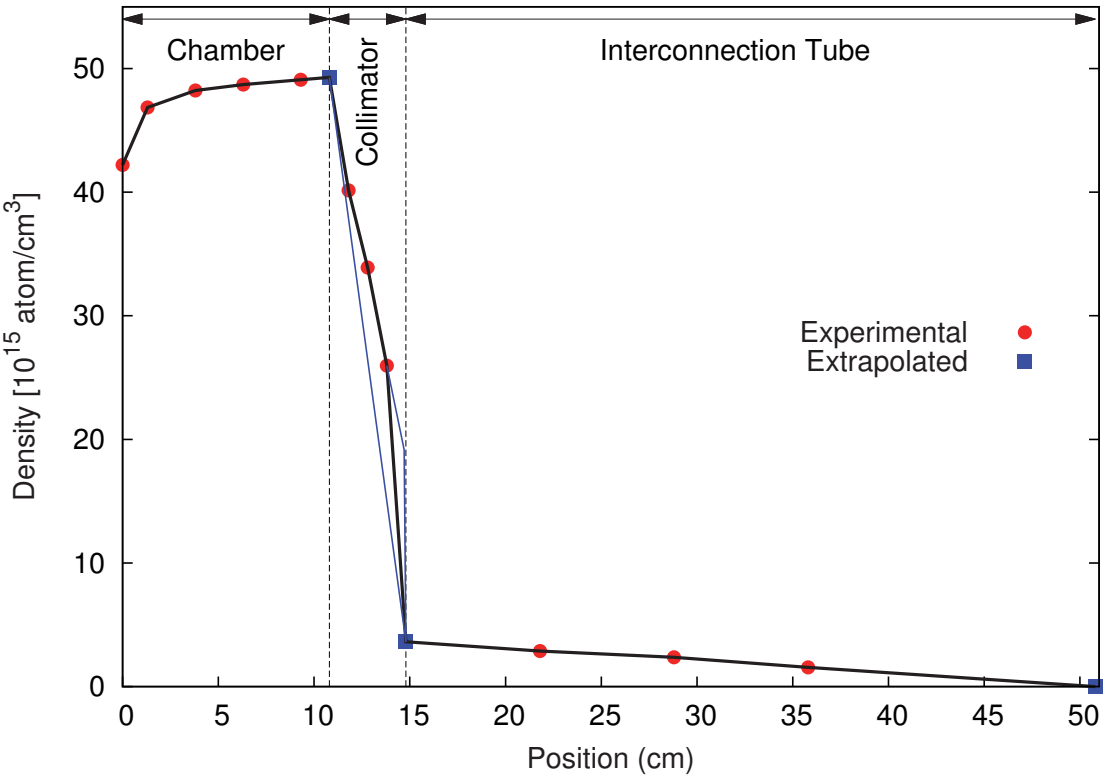

Figure 3.9: Gas density profile along the beam axis (beam from the right). The black line represents the adopted density profile, while blue lines show two alternative profiles inside the collimator.

3.2.4 Beam heating correction

During an irradiation the impinging beam loses some of its energy due to collisions with gas atoms inside the target. This leads to an increase in the temperature of the target gas along the beam path. As the gas warms up, its density decreases and thus the density profile will not be identical to the one measured without beam. This so-called beam heating effect is a typical feature of gas targets, and has already been investigated in previous gas target experiments [47–49].

Recently, the phenomenon was also studied in natural neon at LUNA by using the same differentially pumped gas target system [50]. The measurement was based on the fact that a small fraction (0.27%) of the natural neon gas is ^{21}Ne. The ^{21}Ne(p,γ)^{22}Na reaction has a narrow ($\Gamma < 3$ eV), but quite strong resonance ($\omega\gamma = 83$ meV) at $E_p^{\rm lab} = 271.6$ keV proton beam energy. Due to its narrow width the position of the resonance inside the target chamber is well localised.

In order to populate the resonance at $E_p^{\rm lab}$, the initial proton beam energy $E_p^{\rm ini}$ has to satisfy the following condition

$$E_p^{\rm ini} = E_p^{\rm lab} + \Delta E \tag{3.8}$$

where ΔE is the beam energy loss in the target. The latter quantity is directly proportional to the gas density. Therefore, by comparing the experimentally determined ΔE to its expected value based on the density n_0 measured without the beam, one can calculate the density reduction factor n/n_0.

Using this method, the beam heating effect as a function of the dissipated beam power per unit length dW/dx was found to be described by the following empirical expression [50]

$$\frac{n}{n_0} = 1 - C\frac{dW}{dx} \tag{3.9}$$

with beam heating coefficient $C = (0.44 \pm 0.05) \times 10^{-3}$ cm/mW.

Unfortunately, the reported value of the beam heating coefficient cannot be directly adopted for the present experiment due to differences in the target design: in contrast to the cylindrical target chamber with an inner diameter of 54 mm outlined in Sec. 3.2.1, the chamber of the previous, HPGe-based experimental phase [50] had a rectangular cross section of 120 × 104 mm. This geometrical difference has to be reflected in Eq. 3.9.

Assuming that the walls of the chamber act as an infinite, room-temperature heat sink, it is possible to put an upper limit on temperature difference ΔT between the central beam heated part of the gas and the walls of the chamber [51]:

$$\Delta T = \frac{1}{2\pi K}\frac{dW}{dx}\ln\left(\frac{D}{d}\right) \tag{3.10}$$

where K is the thermal conductivity of the target gas, D is the inner diameter of the cylindrical chamber, and d is the diameter of the cylindrical gas volume heated by the beam, corresponding to the diameter of the collimator.

Since for both chamber designs the diameter of the collimator was 7 mm, the only difference in Eq. 3.10 is parameter D. Consequently, the difference in the beam heating coefficient can be approximated as follows

$$C_{\mathrm{BGO}} = C_{\mathrm{HPGe}}\frac{\ln\left(D_{\mathrm{BGO}}/d\right)}{\ln\left(D_{\mathrm{HPGe}}/d\right)} = 0.32\frac{\mathrm{cm}}{\mathrm{mW}} \tag{3.11}$$

where in case of the chamber used in the HPGe phase an effective inner radius of $D_{\mathrm{HPGe}} = 120$ mm was assumed.

Using Eq. 3.10 one can also compare the heat conduction in different gases based on their thermal conductivity K. This provides an alternative way to determine the beam heating coefficient for the present experiment, thus to check the result of the previous method. The present target chamber is the same one, which was previously used in the ^{14}N(p,γ)^{15}O LUNA experimental campaign [48]. During the measurements the beam heating effect was studied with nitrogen gas, and a beam heating coefficient of $C = 0.54 \times 10^{-3}$ cm/mW was determined. The thermal conductivity of nitrogen gas ($K_{\mathrm{N_2}} = 0.026$ W /mK) is approximately half of the one of neon ($K_{\mathrm{Ne}} = 0.049$ W /mK). This means that the conduction of heat in neon gas is more efficient than in nitrogen, and the beam heating coefficient has to be scaled as follows:

$$C_{\mathrm{Ne}} = C_{\mathrm{N_2}}\frac{K_{\mathrm{N_2}}}{K_{\mathrm{Ne}}} = 0.29\frac{\mathrm{cm}}{\mathrm{mW}} \tag{3.12}$$

Since both methods yield comparable values for the beam heating coefficient, their average value was accepted for the present experiment:

$$\frac{n}{n_0} = 1 - (0.31 \pm 0.09)\frac{dW}{dx} \tag{3.13}$$

Due to the fact that the determination of these value relies on measurements either in different geometry or in different target gas, as a conservative 30 % uncertainty was assigned. With this assumption, the typical beam heating correction was less than 5%.

3.3 BGO detector and DAQ

The detection system was based on a large, segmented bismuth germanate ($Bi_4Ge_3O_{12}$, commonly referred to as BGO) scintillator, produced by Scionix [52]. The detector consists of six optically separated segments, which surround the target chamber in a cylindrical geometry. It has a length of 28 cm and an outer radius of 10 cm, however the actual radial thickness of the crystals is only 7 cm, because the coaxial hole occupied by the target chamber takes up the first 3 cm of the radius. Each crystal can be coupled with two photomultipliers (PMT) (one on the front, and one back end of crystal). In the experiment, however, the crystals were read out only on their back ends due to space constraints, while on their front end they were fitted with a light reflective cap without PMT.

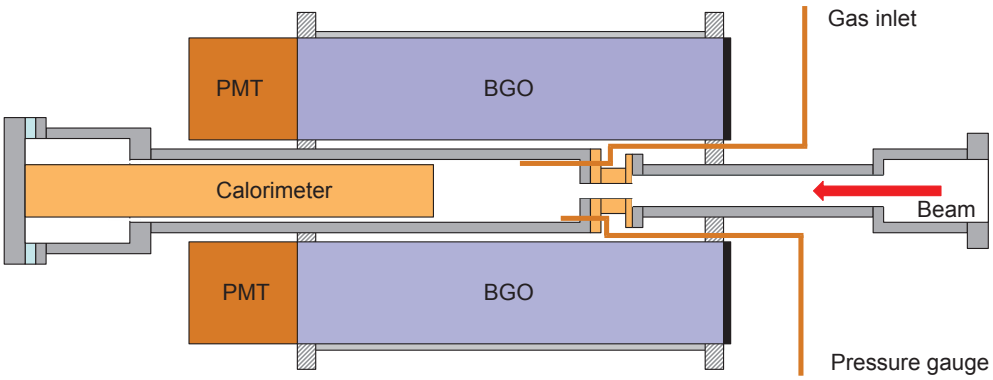

Figure 3.10: BGO detector with target chamber (not to scale)

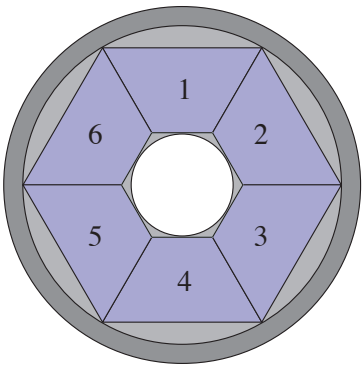

Figure 3.11: Cross section of the BGO detector (not to scale)

The high voltage for the PMTs was provided by a VME-based CAEN V6533P 6-channel power supply. The logical interface between the VME-crate and the control PC was provided by a CAEN V1718 VME-to-USB bridge controller. The voltage of each of the six channels could be adjusted separately using the CAEN GECO2020

control software. During the experiment supply voltages around 900 V were used. The gains of the six PMTs were matched by slightly adjusting their supply voltage.

The signal taken from the anode of each PMT was amplified by one ORTEC 113 charge sensitive pre-amplifier per PMT. The amplified signal then was connected to one of the analog input channels of a CAEN V1724 8-Channel 14 bit 100 MS/s digitizer mounted in the same VME-crate as the power supply of the PMTs. No spectroscopy amplifier was used. The CAEN V1724 card uses a trapezoid filter for pulse height analysis (parameters are listed in Table 3.1). The digitizer was read out by the MC2 Digital MCA Data Acquisition and Analysis Software provided by its manufacturer.

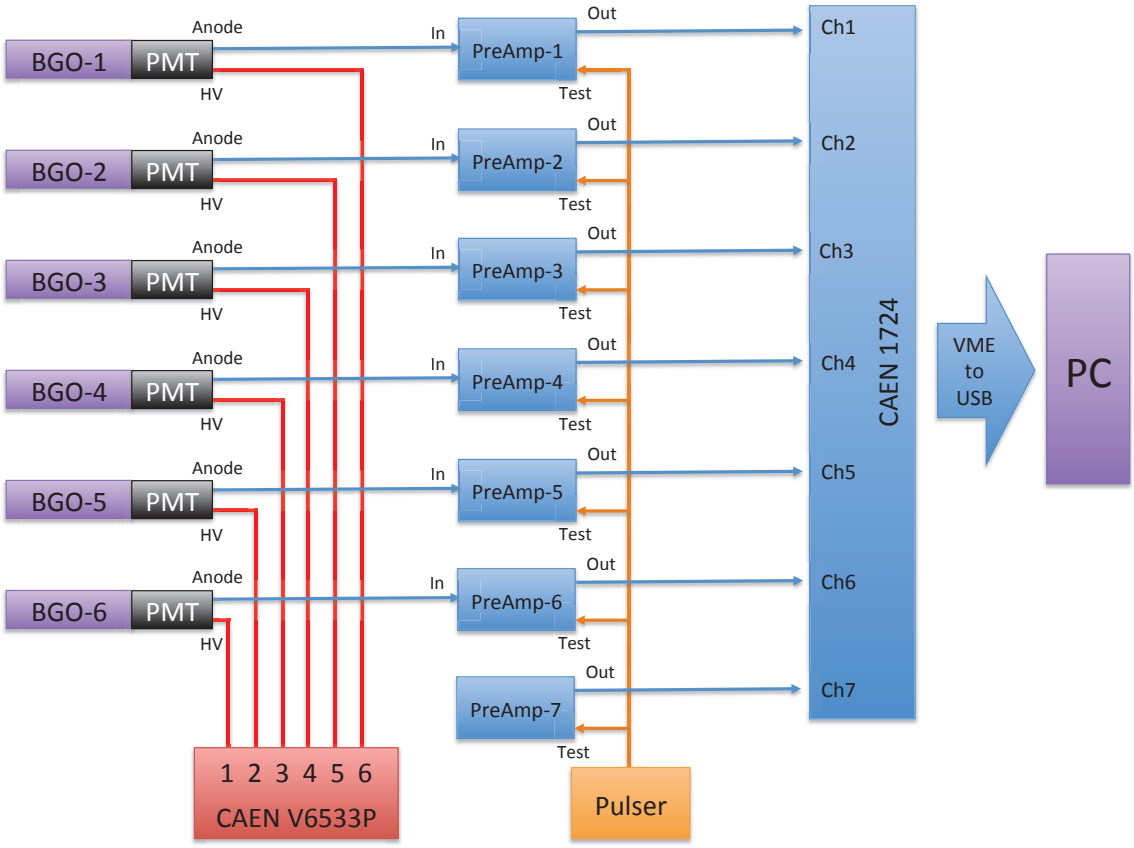

Figure 3.12: Scheme of the data acquisition system

The events were recorded in list-mode format, which made the use of conventional coincidence modules unnecessary. During the data acquisition each channel triggered and stored events independently from the rest. This is different from the described behaviour in the documentation, but clearly visible from the raw data. The coincidence analysis was done off-line based on the time stamps.

In order to monitor the dead-time of the detection system, a BNC PB-5 pulser was also incorporated in the electronics setup. The 50 Hz pulser signal was injected into the data acquisition chain through the "TEST" input of the pre-amplifiers connected to the PMTs. As a reference, a seventh ORTEC 113 pre-amplifier receiving only the pulser signal was used. The output of this pre-amplifier was connected to a separate channel of the CAEN digitizer.

Table 3.1: Main parameters of the CAEN V1724 digitizer with their typical values for BGO segments 1-6 and the pulser. (For their definition refer to the manual of the CAEN V1724 digitizer: www.caen.it.)

Settings group	Parameter	BGO1-6	Pulser
Input Signal	DC offset	14750 LSB*	14600 LSB*
	Decimation	1	1
	Digital gain	8	8
	Pulse polarity	NEG	NEG
Trigger	Threshold	30 LSB*	100 LSB*
	RC-CR2	32	4
	Trigger hold-off	2.00 μs	1.30 μs
	Input rise time	0.20 μs	0.20μs
Energy filter	Baseline mean	1024	256
	Trapezoid gain	1.00	1.00
	Trapezoid rise time	3.00 μs	3.00 μs
	Decay Time	35.0 μs	35.0 μs
	Trapezoid flat top	5.00 μs	5.00 μs
	Flat top delay	50.0 %	50.0 %
	Peak mean	64	64
	Baseline hold-off	0.50 μs	0.50 μs
	Peak hold-off	1.00 μs	1.00 μs
Firmware	DPP-PHA 4.5.128.30 (Feb. 2015)		

* 1 LSB = $2.25\text{V}/2^{14} = 0.137$ mV

3.4 Detector efficiency

The detection efficiency of the above described BGO based setup was studied with the help of radioactive sources, in-beam measurements and Monte Carlo simulation. Due to the nearly 4π geometry and large thickness of the crystals, the detector absorbs very efficiently the γ-photons produced inside the target chamber. The peak detection efficiency can be further increased if the signals from the six segments are summed up in coincidence (add-back mode). In this way, the total energy of γ-rays, which are depositing energy in more than one crystal, can be also restored, compared to the method were the single spectra from the segments are simply combined.

Consequently, one has to differentiate between the peak detection efficiency of the single crystals and add-back (summing) efficiency of the whole detector. The energy dependence of the single crystal efficiency can be easily studied by standard calibration sources and nuclear reactions. On the other hand, the efficiency of the add-back mode is more difficult to understand, because the total energy of the excited state is usually not deposited in a single step, but in a cascade of gamma photons. From this reason, the efficiency with which an excited state is detected depends on its exact decay structure. Furthermore, if more than one transition is possible from an excited state, the branching ratios between these transitions will also influence the final add-back efficiency.

In principle, it is possible to provide an analytical description of the add-back efficiency if the single crystal efficiency and the decay probabilities of the intermediate

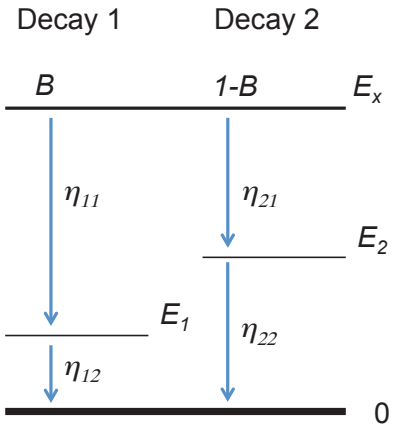

Figure 3.13: Decay of an excited state E_x through two possible γ-cascades with branching ratio B. The detection efficiency for each member of the cascades is denoted as η_{ij}.

states are known. For example, in the simple case which is presented in Fig. 3.13, it can be obtained as follows:

$$\eta_{\text{Add-back}} = B\eta_{11}\eta_{12} + (1-B)\eta_{21}\eta_{22} \tag{3.14}$$

However, it is evident that such an analytical approach becomes impractical if the decay proceeds via a larger number of intermediate states. In order to avoid these complications, and to have a better understanding of the add-back detection efficiency, a precise model of the target chamber and BGO detector was created using GEANT4 [53]. The code does not simulate the nuclear reactions, only the decay of a selected excited state, or radionuclide. The energy loss of the bombarding protons is not implemented, instead the user can explicitly specify the beam energy at the position of the γ-ray emission along with target temperature and pressure in a macro file. The decay probabilities and branching ratios were taken from the ENSDF database.

In order to test the Monte Carlo simulation, the efficiency was measured experimentally with point-like radioactive sources. Standard sources with one or two intense gamma-lines were chosen to make the comparison with simulation easier: ^{7}Be, ^{60}Co, ^{88}Y and ^{137}Cs.

As the interaction with the beam can take place at different positions in the gas target, it was necessary to map the detection efficiency along the beam axis. For this purpose, a special source holder and positioning equipment was made.

Table 3.2: Properties of the radioactive calibration sources (The given uncertainty on the source activity crossesponds to 1σ.)

Isotope	Half-life	Manufacturer	Ref. Activity [kBq]	Ref. Date
^{7}Be	53.22 days	MTA-ATOMKI	112.6 ± 2.4	18. April 2014
^{60}Co	5.27 years	PTB	9.12 ± 0.04	1. January 2005
^{88}Y	106.6 days	Eckert & Ziegler	36.8 ± 0.4	1. April 2014
^{137}Cs	30.08 years	PTB	11.30 ± 0.06	1. January 2005

For the source holder, a very light, frame-like design was constructed from plastic (shown in Fig. 3.14), in which the attenuation of γ-rays was quantified with Monte Carlo simulation: in case of of the 477 keV gammas from the decay of ^{7}Be, the presence of the source holder caused $1.7 \pm 0.5\%$ reduction in the number of γ-rays hitting the detector, while 1836 keV gammas of the ^{88}Y source suffered $1.3 \pm 0.5\%$ attenuation. These attenuation effects were seen mainly by the two detector crystals in plane with the source holder, while the ones located above and below were unaffected.

The source holder then was mounted on one end of a 750 mm long, rectangular (10x10 mm) metal rod. In order to keep the source aligned along the axis of the target chamber and to allow a precise positioning, a support structure was manufactured from a blind flange, which could be mounted on the back end of the target chamber after the removal of the calorimeter. (See Fig. 3.15.) It had a rectangular borehole in its center with the same dimensions as the cross section of the positioning rod. In order to provide additional support against the torque produced by the weight of the rod in eccentric positions, a 100 mm long T shape stainless steel reinforcement was mounted on the outer side of flange.

The detection efficiency for the 661 keV gamma-line of a point-like ^{137}Cs radioactive source is shown in Fig. 3.16 as function of the source position. Due to geometrical constraints, the efficiency could be directly measured only inside the chamber, while the simulation was extend to the whole setup. In case of the simulation, the detection efficiency at a given x position along the beam axis was calculated as follows:

$$\eta_{\text{eff}}(x) = \frac{N_{ROI}(x)}{N_{started}} \tag{3.15}$$

where $N_{ROI}(x)$ is the number of add-back events that have an energy corresponding to the selected region of interest (ROI), and $N_{started}$ is the total number of simulated decays. The simulated efficiency was found to match the experimentally measured one within 4% without any rescaling applied. For the data analysis, this difference was treated as the typical uncertainty of the GEANT4 simulation.

Besides the measurements with the radioactive sources, the gammas originating from the decay of the well-known resonance in ^{14}N(p,γ)^{15}O at $E_p = 278$ keV were also used to check the detector simulation at higher energies. Fig. 3.17 shows a comparison between an experimental and a simulated single crystal spectrum.

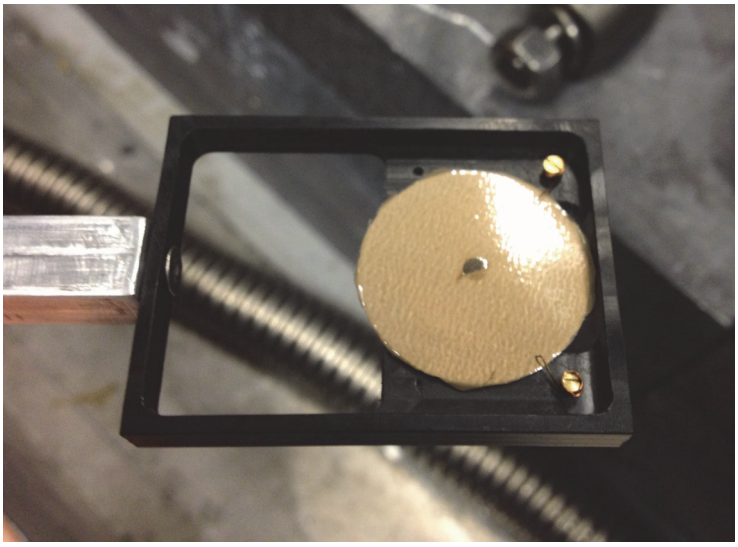

Figure 3.14: Source holder for efficiency measurement

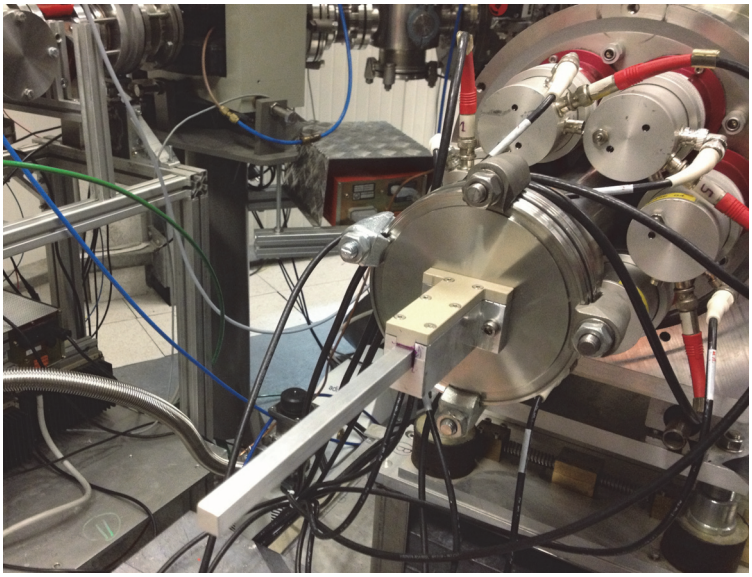

Figure 3.15: Modified end flange and positioning rod for efficiency measurement

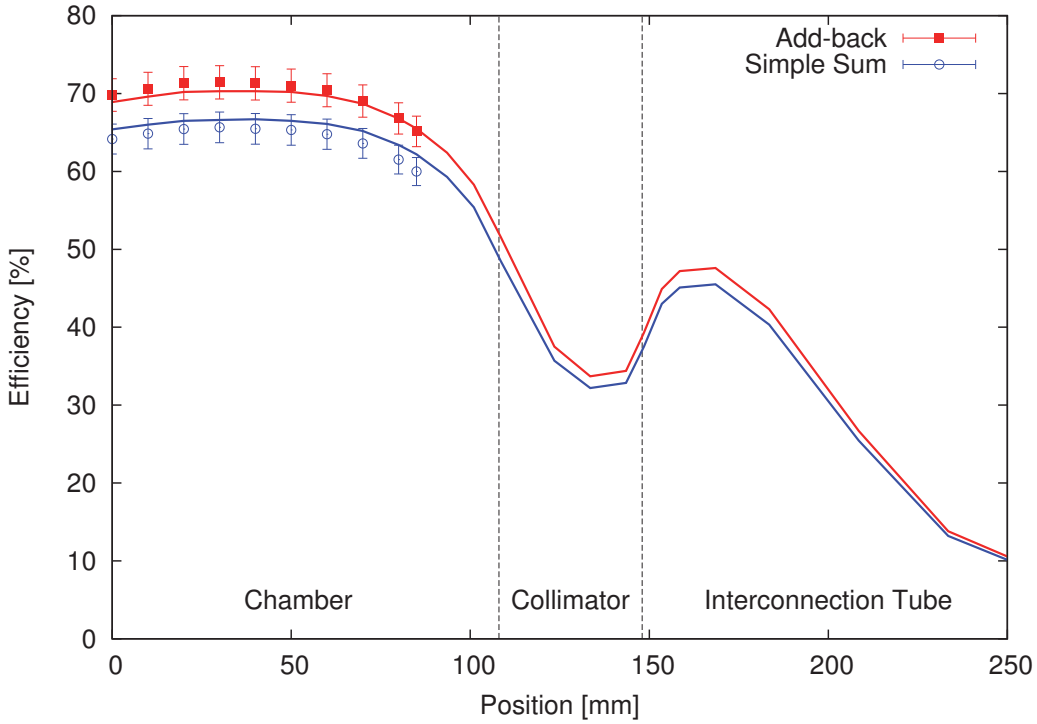

Figure 3.16: Efficiency as function of position, measured with a point-like ^{137}Cs radioactive source. Comparison with the Monte-Carlo simulation (solid lines) is shown both for the simple and add-back summing of the detector segments.

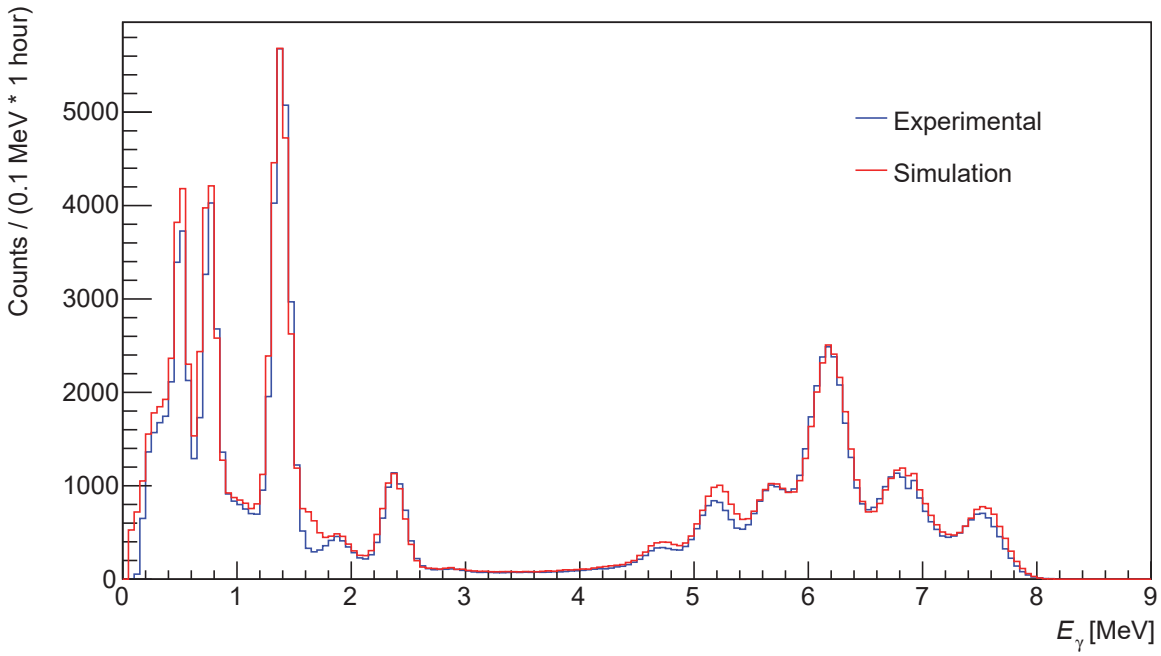

Figure 3.17: Measured and simulated single sum spectra obtained on the $E_p^{\mathrm{lab}} = 278$ keV resonance in ^{14}N(p,γ)^{15}O. Both spectra were created by gating on the ^{14}N(p,γ)^{15}O peak in the add-back spectrum. The simulated spectrum was normalized to the experimental one.

Chapter 4

Results of the ^{22}Ne(p,γ)^{23}Na experiment at LUNA

The aim of the experimental campaign was to collect statistics on the so far unobserved resonances at $E_p^{\mathrm{lab}} = 71$ and 105 keV, and to study the non-resonant component of the ^{22}Ne(p,γ)^{23}Na reaction rate. In addition to this, the three low-energy resonances ($E_p^{\mathrm{lab}} = 156.2$, 189.5, 259.7 keV) reported in the previous phase of the LUNA experiment were remeasured to confirm the resonance strength values obtained [33].

During the more than five months of data taking, the following experimental procedure was followed: The buffer of the gas target system was filled with isotopically enriched (99.9%) ^{22}Ne gas up to a pressure of 500-800 mbar. With the purifier turned on, the gas target was then switched to recirculation mode and the pressure inside the chamber was adjusted to 2 mbar using the manual valves and the MKS automatic feed back valve. At this point, the so-called "zero power" (W_0) of the calorimeter was measured to establish the reference for the calorimetric beam current reading.

After this, the electropneumatic inlet valve of the target chamber was shut off to collect the gas in the buffer. This step was necessary to allow the optimisation of the beam transmission, because otherwise the large number of secondary electrons induced in the gas would have made the electrical readings on the collimators unreliable. The currents of the analysing and steerer magnets were tuned along with the source parameters so that the electrically measured beam current on the target was maximal while the losses on the three consecutive collimators were kept minimal. With the proper beam parameters set, the ^{22}Ne gas was let back to the chamber and the data acquisition was started. At a certain energy, usually several days of statistics were collected in roughly one day long runs. At the end of each experimental run the measurement of W_0 was repeated.

Beam	OFF	ON	ON	OFF
Target pressure	2 mbar	0 mbar	2 mbar	2 mbar
Work phase	W_0 (1)	Focusing (2)	Measurement (3)	W_0 (4)

Figure 4.1: 4-phase experimental procedure

4.1 Detector background

Thanks to the very effective shielding against the cosmic muons by the rock overburden, the background in the BGO detector originates mainly from two sources: natural radioactivity and nuclear capture reactions induced by the beam. It is apparent from Fig. 4.2, that up to 3.7 MeV the spectrum is dominated by the γ-rays from the decay of natural radioisotopes present in the walls of the laboratory and the BGO crystal itself. The resolution of the BGO detector was not sufficient to separate well these natural γ-lines, therefore only a few of them could be clearly identified: ^{40}K, ^{207}Bi, ^{208}Tl, ^{214}Bi.

The ^{207}Bi isotope is an intrinsic contaminant, which is typical for all BGO crystals. In nature, it is produced from ^{207}Pb and ^{208}Pb via (p, n) and $(p, 2n)$ reactions by cosmic rays. In addition to this, the nuclear weapon tests in the 1960s led to an enrichment of ^{207}Bi in atmosphere and thus increased the global contamination levels in bismuth processed afterwards.

The long tail above 3.7 MeV and the following two distinct plateaus from 5.5 to 8.0 MeV and from 8.0 to 10.5 MeV are due to neutron capture on the materials of the detector housing and BGO crystal. While the flux of environmental neutrons is three order of magnitude lower than on the surface, there are still enough neutrons (both thermal and high-energy) left to generate energetic γ-rays via (n, γ) reactions on various isotopes of Fe, Cr, Ni and Ge. The neutron capture reactions in the copper calorimeter and collimator also contribute to the counting rate in these regions.

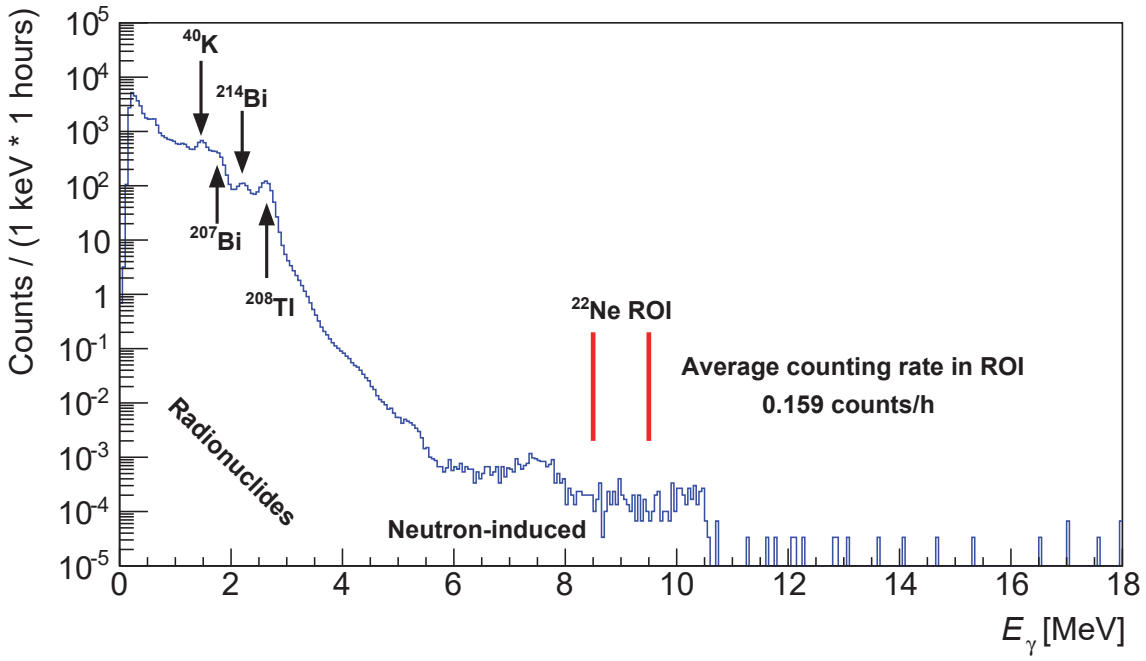

Figure 4.2: Natural background seen by the BGO detector in add-back mode

Due to the adopted add-back measurement method, the signal of the ^{22}Ne(p,γ)^{23}Na ($Q = 8.794$ MeV) reaction is expected at energies corresponding to the excited levels in ^{23}Na. For low energy resonances under investigation the region-of-interest is around 9 MeV ($E = Q + E_{\mathrm{cm}}$) and it is typically 1 MeV wide. As can be seen in Fig. 4.2, the average counting rate in this region is in the order of 10^{-4} counts/(keV h).

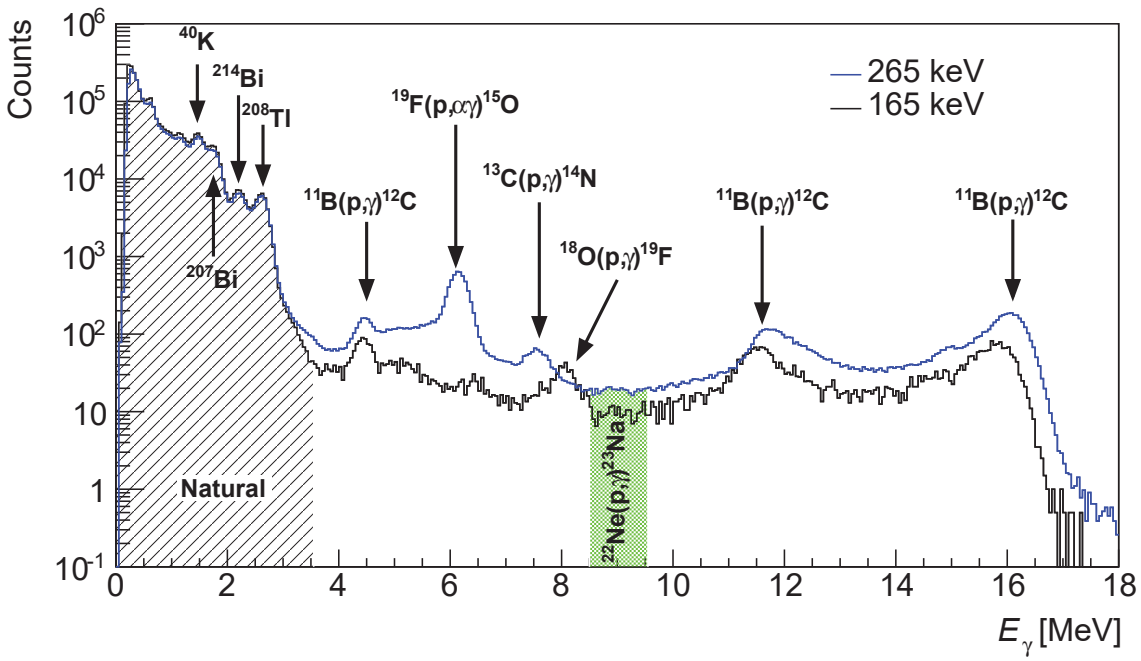

Figure 4.3: Beam induced background at $E_p^{\text{ini}} = 165$ keV and 265 keV in argon gas

Due to this extremely low counting rate, in most cases the main concern is represented by the additional nuclear reactions induced by the proton beam. The most common sources of beam-induced background are listed in Table 4.1.

Table 4.1: Common contaminant reactions in the gas target

Reaction	Q-value [MeV]	γ-lines in the add-back spectrum [MeV]
^{15}N(p,$\alpha\gamma$)^{12}C	4.965	4.439
^{14}N(p,γ)^{15}O	7.296	7.296+E_{cm}, 6.791, 6.172, 5.180
^{13}C(p,γ)^{14}N	7.551	7.551+E_{cm}
^{18}O(p,γ)^{19}F	7.993	8.136, 8.026, 7.939, 4.230, 3.906
^{19}F(p,$\alpha\gamma$)^{16}O	8.114	6.130
^{15}N(p,γ)^{16}O	12.126	12.126+E_{cm}
^{11}B(p,γ)^{12}C	15.956	15.957+E_{cm}, 11.661, 4.439

As can be seen in Fig. 4.3, the beam-induced background varies with the beam energy, because depending on their cross section at different energies different groups of contaminants come into focus. Moreover, resonances in the contaminant nuclear reactions lead to rapid changes in the counting rates. Therefore, if possible, the beam-induced background should be investigated at the same energy as the nuclear reaction under study.

However, a spectrum taken in vacuum at the same beam energy does not necessarily reflect the actual beam-induced background correctly: When the gas target is filled with ^{22}Ne gas, the bombarding protons not only lose energy due to collisions with the target atoms, but also experience angular deflection. The latter effect is called angular straggling, and leads to angular spreading of the beam. Thus, the beam may hit such deposits of contaminants inside the target chamber, which would

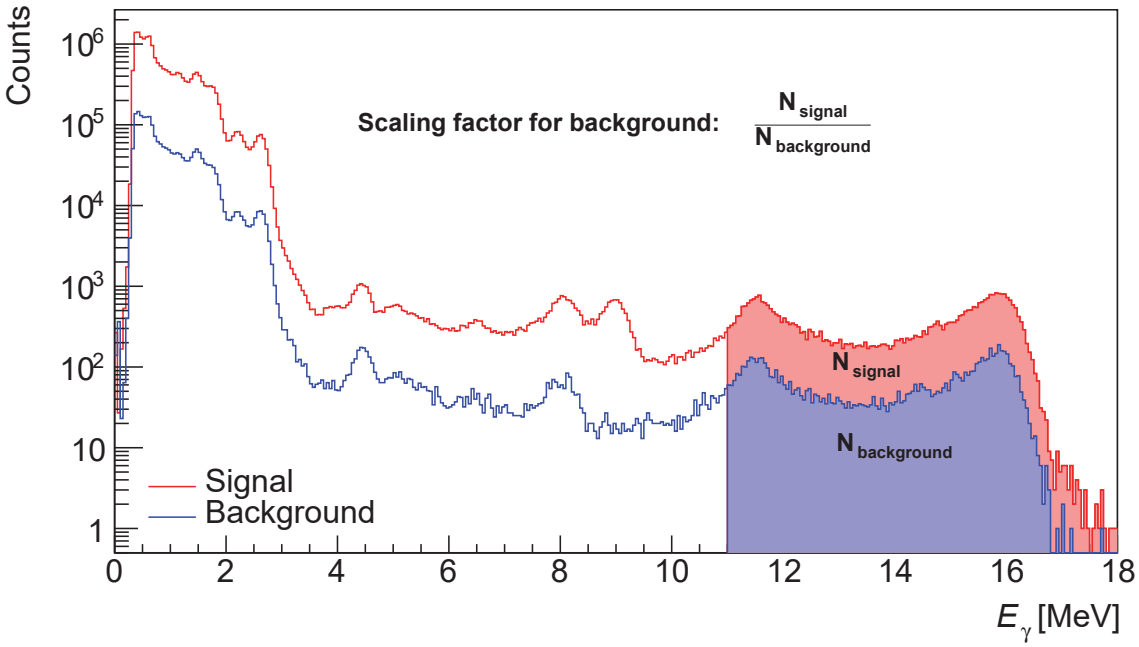

Figure 4.4: Illustration of the adopted background normalization approach

not be excited in vacuum.

From this reason, the background measurements were done in natural argon gas instead of vacuum. However, it is important to note that there is nearly a factor of two difference in the stopping powers of ^{nat}Ar and ^{22}Ne. Therefore, at the same pressure the beam energy loss and the straggling are very different in the two gases. In order to reach the same beam energy at the calorimeter, the pressure of the argon gas was decreased compared to ^{22}Ne.

The contaminants can be present either in the target gas, or localized on an inner surface of the target chamber. With respect to the bound contaminants, the two locations with the highest impact are the target collimator and the calorimeter, because they are in direct interaction with the beam.

The spectrum over 10 MeV is dominated by the ^{11}B(p,γ)^{12}C reaction. Its full energy peak is located around 16 MeV (Q-value + E_{cm}). However, the add-back summing is not always complete. Therefore, the single γ-lines from the de-excitation of ^{12}C are also visible at 11.6 MeV and 4.4 MeV. Since the Compton-continuum of the structure above 10 MeV contributes to the counting rate in the ^{22}Ne(p,γ)^{23}Na ROI, considerable effort was devoted to localise and remove the ^{11}B contamination. Unfortunately, the investigation was inconclusive, and only a minor reduction of the contamination level was achieved. On the other hand, it was confirmed that the ^{11}B is a non-volatile contaminant. Therefore, the ^{11}B(p,γ)^{12}C signal shape is independent from the gas type and pressure.

Due to the fact that it is hard to keep a vacuum system completely free from small leaks, the stable isotopes of oxygen and nitrogen are also common contaminants. Their isotopes can be also localised on the inner surfaces of the gas target due to oxidization or implantation. With respect to the study of ^{22}Ne(p,γ)^{23}Na, the ^{18}O isotope is one of the most problematic contaminants, because its ^{18}O(p,γ)^{19}F reaction produces a characteristic sum peak at 8 MeV next to the ^{22}Ne ROI.

In order to better understand the long-term tendencies in the background, the measurements with ^{22}Ne were alternated with background runs every other day. Approximately, the same amount of time was devoted to measurements with ^{22}Ne and $^{\mathrm{nat}}$Ar at a given energy. Still, during the data analysis some scaling of the experimental spectra was necessary, because of the variations in beam current and focusing. Since the ROI for the ^{22}Ne(p,γ)^{23}Na reaction is mostly affected by the γ-rays from beam induced nuclear reactions, the spectra had to be normalised to the collected charge.

Instead of using directly the charge obtained from the calorimetric current measurement, a more precise approach was adopted to normalize the ^{22}Ne and ^{nat}Ar runs by using features already present in the spectra: the scaling factor was determined based on a ROI from 11 to 18 MeV, mainly dominated by the ^{11}B(p,γ)^{12}C reaction. The approach is illustrated in Fig. 4.4.

4.2 Resonant capture reaction

As it was already mentioned in Chapter 1, the reaction cross section can be dramatically enhanced if resonances are present. In case of isolated, narrow resonances, the cross section σ is well-described by the Breit-Wigner formula (see Eq. 1.18) and, thus the resonances are characterised by their resonance strength $\omega\gamma$ (Eq. 1.21). In this case the resonant yield can be expressed as follows:

$$Y_{\mathrm{res}} = \int_{E_0-\Delta E}^{E_0} \frac{\sigma_{BW}(E)}{\epsilon(E)} dE = \int_{E_0-\Delta E}^{E_0} \frac{1}{\epsilon(E)} \frac{\lambda^2}{2\pi} \omega\gamma \frac{\Gamma/2}{(E-E_r)^2 + (\Gamma/2)^2} dE \tag{4.1}$$

Since the change in the stopping power $\epsilon(E)$ over the beam energy loss ΔE is typically negligible, it can be evaluated at the resonance energy E_r. The de Broglie wavelength λ also has to be determined at E_r, therefore it can be moved out of the integrand.

$$Y_{\mathrm{res}} = \frac{1}{\epsilon_r} \frac{\lambda_r^2}{2\pi} \omega\gamma \int_{E_0-\Delta E}^{E_0} \frac{\Gamma/2}{(E-E_R)^2 + (\Gamma/2)^2} dE \tag{4.2}$$

Noting that $\int (1+x^2)^{-1} dx = \arctan x + c$, this integral can be calculated analytically, thus, one obtains the following expression for the yield

$$Y_{\mathrm{res}} = \frac{1}{\epsilon_r} \frac{\lambda_r^2}{2\pi} \omega\gamma \left[\arctan\left(\frac{E_0 - E_r}{\Gamma/2}\right) - \arctan\left(\frac{E_0 - E_r - \Delta E}{\Gamma/2}\right) \right] \tag{4.3}$$

It can be shown that the maximum of the yield is achieved if the initial beam energy E_0 satisfies the following relation

$$E_0 = E_r + \frac{\Delta E}{2} \tag{4.4}$$

In this way, the resonance is populated in the center of the gas target, and the yield becomes

$$Y_{\mathrm{res,max}} = \frac{1}{\epsilon_r} \frac{\lambda_r^2}{\pi} \omega\gamma \arctan\left(\frac{\Delta E}{\Gamma}\right) \tag{4.5}$$

The total resonance width is the sum of the partial width of all open channel. For (p,γ) reactions, where only the proton and gamma channels are open, it can be written as $\Gamma = \Gamma_p + \Gamma_\gamma$. For the low energies of astrophysical interest $\Gamma_p << \Gamma_\gamma$ [1], thus the total resonance width Γ is dominated by the gamma width, which also means that the resonance strength $\omega\gamma$ (see Eq. 1.21) is basically determined by the proton width Γ_p:

$$\omega\gamma = \omega\frac{\Gamma_p\Gamma_\gamma}{\Gamma} \approx \omega\frac{\Gamma_p\Gamma_\gamma}{\Gamma_\gamma} = \omega\Gamma_p \tag{4.6}$$

Typically $\Gamma \approx \Gamma_\gamma$ is not larger than a few eV-s, while the beam energy loss ΔE in the target usually amounts to several keV-s. Thus $\Gamma << \Delta E$, and the arctan function in Eq. 4.5 converges to $\pi/2$. Consequently, the yield for an infinitely thick target becomes

$$Y_{\rm res}(\Gamma << \Delta E) = \frac{\lambda_r^2}{2}\frac{\omega\gamma}{\epsilon_r} \tag{4.7}$$

Usually, in order to obtain $Y_{\rm res}$ from the experimental yield $Y_{\rm exp}$, one has to correct for the detector efficiency $\eta_{\rm eff}$, the branching ratios B and angular distribution of the γ-photons $W(\theta)$. However, due to the nearly 4π detection geometry of the present experiment and the add-back detection mode used, the latter two corrections can be neglected. For the resonance strength $\omega\gamma$ thus one finds

$$\omega\gamma = \frac{2}{\lambda_r^2}\epsilon_r\frac{N}{N_b\eta_{\rm eff}} \tag{4.8}$$

where N_b and N are the numbers of bombarding particles and detected gammas.

4.2.1 71 keV resonance

Experimental yields were measured at four different beam energies near the recommended literature resonance energy of $E_p^{\rm lab} = 71 \pm 5$ keV [29]. A more detailed resonance scan would have been desirable because of the uncertainty in the actual resonance energy, however, due to beam time constraints it was not feasible. The typical measurement time for one experimental point was 2-3 days, followed by an in-beam background measurement of approximately equal length with $^{\rm nat}$Ar gas. The details of the measurement can be found in Table 4.2.

Based on its Q-value and the resonance energy of 71 keV, the γ-rays of the ^{22}Ne(p,γ)^{23}Na reaction were expected at 8862 keV. No clean peak-like structure is visible in the experimental spectra near this energy (see Fig. 4.5, 4.6, 4.7 and 4.8). Therefore, the counts were simply integrated between 8.36 and 9.36 MeV. The choice of the ROI was motivated by the level energy of the resonance ($E_x = 8862$ keV), and the resolution of the detector. The same ROI was used for all four beam energies, since the uncertainty related to the energy calibration of the BGO spectra was higher than the required shift due to the difference in beam energy.

As it was mentioned in Sec. 4.1, the natural background in LUNA is extremely low, thus in most cases it can be neglected due to the presence of the more prominent beam-induced background. However, as can be seen in Table 4.3, at the present beam energies the integrated number of counts in the ROI (both in ^{22}Ne and $^{\rm nat}$Ar gas) is consistent with the expected number of events from the natural background (based on the average counting rate reported in Sec. 4.1).

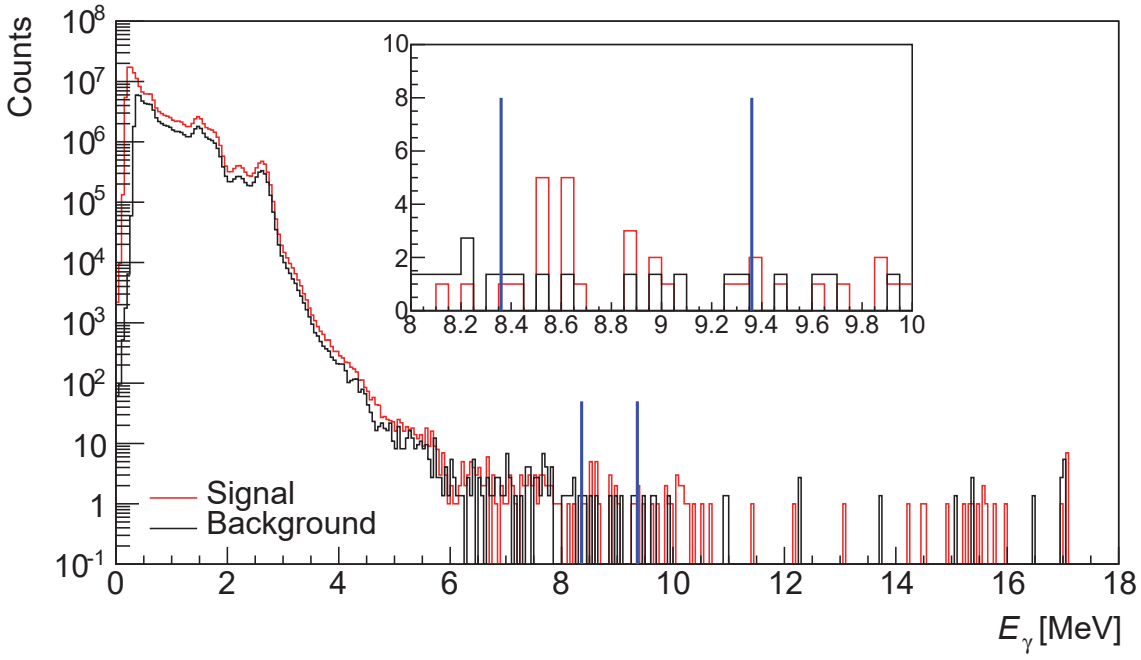

Figure 4.5: Experimental spectra at $E_p^{\mathrm{ini}} = 72.1$ keV.

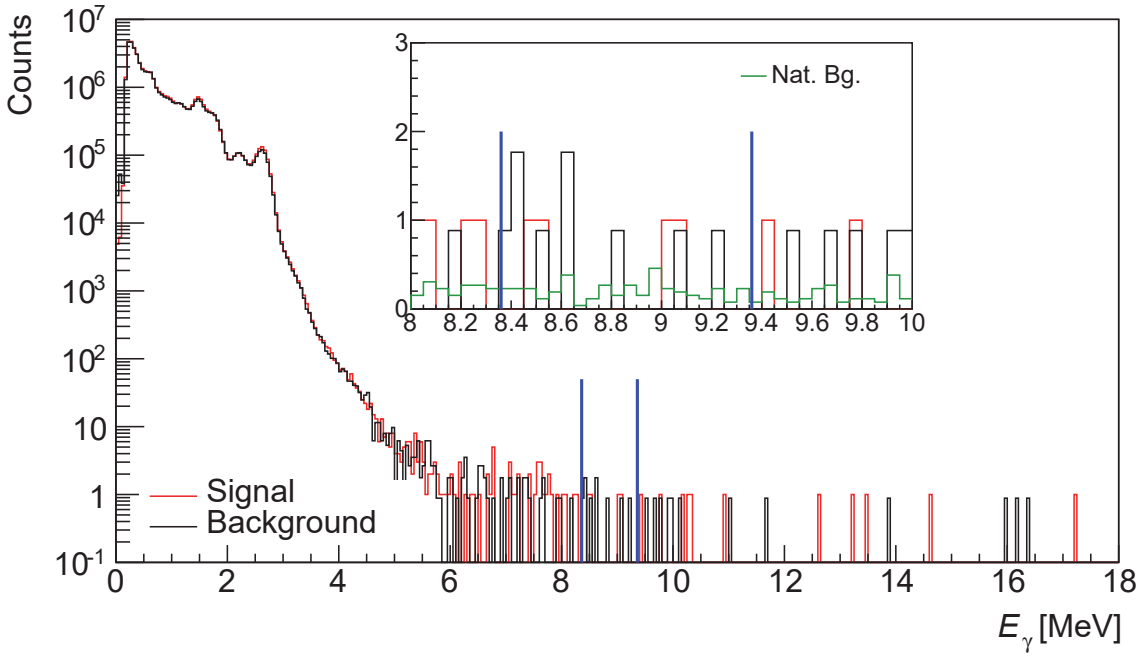

Figure 4.6: Experimental spectra at $E_p^{\mathrm{ini}} = 74.0$ keV.

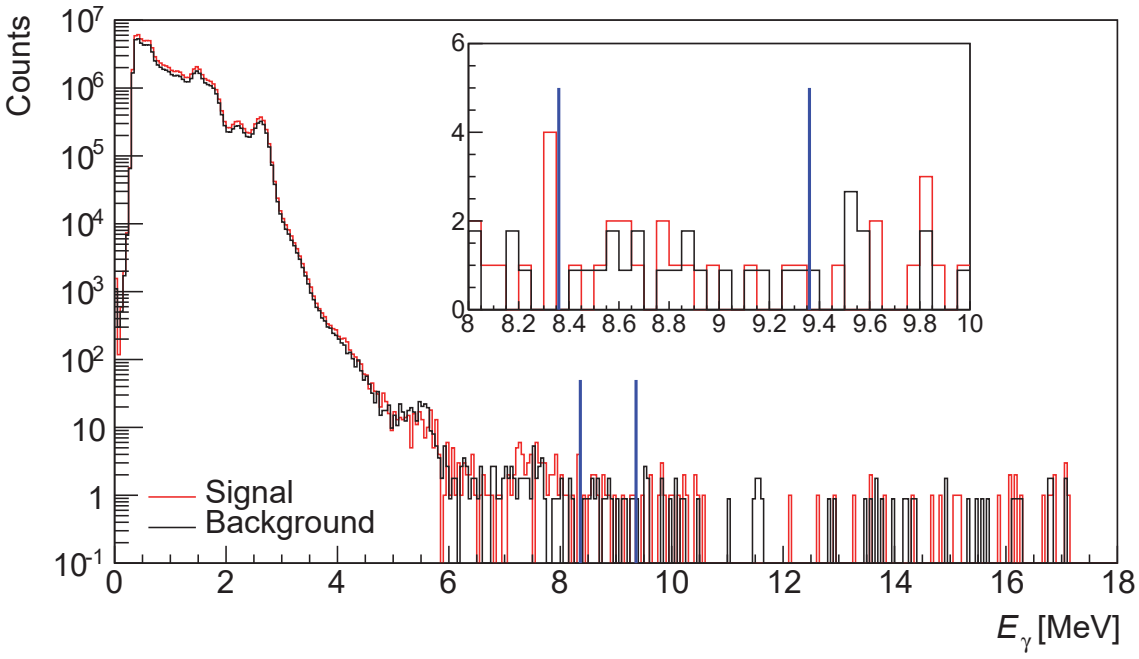

Figure 4.7: Experimental spectra at $E_p^{\mathrm{ini}} = 76.0$ keV.

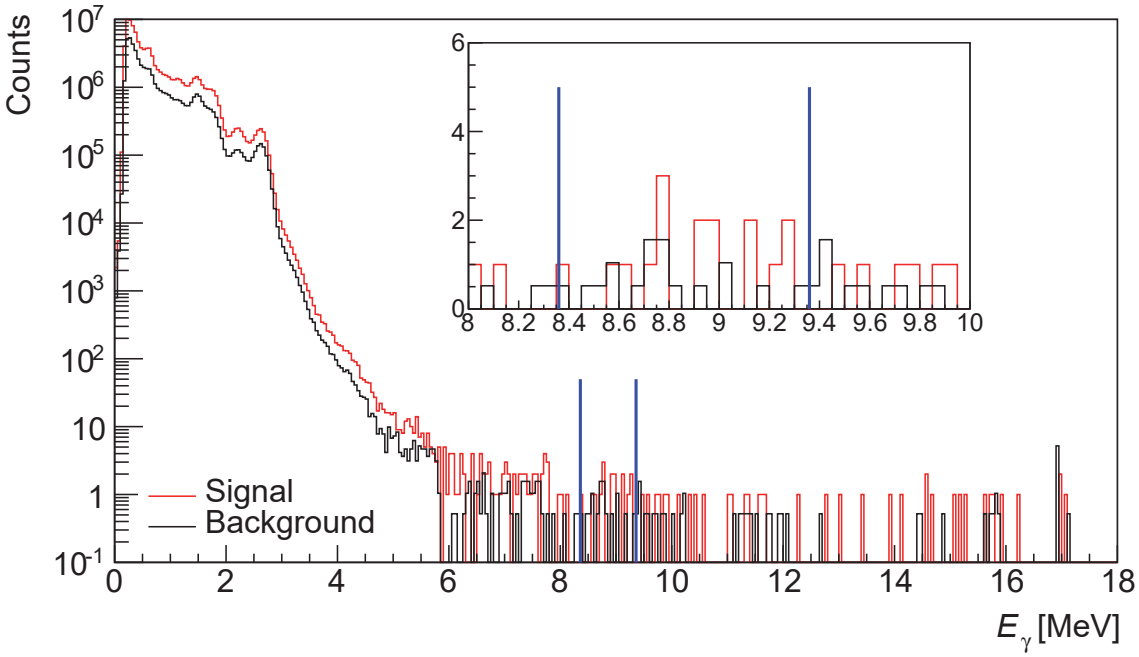

Figure 4.8: Experimental spectra at $E_p^{\mathrm{ini}} = 80.3$ keV.

Table 4.2: Experimental parameters for the resonance at $E_p^{\mathrm{lab}} = 71$ keV: E_p^{ini} and E_{target} correspond to the initial proton energy, and beam energy at the center of the target chamber in the laboratory frame, respectively. q is the integrated charge based on the calorimetric beam current measurement, t is the measurement time, and p_t stands for the target pressure.

		^{22}Ne gas			$^{\mathrm{nat}}$Ar gas		
E_p^{ini} [keV]	E_{target} [keV]	q [C]	t [h]	p_t [mbar]	q [C]	t [h]	p_t [mbar]
72.1 ± 0.3	65.8 ± 0.5	24.6 ± 1.0	80.5	2.00	18.0 ± 0.6	42.5	0.81
74.0 ± 0.3	67.7 ± 0.5	9.4 ± 0.3	22.8	2.00	10.6 ± 0.3	22.7	0.82
76.0 ± 0.3	69.6 ± 0.5	22.5 ± 0.8	64.4	2.00	25.4 ± 0.8	63.0	0.81
80.3 ± 0.3	73.8 ± 0.5	13.3 ± 0.5	40.7	2.00	25.6 ± 0.6	47.7	0.84

Table 4.3: Registered events (not normalised) in the experimental ROI (8.36-9.36 MeV) compared to the expected number of counts from natural background. (The latter numbers were obtained from Fig. 4.2 by scaling with the measurement time)

	^{22}Ne gas		$^{\mathrm{nat}}$Ar gas	
E_p^{ini} [keV]	ROI [counts]	$^{\mathrm{nat}}$Bg* [counts]	ROI [counts]	$^{\mathrm{nat}}$Bg* [counts]
72.1 ± 0.3	22	14.2 ± 1.4	9	7.5 ± 0.7
74.0 ± 0.3	4	4.0 ± 0.4	8	4.0 ± 0.4
76.0 ± 0.3	15	11.3 ± 1.1	19	11.1 ± 1.1
80.3 ± 0.3	16	7.2 ± 0.7	19	8.4 ± 0.8

* original counting rate: 105 events in 597.5 hours

Because of the low statistics, the analysis of the experimental data was done using a Monte-Carlo approach: The number of events measured in ^{22}Ne (ξ_{Ne}), or in $^{\mathrm{nat}}$Ar gas (ξ_{Ar}) during irradiation, and the counts from the natural background (ξ_{BG}) were assumed to be random variables following Poisson-statistics. The expected number of true events (N_{net}) due to the ^{22}Ne(p,γ)^{23}Na reaction was calculated as follows:

$$N_{\mathrm{net}} = \xi_{\mathrm{Ne}} - \frac{t_{\mathrm{Ne}}}{t_{\mathrm{BG}}}\xi_{\mathrm{BG}} - C\Big(\xi_{\mathrm{Ar}} - \frac{t_{\mathrm{Ar}}}{t_{\mathrm{BG}}}\xi_{\mathrm{BG}}\Big) \tag{4.9}$$

where t_{Ne}, t_{Ar} and t_{BG} are the real-times of the corresponding measurements. The C scaling factor between the in-beam measurements with ^{22}Ne and $^{\mathrm{nat}}$Ar was calculated by comparing the number of counts in the ROI of ^{11}B(p,γ)^{12}C reaction (see Sec. 4.1) for the two spectra.

The mean of the Poisson distributions was set equal to the raw number of events in the ^{22}Ne(p,γ)^{23}Na ROI of the corresponding experimental spectrum without any normalisation applied. For each beam energy the Monte-Carlo code was run 100000 times to obtain distribution of the NET counting rate N_{net}. Based on its probability density function, upper limits on the counting rate with 90% confidence level were determined.

In addition to this Monte-Carlo based method, the upper limits were also determined based on the profile likelihood approach suggested by Wolfgang Rolke [54]. The method is implemented in the TRolke class of ROOT [55], however the current version only allows one source of background - which can be either Poisson or Gaussian distributed. (The signal events are always considered Poisson distributed.)

Therefore, total background rate in the experiment was estimated by an additional Monte Carlo simulation: the beam-induced and natural background were considered Poisson distributed, and the sum of the backgrounds were calculated. The Gaussian mean and sigma of the resulting distribution were used as input for the Rolke approach. The upper limits corresponding to 90% confidence level were determined.

The results for both methods are summarized in Table 4.5. The proton beam energy in the center of the target chamber was given as resonance energy for the obtained upper limits on $\omega\gamma$ (Eq. 4.2). The assigned uncertainty on the resonance energy in Table 4.5 reflects the energy interval spanned by the beam inside the 108 mm long target chamber.

As can be seen in Fig. 4.9, the upper limits based on the Rolke approach are generally higher than the ones produced by the Monte Carlo method. While for the measurements at 65.8 and 73.8 keV, the upper limits from the two different methods are comparable, in case of the experimental points at 67.7 and 69.6 keV there is a larger discrepancy. The difference can be explained by the fact that in these runs the expected rate of background was higher than the rate of signal events. Therefore, in the Monte Carlo simulation only a small fraction of the probability density function (of the net counting rate) was above zero, which led to lower upper limits.

During the experiment the beam energy was chosen so that the individual energy regions overlap with each other (see Fig. 4.9). The investigated energy range spans from 62.3 to 77.6 keV, and therefore it completely covers the 71 ± 5 keV range originally reported by Powers *et al.* [29]. Consequently, if a narrow resonance does exist in this energy region, its resonance strength cannot be higher than 5.8×10^{-11} eV.

As it was emphasized in Sec. 3.4, the determination of the add-back detection efficiency relies on the knowledge of the exact decay scheme of the excited state under study. For the tentative resonances at $E_p^{\mathrm{lab}} = 71$ and 105 keV, however, the branching ratios are unknown [32]. Moreover, the arbitrary $1/2^+$ spin and parity assignment [30] of these states is yet to be confirmed by experiment.

Fortunately, in case of the $E_x = 8829.5$ keV level, corresponding to the resonance at $E_p^{\mathrm{lab}} = 37$ keV, the branching ratios are well-known [32]: $R \to 2391$ with $64 \pm 10\%$, and $R \to 0$ with $36 \pm 10\%$. Since this state has similar energy, and its spin/parity assignment is also $1/2^+$, it may be assumed that the decay scheme of the resonances at 71 and 105 keV follow the same pattern. However, some other possible scenarios were also tested with the help of the Monte Carlo code, in order to determine the sensitivity of the simulated add-back efficiency for the branching ratios. The results are listed in Table 4.4.

As expected, a single ground state transition yields the highest efficiency, while the detection of γ-rays is less efficient when the de-excitation proceeds via a cascade of several MeV γ-rays ($R \to 3678$, $R \to 2391$). If the branching ratios from the $E_x = 8829.5$ keV level are adopted, the simulated efficiency lies between the two extremes. As a conservative assumption, the upper limits (listed in Table 4.5) were based on the lowest value $\eta_{\mathrm{eff}}^{71} = 42\%$.

Table 4.4: Add-back detection efficiencies for the resonances at $E_p^{\rm lab}$ = 71 and 105 keV

Transition	Multipolarity	Branching [%]			
$R \rightarrow 3678$	E1	-	-	-	100
$R \rightarrow 2391$	M1	64	-	100	-
$R \rightarrow 0$	M1	36	100	-	-
Efficiency (71 keV):		52.9 %	64.5 %	46.3 %	42.3 %
Efficiency (105 keV):		52.1 %	63.8 %	45.5 %	41.1 %

Table 4.5: Upper limits on the $\omega\gamma$ for the resonance at $E_p^{\rm lab} = 71$ keV

$E_{\rm target}$ [keV]	$\omega\gamma_{\rm MC}$ [eV]	$\omega\gamma_{\rm Rolke}$ [eV]
$65.8^{+3.6}_{-3.5}$	$\leq 4.1 \times 10^{-11}$	$\leq 4.8 \times 10^{-11}$
$67.7^{+3.7}_{-3.5}$	$\leq 7.7 \times 10^{-12}$	$\leq 2.6 \times 10^{-11}$
$69.6^{+3.7}_{-3.5}$	$\leq 1.4 \times 10^{-11}$	$\leq 2.3 \times 10^{-11}$
$73.8^{+3.8}_{-3.6}$	$\leq 4.5 \times 10^{-11}$	$\leq 5.8 \times 10^{-11}$

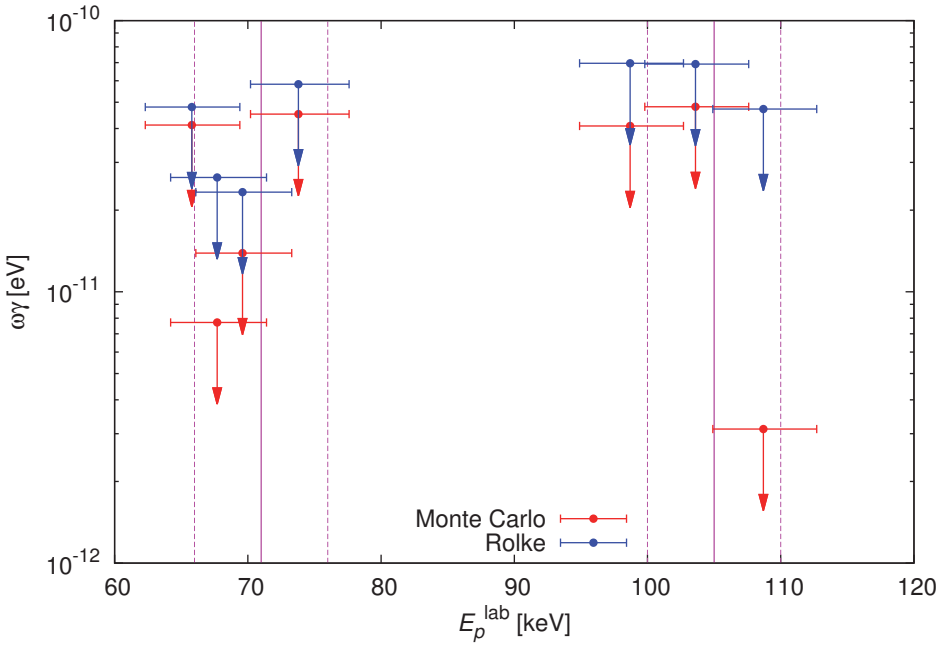

Figure 4.9: Upper limits on the strength of resonance $E_p^{\rm lab}$= 71 and 105 keV. The vertical lines show the resonance energy and its uncertainty reported by Powers *et al.* [29].

4.2.2 105 keV resonance

The measurements regarding the resonance at $E_p^{\text{lab}} = 105$ keV were carried out in a similar fashion as for the resonance at $E_p^{\text{lab}} = 71$ keV. Experimental yields were measured at three different proton beam energies around the suggested literature energy of the resonance. During the analysis the experimental ROI was shifted to 8.40-9.40 MeV, in order to account for the difference in the level energy compared to the resonance at 71 keV. The simulated detector efficiency was slightly lower than for the 71 keV ($\eta_{\text{eff}}^{105} = 41\%$) due to the shift in the limits of the ROI (see Table 4.4). The details of the experiment are listed in Table 4.6.

The experimental spectra are shown in Figures 4.10, 4.11 and 4.12. As can be seen, at these energies there is more structure also in the high energy part of the spectra. Due to the increased beam-induced background, the role of the natural background is less prominent, however, its contribution to the total counting rate in the ROI is still around 10%.

Near the expected resonance energy of 8894 keV, a broad peak-like structure is visible in all three spectra. However, the same feature seems to be also present in the background runs with similar counting rates. Therefore, only upper limits could be derived from the data, whereas both the previously described Monte-Carlo (Eq. 4.2.1) and Rolke approach were used. The obtained upper limits are summarised in Table 4.7.

In case of the last experimental point corresponding to $E_{\text{target}} = 108.7$ keV proton energy, the Monte Carlo based derivation of upper limits fails, because the background is considerably higher than the rate of signal events. For the other two points, both method provide consistent upper limits on $\omega\gamma$, however, the values based on the Rolke method are more conservative.

The three experimental points completely cover the suggested 105 ± 5 keV energy range by Powers *et al.* [29] (see Fig. 4.9). Therefore, if a resonance exists in this range, its strength cannot be higher than 7.0×10^{-11} eV.

Table 4.6: Experimental parameters for the resonance at $E_p^{\text{lab}} = 105$ keV: E_p^{ini} and E_{target} correspond to the initial proton energy, and beam energy at the center of the target chamber in the laboratory frame, respectively. q is the integrated charge based on the calorimetric beam current measurement, t is the measurement time, and p_t stands for the target pressure.

		^{22}Ne gas			$^{\text{nat}}$Ar gas		
E_p^{ini} [keV]	E_{target} [keV]	q [C]	t [h]	p_t [mbar]	q [C]	t [h]	p_t [mbar]
105.5 ± 0.3	98.7 ± 0.5	14.2 ± 0.2	22.1	2.00	16.1 ± 0.3	23.3	0.92
110.5 ± 0.3	103.6 ± 0.5	28.7 ± 0.6	67.3	2.00	27.8 ± 0.6	61.3	0.94
115.5 ± 0.3	108.7 ± 0.5	40.3 ± 0.6	62.6	2.00	32.0 ± 0.5	44.4	0.95

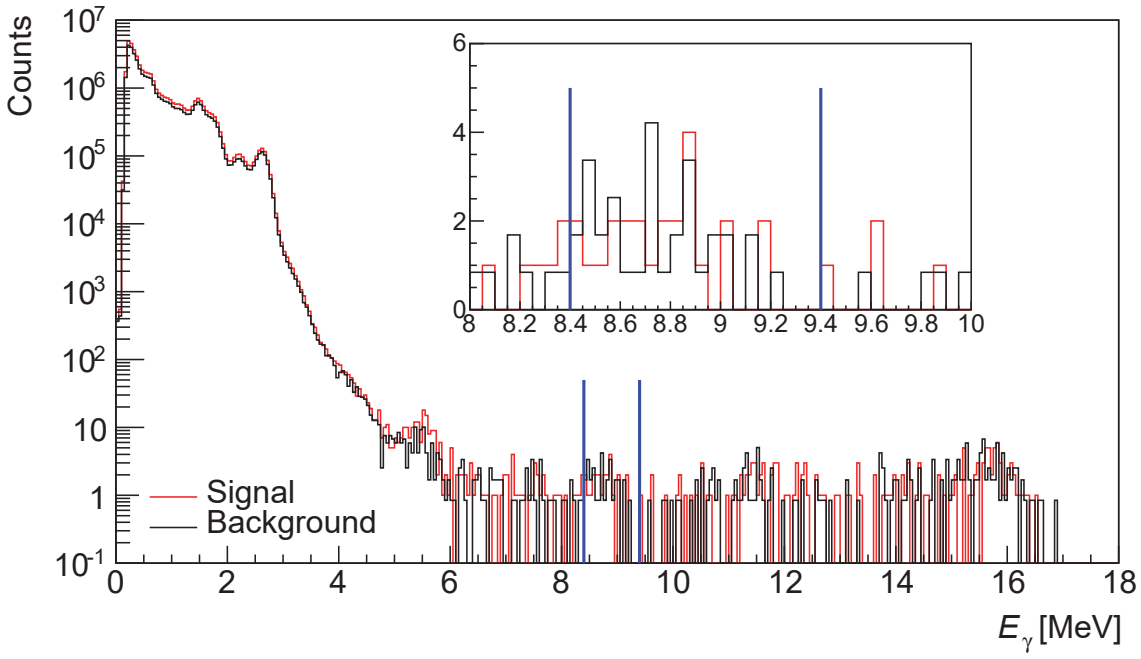

Figure 4.10: Experimental spectra at $E_p^{\mathrm{ini}} = 105.5$ keV.

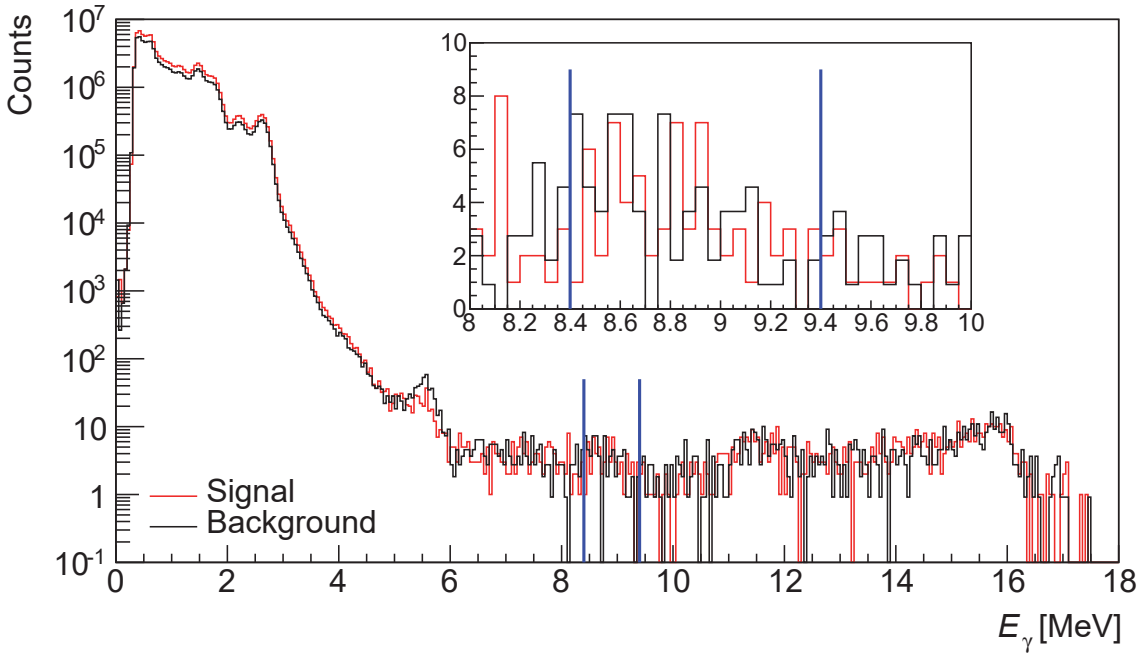

Figure 4.11: Experimental spectra at $E_p^{\mathrm{ini}} = 110.5$ keV.

Table 4.7: Upper limits on the $\omega\gamma$ for the resonance at $E_p^{\rm lab} = 105$ keV

$E_{\rm target}$ [keV]	$\omega\gamma_{\rm MC}$ [eV]	$\omega\gamma_{\rm Rolke}$ [eV]
$98.7^{+4.0}_{-3.8}$	$\leq 4.1 \times 10^{-11}$	$\leq 7.0 \times 10^{-11}$
$103.6^{+4.0}_{-3.8}$	$\leq 4.8 \times 10^{-11}$	$\leq 6.9 \times 10^{-11}$
$108.7^{+4.0}_{-3.8}$	$\leq 3.1 \times 10^{-12}$	$\leq 4.7 \times 10^{-11}$

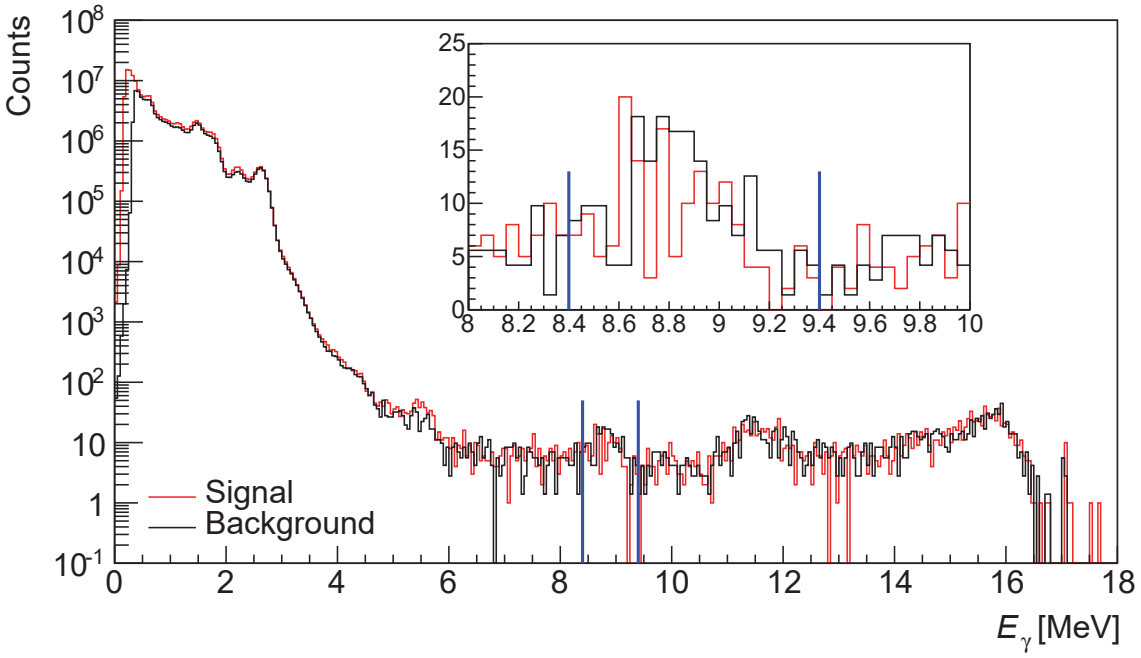

Figure 4.12: Experimental spectra at $E_p^{\rm ini} = 115.5$ keV.

4.2.3 156.2 keV resonance

The resonance at $E_p^{\mathrm{lab}} = 156.2$ keV proton energy has been successfully observed in the previous, HPGe-based experimental phase in LUNA. In order to confirm the reported resonance strength [33], its value was remeasured in the present experiment. As a first step, a resonance scan was performed to determine the proton beam energy corresponding to the resonance in the new target chamber. Based on the yield curve (see Fig. 4.13), the initial proton beam energy was set to $E_p^{\mathrm{ini}} = 163.9$ keV and statistics were collected for half a day. Further details of the measurement are summarised in Table 4.11 at the end of Sec. 4.2.

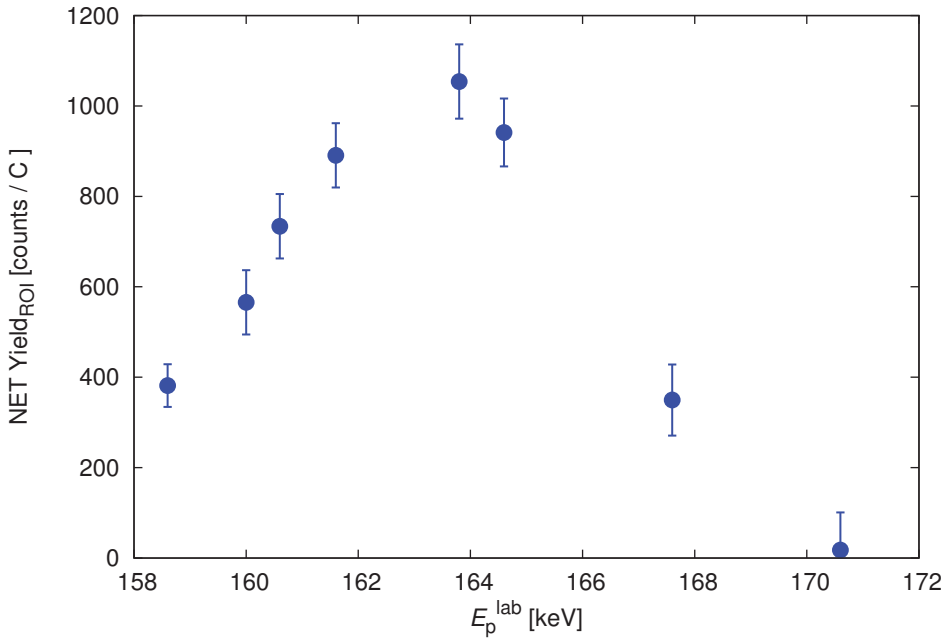

Figure 4.13: Scan of the resonance at $E_p^{\mathrm{lab}} = 156.2$ keV

Because of the higher beam energy, the beam induced background also became more significant compared to the spectra at lower energies. For example, in case of the measurement at $E_p^{\mathrm{ini}} = 105.5$ keV (Fig. 4.10) the counting rate in the ^{11}B(p,γ)^{12}C region (11-18 MeV) was about 6.3 counts/h, while at $E_p^{\mathrm{ini}} = 163.9$ keV it was 3300 counts/h. On one hand, this approximately 500 times increase meant more Compton events for the ^{22}Ne(p,γ)^{23}Na ROI around 9 MeV, but on the other hand made the background normalization and subtraction more reliable: in only hours enough statistics could be acquired to allow the normalization of the $^{\mathrm{nat}}$Ar spectrum to the one in ^{22}Ne with 1% uncertainty. Therefore, more time could be allocated for the study of the resonance itself. Moreover, the appearance of distinct structures in the high energy part of the spectra made it easier to judge the quality of the background subtraction.

As can bee seen in Fig. 4.14, the dominant contaminants are the ^{11}B(p,γ)^{12}C and ^{18}O(p,γ)^{19}F reactions. Despite the fact, that the high energy part of the spectra is basically determined by the γ-peaks from the ^{11}B(p,γ)^{12}C reaction, the presence of ^{18}O is far more problematic: its full energy sum peak is located directly next to the region of interest, which was selected from 8.5 to 9.5 MeV.

The validity of this choice becomes more evident from Fig. 4.15, which shows

the NET spectrum after background subtraction. Within the selected ROI, the experimental spectrum is in excellent agreement with the predicted peak shape by the Monte-Carlo simulation (shown in red). Looking only at the spectra taken in ^{22}Ne and ^{nat}Ar, one might except the high energy tail of the ^{18}O(p,γ)^{19}F peak has some contribution in the ROI. Fortunately, from Fig. 4.15 it is clear that it is not the case.

As it was already emphasised in the previous chapters, for the correct simulation of the add-back efficiency the knowledge of the decay scheme of the excited level is necessary. The $E_x = 8943.5$ keV state corresponding to the resonance at $E_p^{lab} = 156.2$ keV is known to decay into the 2391 and 3914 keV states. The most recent branching ratios regarding these γ-transitions are from the previous LUNA experimental campaign on ^{22}Ne(p,γ)^{23}Na reaction [38] and the measurement conducted by Kelly *et al.* [37] at TUNL (see Table 4.8).

Table 4.8: Branching ratios for the resonance at $E_p^{lab} = 156.2$ keV

γ-transition	E_γ [keV]	Branching [%] TUNL [37]	LUNA-HPGe [38]	LUNA-BGO		J^π
R$\rightarrow$ 0	8943	-	-	-	5 ± 1	$\frac{3}{2}^+ \rightarrow \frac{3}{2}^+$
R$\rightarrow$ 2391	6552	20 ± 4	23 ± 4	34 ± 4	32 ± 3	$\frac{3}{2}^+ \rightarrow \frac{1}{2}^+$
R$\rightarrow$ 3914	5029	80 ± 6	77 ± 4	66 ± 4	63 ± 3	$\frac{3}{2}^+ \rightarrow \frac{5}{2}^+$
Efficiency:		41.4%	41.6%	41.7%	42.7%	

Simulations were carried out subsequently with each of the two reported branching ratios and compared to experimental spectra. Taking advantage of the fact that all data were recorded in list mode, a conditional filter was applied to the recorded events: only those add-back events were allowed, which had an energy 8.5 MeV $\leq E \leq$ 9.5 MeV. This gating procedure was applied both for the experimental and simulated spectra. From the add-back events which satisfied the condition, the single events were extracted corresponding to single counts in the individual detector crystals. These single events were then simply summed together without considering coincidence effects, creating a so-called single-sum spectrum. Before comparison with the simulation, the experimental spectra taken in ^{22}Ne was corrected for the beam induced background, by scaling and then subtracting the single-sum spectrum of the beam induced background recorded in ^{nat}Ar.

It is apparent from Fig. 4.16, that both recommendations regarding the branching ratios fail to properly reproduce the experimental spectrum. Therefore, the branching ratios were redetermined based on the present data: Two template spectra were created by simulating the transitions $R \rightarrow 2391$ and R$\rightarrow$ 3914 separately. If the gated experimental spectrum is free from background, and there are only the above mentioned γ-transitions present, then it should be possible to reconstruct it as a "mixture" of the two templates:

$$\text{Experimental} = A_{2391} \times \text{Template}_{2391} + A_{3914} \times \text{Template}_{3914} \tag{4.10}$$

where parameters A_{2391} and A_{3914} are the corresponding branching ratios. Based on this assumption, a fitting procedure was created using the MINUIT minimizer class of ROOT [55]. The resulting new branching ratios are listed in Table 4.8.

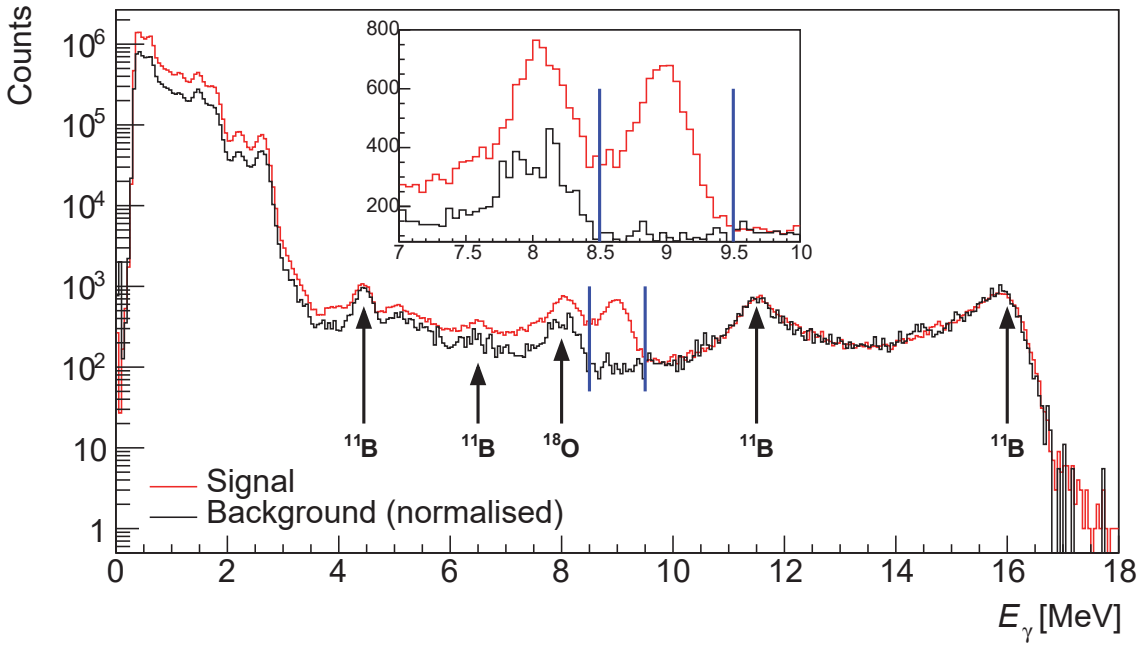

Figure 4.14: Experimental spectrum at $E_p^{\text{ini}} = 163.9$ keV for the study of the resonance at $E_p^{\text{lab}} = 156.2$ keV.

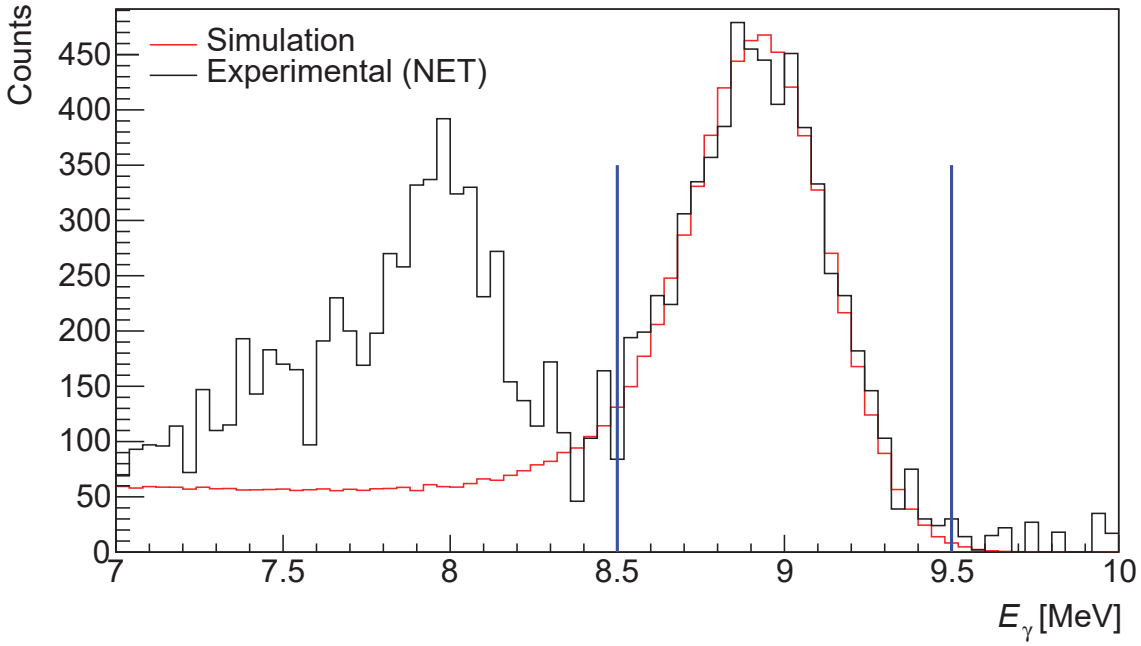

Figure 4.15: Comparison between the experimental NET (after background subtraction) and the simulated spectra for the resonance at $E_p^{\text{lab}} = 156.2$ keV

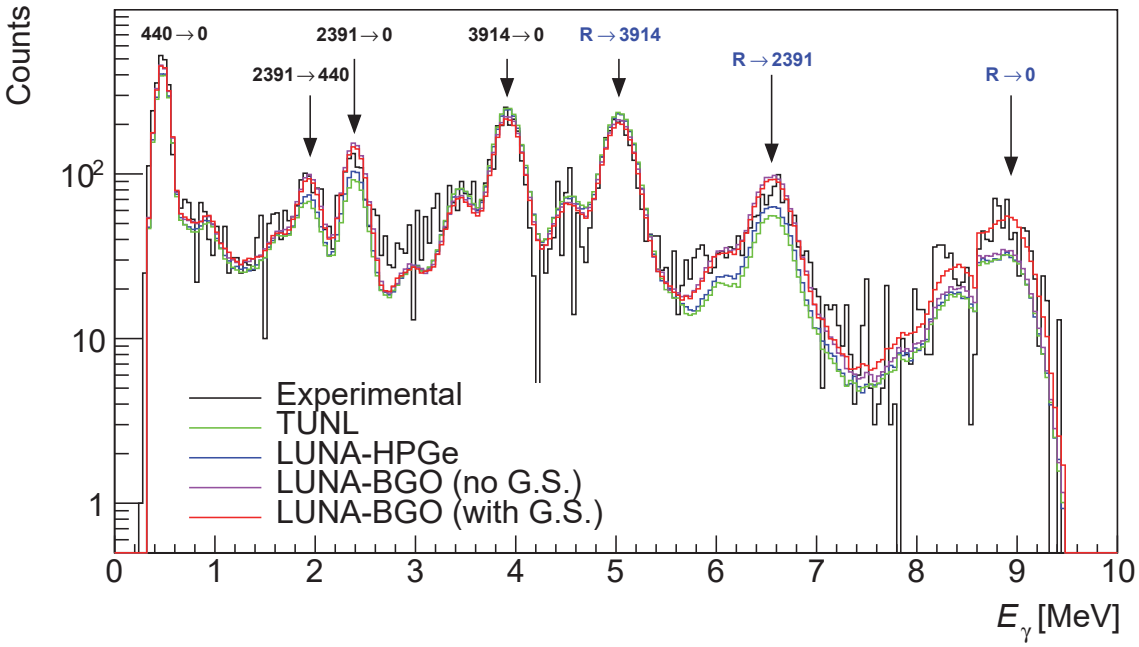

Figure 4.16: Comparison of the gated experimental single-sum spectrum to the simulated ones based on the different decay schemes in case of the resonance at $E_p^{\text{lab}} = 156.2$ keV. Primary transitions are indicated in blue.

While the readjusted branching ratios provide a better agreement between the experiment and simulation (Fig. 4.16), the reproduction of the peak around the total level energy ($E_x = 8943$ keV) of resonance is not perfect. This peak arises due to the fact, that the individual segments of the detector are so large, that the consecutive gammas from the decay of the resonance have a good chance hitting the same segment. However, it seems that this self-summing effect could not entirely account for the number of counts observed in the experimental spectrum. This suggests that a small fraction of γ-transitions proceeds directly to the ground state. Therefore, a template for the $R \rightarrow 0$ transition was created. With the help of the above described fitting procedure, the contribution form the ground state was estimated to be $5 \pm 1\%$.

Based on the new recommended branching ratios, the add-back detection efficiency was estimated to be $\eta_{\text{eff}}^{156} = 43 \pm 2\%$. Since the variation of the efficiency between the different sets of branching ratios listed in Table 4.8 is minimal, the uncertainty is mainly dominated by the modelling of the BGO geometry in the Monte Carlo code (see Sec. 3.4).

The resulting experimental resonance strength was:

$$\omega\gamma = [1.84 \pm 0.04_{\text{stat}} \pm 0.09_{\text{sys}}] \times 10^{-7} \quad \text{eV} \tag{4.11}$$

In case of the resonance energy, the previous literature value of $E_p^{\text{lab}} = 156.2$ keV [38] was accepted.

4.2.4 189.5 keV resonance

The strength of the second resonance reported by LUNA [38] at $E_p^{\text{lab}} = 189.5$ keV was also remeasured in the current experiment. Based on the resonance scan shown in Fig. 4.17, the proton beam energy was set to $E_p^{\text{ini}} = 196.4$ keV. The main measurement in ^{22}Ne gas lasted 16.2 hours, followed by a 1 hour long background run in $^{\text{nat}}$Ar. Further details of the experiment can be found in Table 4.11.

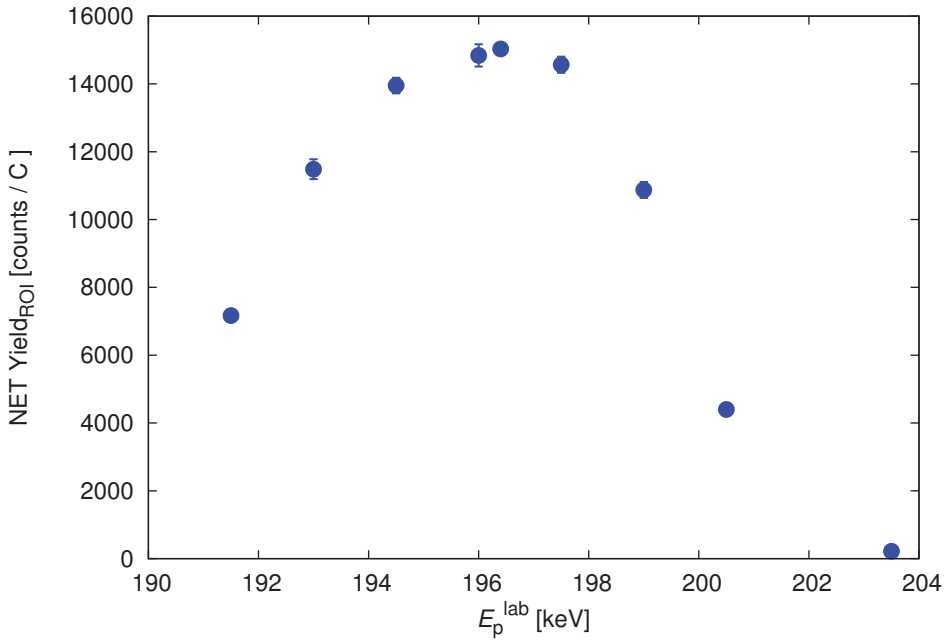

Figure 4.17: Scan of the resonance at $E_p^{\text{lab}} = 189.5$ keV

The background spectrum was normalised based on the integrated number of counts from 11 to 18 MeV. With respect to the beam induced background, the spectra are dominated by the various peaks of the ^{11}B(p,γ)^{12}C, however, the signature of the ^{14}N(p,γ)^{15}O and / or ^{13}C(p,γ)^{14}N reactions are also visible around 7.5 MeV.

The peak corresponding to the ^{22}Ne(p,γ)^{23}Na reaction has a broad, non-Gaussian shape, and its large Compton-continuum extends down to 5 MeV. A closer look reveals, this asymmetry of ^{22}Ne add-back peak is most likely caused by the presence of a second γ-peak centered around 8.5 MeV. This energy is close to, but not equal to the one, where the add-back peak from the ^{18}O(p,γ)^{19}F contaminant reaction ($Q = 7.993$ MeV) is expected (see Table 4.1). Moreover, the spectrum taken in $^{\text{nat}}$Ar does not show any sign of a ^{18}O contamination.

Fortunately, the origin of the peak in question can be explained by the decay scheme of the resonance [37, 38]. From Table 4.9 it is evident, that after the resonant capture of a proton, there is a high probability of a γ-transition to the $E_x = 440$ keV level. The incomplete summing of the resulting 8.5 MeV, and the consecutive 440 keV photons can lead to the formation of a peak in the add-back spectrum at 8.5 MeV. The overlap between this and the complete sum peak can account for the asymmetry of the observed ^{22}Ne add-back peak.

This explanation was verified with the help of a Monte Carlo simulation. The shape of the add-back peak was simulated using the branching ratios from the previous LUNA experimental phase and compared to the experimental spectrum after

background subtraction. As can be seen in Fig. 4.19, the simulation by default fails to reproduce the shape of the observed add-back peak. This suggests that during the measurement the detector lost more 440 keV photons than it was expected.

During the experiment, all BGO crystals were used with the same DAQ settings (see Table 3.1). However, during this particular measurement crystal segment Nr. 6 exhibited increased noise levels, which affected the counting rate in the low energy end of the spectrum, and more importantly the dead time. Therefore, the trigger threshold was increased for the problematic segment. Taking into account this difference in the trigger levels, a good agreement could be reached between the simulation and the experiment.

Table 4.9: Branching ratios for the resonance at $E_p^{\mathrm{lab}} = 189.5$ keV

γ-transition	E_γ [keV]	Branching [%] TUNL [37]	LUNA-HPGe [38]	LUNA-BGO	J^π
R$\rightarrow$ 0	8975.3	5.3 ± 1.4	-	-	$\frac{5}{2}^+ \rightarrow \frac{3}{2}^+$
R$\rightarrow$ 440	8535.3	37.7 ± 1.5	42.8 ± 0.9	38.0 ± 0.9	$\frac{5}{2}^+ \rightarrow \frac{5}{2}^+$
R$\rightarrow$ 2076	6899.3	39.8 ± 1.3	47.9 ± 0.9	50.6 ± 0.9	$\frac{5}{2}^+ \rightarrow \frac{7}{2}^+$
R$\rightarrow$ 2982	5993.3	5.0 ± 0.8	3.7 ± 0.5	3.2 ± 0.5	$\frac{5}{2}^+ \rightarrow \frac{3}{2}^+$
R$\rightarrow$ 3678	5297.3	2.2 ± 0.8	-	2.2 ± 0.2	$\frac{5}{2}^+ \rightarrow \frac{3}{2}^-$
R$\rightarrow$ 3914	5061.3	3.1 ± 0.6	1.1 ± 0.3	2.0 ± 0.5	$\frac{5}{2}^+ \rightarrow \frac{5}{2}^+$
R$\rightarrow$ 4775	4200.3	≤ 3.0	1.8 ± 0.2	1.6 ± 0.2	$\frac{5}{2}^+ \rightarrow \frac{7}{2}^+$
R$\rightarrow$ 6618	2357.3	4.7 ± 0.9	2.7 ± 0.2	2.4 ± 0.2	$\frac{5}{2}^+ \rightarrow \frac{3}{2}^+ \frac{5}{2}^+ \frac{7}{2}^+$
Efficiency:		60.3%	60.9%	60.0%	

Apart from the add-back spectrum, the validity of the simulation was also checked with respect to the single-sum mode. This was especially important, because again two different sets of branching ratios are reported in the literature (see Table 4.9): The most recent measurement by Kelly *et al.* (TUNL) [37] not only provides slightly different values of the branching ratios, but also reports two additional transitions, which were not observed in case of the LUNA-HPGe experiment [38].

The Monte-Carlo code was run with both branching sets, and then the resulting simulated spectra were compared to the experimental results by using the same gating method described in the previous chapter. In this case, the singles-sum spectra were built from those add-back events which had an energy 8.0 MeV $\leq E \leq$ 9.5 MeV. The results are shown in Fig. 4.20.

The two most intense primary transitions (R$\rightarrow$ 440 and R$\rightarrow$ 2076) are reasonably well reproduced with both sets of branching. However, the transition to the ground state suggested by Kelly *et al.* [37] does not seems to be justified by the present experiment. Moreover, the TUNL branching ratios result in a general overestimation in the energy range from 2 to 6 MeV due to the higher intensity given to transitions R$\rightarrow$ 2982, R$\rightarrow$ 3678, R$\rightarrow$ 3914, R$\rightarrow$ 4775 and R$\rightarrow$ 6618.

The LUNA branching ratios [38] in general provide a better, but not perfect description of the experimental spectrum. The simulated spectrum somewhat underestimates the counting rate in regions 3-4 and 5-6 MeV. This suggest that the actual intensity of transitions R$\rightarrow$ 3678 and R$\rightarrow$ 3914 might be slightly higher than reported by the LUNA-HPGe phase.

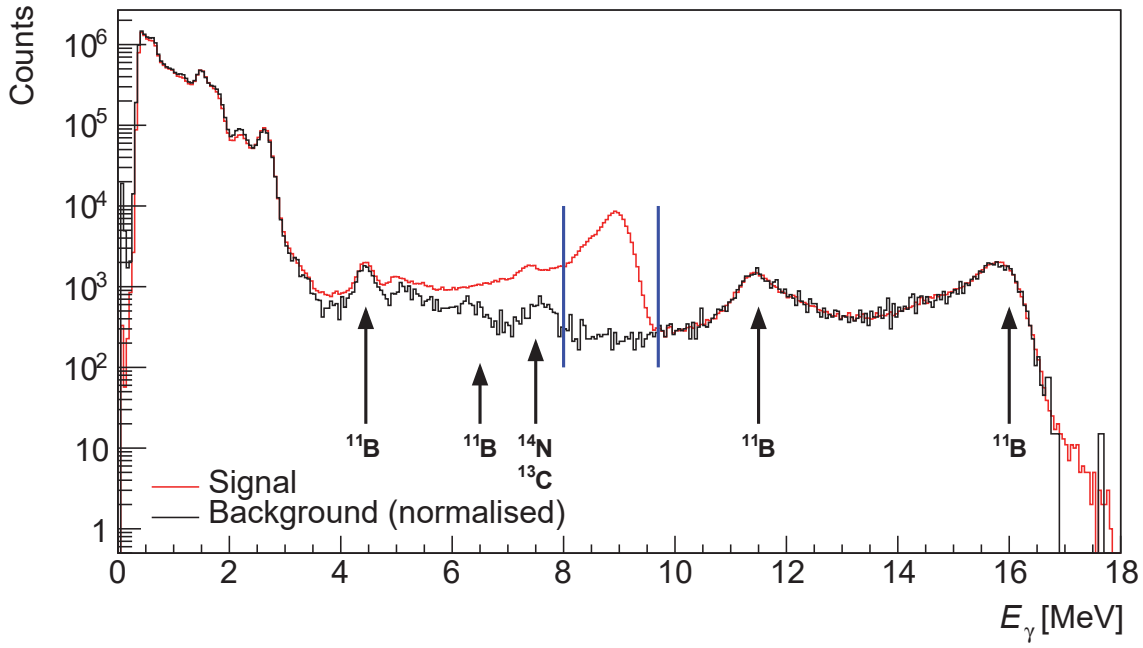

Figure 4.18: Experimental spectra at $E_p^{\text{ini}} = 196.4$ keV for the study of the resonance at $E_p^{\text{lab}} = 189.5$ keV.

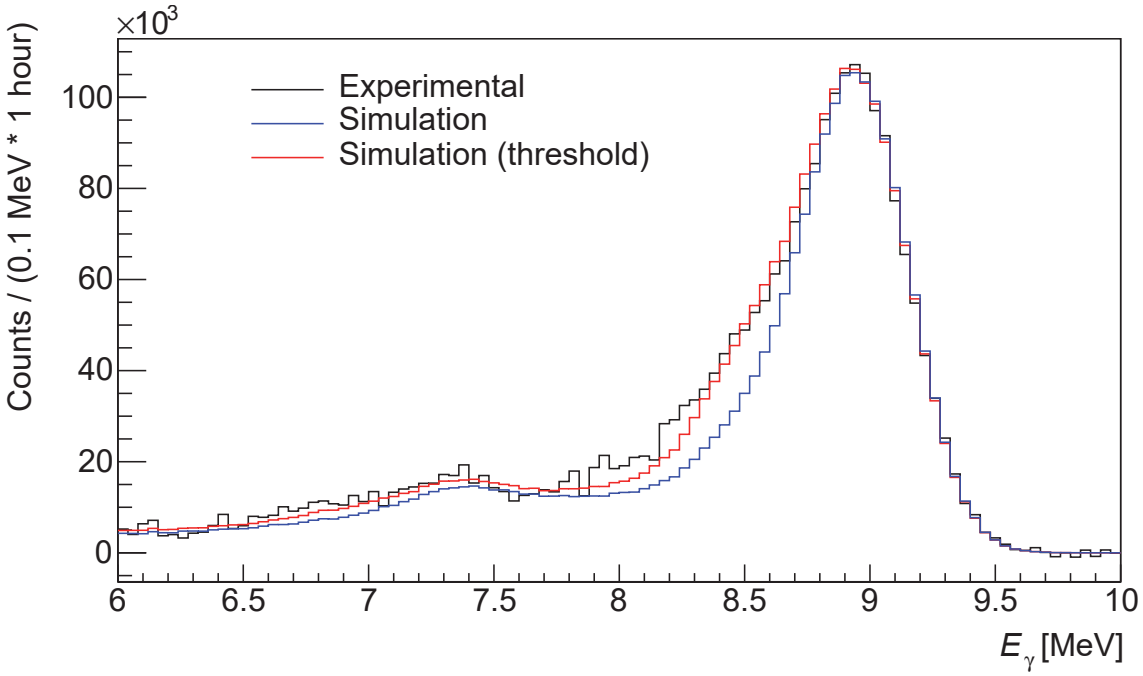

Figure 4.19: Comparison of experimental NET (after background subtraction) and simulated add-back peak for the resonance at $E_p^{\text{lab}} = 189.5$ keV. The blue curve shows the predicated shape of the add-back peak based on the LUNA branching ratios from Table 4.9, while the red curve also takes into account that one of the detector crystals had a higher trigger threshold than the others.

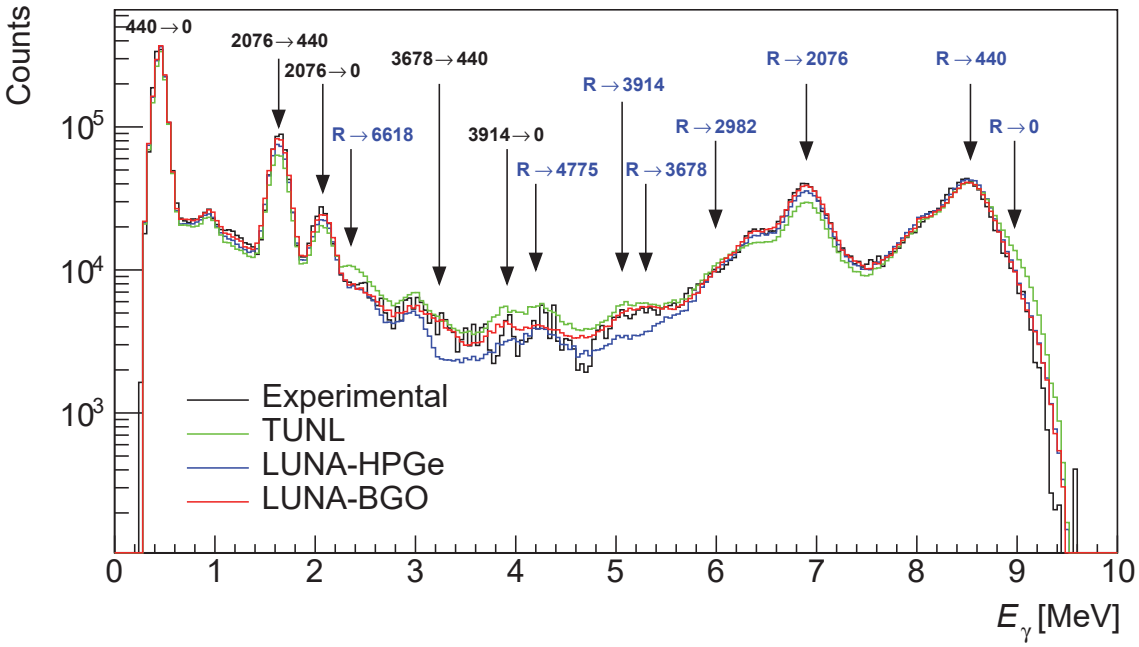

Figure 4.20: Comparison of the gated experimental single-sum spectrum to the simulated ones based on the different decay schemes in case of the resonance at $E_p^{\text{lab}} = 189.5$ keV. Primary transitions are indicated in blue.

Therefore, the branching ratios were redetermined adopting the same fitting procedure as in Sec. 4.2.3. The results is very similar to the previous LUNA recommendation (see Table 4.9), although, it was necessary for the better reproduction of the experimental spectrum to increase the strength of transitions R→ 3678 and R→ 3914. This also improves the matching between the simulated and experimental spectra in the region 3-4 MeV, because of the intense secondary transitions 3678 → 440 and 3914 → 0. The fit, however, did not justify the 5.3% probability of a ground state transition suggested by the TUNL measurement.

The new branching ratios are listed in Table 4.9 along with the previous literature values. The final simulation of the resonance was based on this updated decay scheme, and the add-back detection efficiency was found to be $\eta_{\text{eff}}^{189} = 60 \pm 2\%$ for the selected experimental ROI (8.0-9.7 MeV) shown in Fig. 4.18. The three sets of the branching ratios result in similar detection efficiencies, therefore the uncertainty is mainly arising from the simulation of the detector geometry.

The resulting experimental resonance strength was:

$$\omega\gamma = [2.28 \pm 0.02_{\text{stat}} \pm 0.10_{\text{sys}}] \times 10^{-6} \quad \text{eV} \tag{4.12}$$

For the resonance energy, the previous literature value of $E_p^{\text{lab}} = 189.5$ keV [38] was accepted.

4.2.5 259.7 keV resonance

Unlike the previously discussed two resonances, the resonance at $E_p^{\text{lab}} = 259.7$ keV was not studied in the most recent measurement at TUNL [36, 37]. Therefore, the only value on its $\omega\gamma$ is known from direct measurement performed at LUNA [38]. In

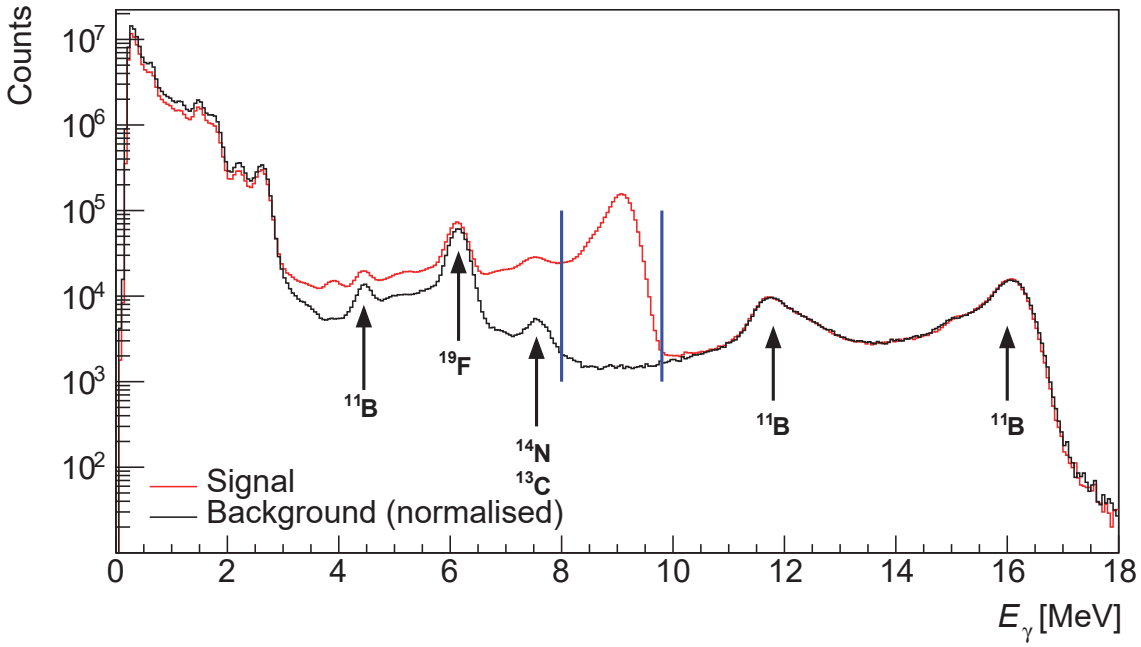

Figure 4.21: Experimental spectra at E_p^{ini}= 265.0 keV for the study of the resonance at E_p^{lab} = 259.7 keV.

order to confirm the reported resonance strength, this resonances was also remeasured in the current experiment. The details of the measurement are summarised in Table 4.11.

The signature of the ^{22}Ne(p,γ)^{23}Na reaction is clearly visible in the experimental spectrum (Fig. 4.21). It produces a broad add-back peak between 8 and 10 MeV, with a considerable Compton-tail extending towards lower energies. With respect to the contaminant reactions, the most visible difference compared to Fig. 4.19, is the appearance of the peak of the ^{19}F(p,$\alpha\gamma$)^{16}O reaction at 6.1 MeV. Despite its intensity, the ^{19}F peak is less important than the weaker one produced by the ^{14}N(p,γ)^{15}O (or ^{13}C(p,γ)^{14}N) reaction around 7.6 MeV, which lies next to the region of interest.

Still, most of the beam induced background originates from ^{11}B(p,γ)^{12}C. As can be seen in Fig. 4.19, the integrated number of counts from this reaction (in the region of 10-18 MeV) provides a good basis for normalisation of the spectra. As the excellent matching between the spectra taken in ^{22}Ne and $^{\mathrm{nat}}$Ar reveals, the beam induced background under the ^{22}Ne(p,γ)^{23}Na peak region (ROI 8.0-9.8 MeV) is nearly constant.

With respect to the decay scheme of the resonance, the previously reported branching ratios [38] provide a reasonable description of the experimental spectra (see Fig. 4.22). However, in case of the transitions R$\rightarrow$ 5927 and R$\rightarrow$ 6042, the simulation seems to slightly overestimate the height of the experimentally observed peak. This issue can be addressed by a minor reduction in the intensity of these transitions. The new branching ratios are summarised in Table 4.10 along with the originally recommended ones.

It is worth to note, the in both cases the simulation fails to reproduce the experimental spectra in two regions: near 1.2 MeV and 4.2 MeV the predicted curves

underestimate the observed one. Neither of these regions are directly affected by the reported primary transitions. Moreover, the following secondary transitions do not produce gammas corresponding to these energies. Therefore, it is most likely that this 0.8% excess over the simulated spectrum is due to some kind of unidentified background or random summing of gammas in the detector crystals, which is not correctly reproduced in the simulation.

Table 4.10: Branching ratios for the resonance at $E_p^{\text{lab}} = 259.7$ keV

γ-transition	E_γ [keV]	Branching [%]		J^π
		LUNA-HPGe [38]	LUNA-BGO	
R$\rightarrow$ 440	8602	45.4 ± 0.9	46.0 ± 0.9	$\frac{7}{2}^+\frac{9}{2}^+ \rightarrow \frac{5}{2}^+$
R$\rightarrow$ 2076	6963	18.7 ± 0.6	18.9 ± 0.6	$\frac{7}{2}^+\frac{9}{2}^+ \rightarrow \frac{7}{2}^+$
R$\rightarrow$ 2704	6335	10.9 ± 0.5	11.0 ± 0.5	$\frac{7}{2}^+\frac{9}{2}^+ \rightarrow \frac{9}{2}^+$
R$\rightarrow$ 3848	5193	13.3 ± 0.5	13.5 ± 0.5	$\frac{7}{2}^+\frac{9}{2}^+ \rightarrow \frac{5}{2}^-$
R$\rightarrow$ 3914	5127	1.8 ± 0.4	1.8 ± 0.4	$\frac{7}{2}^+\frac{9}{2}^+ \rightarrow \frac{5}{2}^+$
R$\rightarrow$ 5927	3115	3.6 ± 0.2	3.0 ± 0.2	$\frac{7}{2}^+\frac{9}{2}^+ \rightarrow \frac{7}{2}^+$
R$\rightarrow$ 6042	3000	2.6 ± 0.2	2.0 ± 0.2	$\frac{7}{2}^+\frac{9}{2}^+ \rightarrow \frac{7}{2}^-$
R$\rightarrow$ 6355	2686	1.5 ± 0.2	1.5 ± 0.2	$\frac{7}{2}^+\frac{9}{2}^+ \rightarrow \frac{9}{2}^-$
R$\rightarrow$ 6820	2221	2.2 ± 0.2	2.2 ± 0.2	$\frac{7}{2}^+\frac{9}{2}^+ \rightarrow \frac{5}{2}^-$
Efficiency		60.1%	60.2%	

The evaluated add-back efficiency was $\eta_{\text{eff}}^{260} = 60 \pm 2\%$ for this resonance and the resonance strength was found to be

$$\omega\gamma = [8.74 \pm 0.03_{\text{stat}} \pm 0.39_{\text{sys}}] \times 10^{-6} \quad \text{eV} \tag{4.13}$$

based on the integrated number of counts in the experimental ROI (8.0-9.8 MeV). The already established literature value of resonance energy $E_p^{\text{lab}} = 259.7$ keV [38] was accepted also in this case.

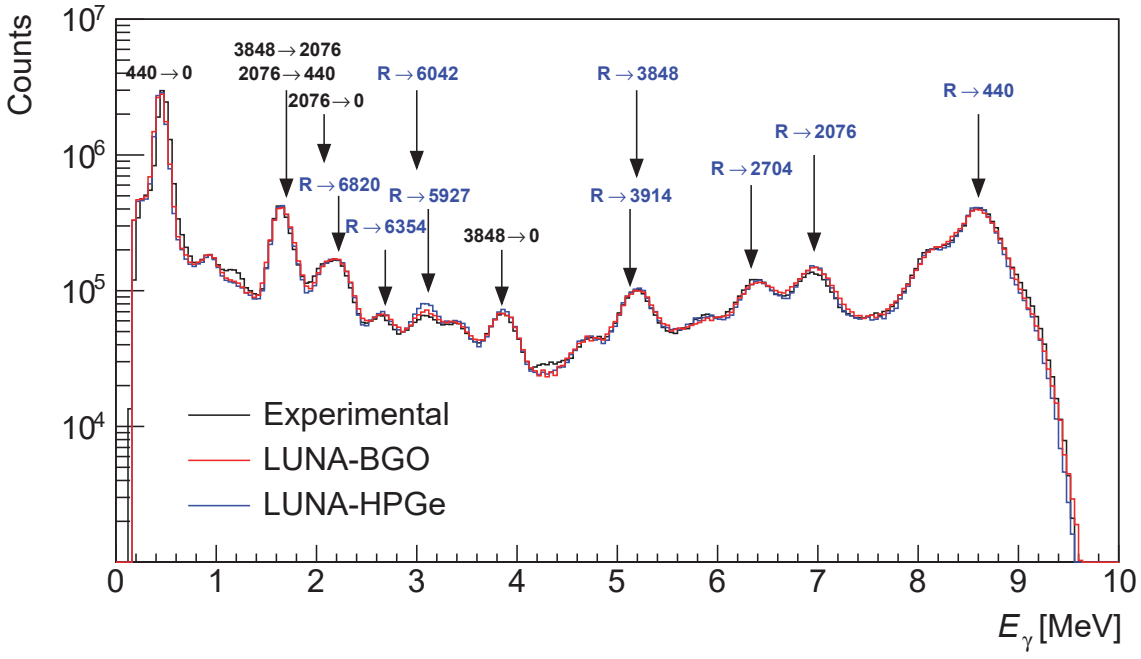

Figure 4.22: Comparison of the gated experimental single-sum spectrum to the simulated ones based on the different decay schemes in case of the resonance at $E_p^{\text{lab}} = 259.7$ keV. Primary transitions are indicated in blue.

Table 4.11: Experimental parameters for the resonances at $E_p^{\text{lab}} = 156.2$, 189.5 and 259.7 keV

		^{22}Ne gas			$^{\text{nat}}$Ar gas		
E_p^{ini} [keV]	E_{target} [keV]	q [C]	t [h]	p_t [mbar]	q [C]	t [h]	p_t [mbar]
163.9 ± 0.3	157.2 ± 0.5	6.3 ± 0.1	12.4	2.00	0.77 ± 0.01	1.5	1.06
196.4 ± 0.3	189.9 ± 0.5	8.0 ± 0.1	16.2	2.00	0.27 ± 0.01	1.0	1.13
265.0 ± 0.3	259.1 ± 0.5	47.3 ± 0.5	48.1	2.00	27.2 ± 0.5	35.3	1.22

4.3 Non-resonant capture reaction

In the case of a narrow resonance, the reaction happens at a well-defined energy (E_{res}), therefore the point of interaction is well localised inside the target chamber. On the other hand, the direct capture reaction mechanism can take place at any energy. Consequently, the source of the gamma photons is spread out along the beam axis. Every point of the gas target, where the beam hits the ^{22}Ne gas, contributes to the total non-resonant reaction yield (Y_{DC}) in the BGO:

$$Y_{DC} = \int_{E_0-\Delta E}^{E_0} \frac{\sigma(E)}{\epsilon(E)} dE \tag{4.14}$$

where E_0 is initial center-of-mass energy of the target-projectile system, ΔE is the energy loss of the beam in the target, and $\epsilon(E)$ is the stopping power. By expressing the reaction cross section $\sigma(E)$ with the help of the astrophysical S-factor $S(E)$ (see Eq. 1.8), the yield can be written as

$$Y_{DC} = S(E_{\text{eff}}) \int_{E_0-\Delta E}^{E_0} \frac{1}{\epsilon(E)} \frac{1}{E} \exp(-2\pi\eta) dE \tag{4.15}$$

Since typically $\Delta E \leq 10$ keV, the S-factor can be assumed to be constant. Therefore, it can be moved in front of the integration by evaluating its value at E_{eff} effective beam energy. E_{eff} is usually defined as the energy at which one-half of the total yield (for the full target thickness) is obtained:

$$\int_{E_{\text{eff}}}^{E_0} \frac{1}{\epsilon(E)} \frac{1}{E} \exp(-2\pi\eta) dE = \frac{1}{2} \int_{E_0-\Delta E}^{E_0} \frac{1}{\epsilon(E)} \frac{1}{E} \exp(-2\pi\eta) dE \tag{4.16}$$

Following the notation of Chapter 1, Eq. 4.15 and 4.16 were expressed here in the center-of-mass frame. However, for an experimentalist it is often more intuitive to use quantities defined in the laboratory frame. For example, in the laboratory the stopping powers can directly be adopted from the well-known SRIM compilation [56]. Fortunately, the yield Y_{DC} as physical quantity is independent from the frame of reference, therefore, the integral in Eq. 4.15 can also be calculated with the initial beam energy E_p^{ini} and energy loss ΔE_p measured in the laboratory frame:

$$Y_{DC} = S(E_{\text{eff}}) \int_{E_p^{\text{ini}}-\Delta E_p}^{E_p^{\text{ini}}} \frac{1}{\epsilon(E)} \frac{1}{E} \exp(-2\pi\eta) dE \tag{4.17}$$

where the Sommerfeld-paramter (see Eq. 1.4) has to be evaluated taking into account the following conversion

$$E_{\text{cm}} = \frac{M_t}{M_t + M_p} E_p^{\text{lab}} \tag{4.18}$$

with M_t and M_p as the atomic mass of target and projectile respectively.

It is important to note, that Eq. 4.17 in its present form does not take into account that the detector has an efficiency $\eta_{\text{eff}} \leq 1$. Moreover, η_{eff} is not constant, but it varies as a function of the position along the beam axis. Therefore, the efficiency has to be evaluated point-by-point with the help of the Monte Carlo simulation.

As it was already mentioned in the previous chapter, the add-back efficiency also depends on the branching ratio of different γ-transitions involved in the decay

of an excited state. Therefore, in case of the direct capture process the capture probabilities to the different excited states are needed as input parameters for the simulation. Unfortunately, there is no information available at the low energies discussed here: In 1983 Görres *et al.* studied the direct capture cross sections at a beam energy of 1.22 MeV [40], while most recently Kelly *et al.* reported cross section data at 425 keV [37].

Table 4.12: Most important transitions for the direct capture ^{22}Ne(p,γ)^{23}Na at $E_p^{\text{ini}} = 1.22$, 0.425 and 0.310 MeV, showing their relative intensity. The given efficiency is calculated for the center of the target, assuming point-like γ-emission.

Transition [keV]	J_f^π	Intensity (%) Görres [40] (1.22 MeV)	Kelly [37] (0.425 MeV)	Adopted (0.310 MeV)	Multipolarity s-wave	p-wave
DC→ 0	$\frac{3}{2}^+$	9.5	31.1	53.6	M1	E1
DC→ 440	$\frac{5}{2}^+$	22.1	11.6	8.3	E2	E1
DC→ 2391	$\frac{1}{2}^+$	31.5	18.6	15.3	M1	E1
DC→ 2982	$\frac{3}{2}^+$	10.7	7.2	0.0	M1	E1
DC→ 6306	$\frac{1}{2}^+$	6.9	5.9	4.6	M1	E1
DC→ 6918	$\frac{3}{2}^-$	4.9	1.5	1.1	E1	M1
DC→ 7080	$\frac{3}{2}^-$	2.2	3.0	2.1	E1	M1
DC→ 7488	$\frac{1}{2}^-$, $\frac{3}{2}^-$	1.4	2.1	1.5	E1	M1
DC→ 8664	$\frac{1}{2}^+$	9.9	15.2	10.9	M1	E1
DC→ 8829	$\frac{1}{2}^+$	0.9	3.6	2.6	M1	E1
Efficiency:		50.8 %	54.0 %	57.3 %		

As can be seen in Table 4.12, both evaluations of direct capture cross sections place the emphasis on the transitions to low lying excited states: DC→ 0, DC→ 440, DC→ 2391 and DC→ 2982. However, there are differences with respect to the strongest one: at 1.22 MeV one third of the transition results in level $E_x = 2391$ keV, while in case of the data at 425 keV the ground state transition bears the main importance. For the rest of the transitions both experiments see comparably low intensities. The only exception is level $E_x = 8664$ keV, which has 10-15 % capture probability.

With respect of the multipolarity of transitions, the capture process is characterised by mostly p-wave transitions. Despite the higher centrifugal barrier, p-wave transitions are more advantageous in case of positive parity states. On the other hand, s-wave transitions are preferred for levels with negative parity.

Due to the lack of information at lower energies, it was assumed that only the transitions listed in Table 4.12 have significance for the direct capture process in the present experimental energy range. Their relative intensities were used as input for the Monte Carlo simulation. The resulting spectra were then compared to the experimental one obtained at $E_p^{\text{ini}} = 310$ keV. As in the previous chapter, the comparison was done by using gated single-sum spectra which only included events with total add-back energy 8.6 MeV $\leq E \leq$ 9.5 MeV.

From Fig. 4.23 it is evident that neither the Görres [40] nor the Kelly [37] data could reproduce the experimental spectra. Therefore, the transition probabilities

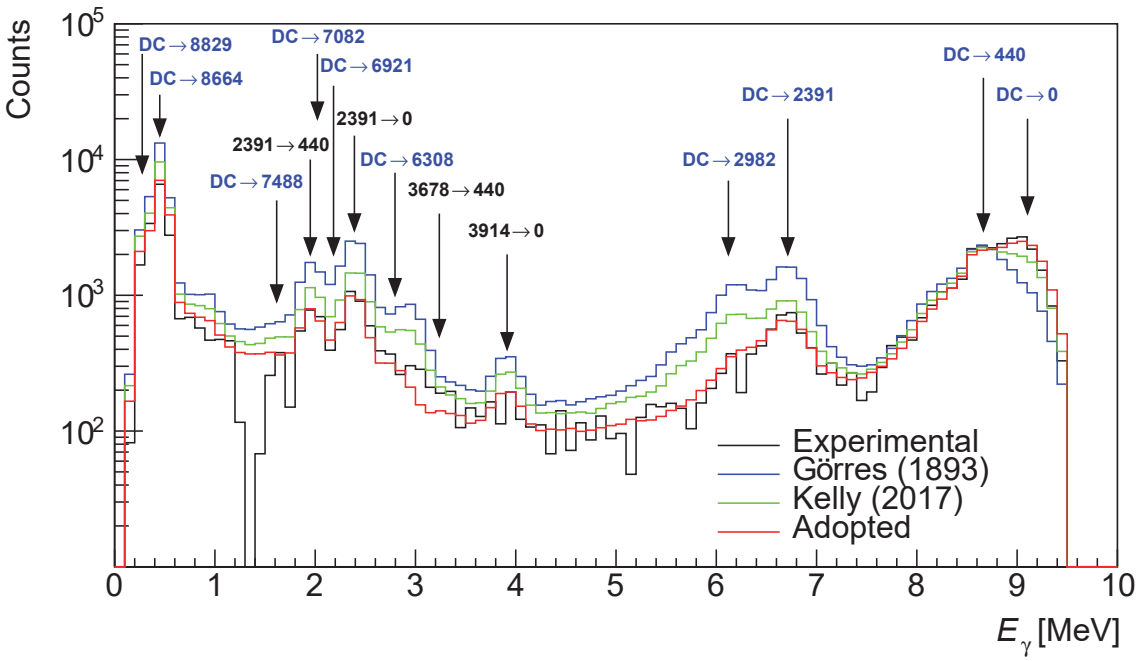

Figure 4.23: Comparison of the observed and simulated direct capture transitions at $E_p^{\text{ini}} = 310$ keV using gated single-sum spectra. The transitions from Table 4.12 are indicated in blue, while the secondary transitions are shown in black.

were adjusted until a reasonable agreement with the experimental spectrum was achieved. The adopted ,,branching ratios" are reported in the Table 4.12. However, it is important to note, that these values not necessarily represent the actual transition probabilities due to the difficulties associated with the localisation of the γ-emission in case of the experiment. Moreover, the limited statistics makes a precise determination of the strength of the individual transitions difficult. Therefore, it is safer to consider the adopted numbers only as arbitrary input parameters of the Monte Carlo model without much emphasis on their physical meaning. For the same reason no uncertainty is quoted on them.

The resulting trend of add-back efficiency as function of the position inside the target chamber is presented in Fig. 4.24 along with density profile already presented in Fig. 3.9.

The efficiency peaks in the center of the chamber, where it has a plateau around 60%. In the close vicinity of the calorimeter, the efficiency starts to drop, because the massive copper body of the calorimeter absorbs a large fraction of the gamma photons. Towards the collimator, the efficiency also decreases due to the shielding effect of the collimator on the front portion of the BGO crystals. Inside the collimator the efficiency is about half of its maximum value, which is consistent with the fact, that the gamma photons have to propagate through 2 cm material made of copper and stainless-steel before reaching the BGO crystal. In first centimetres of the interconnection tube, the detection efficiency shows a slight increase, because the walls of the tube are only 2 mm thick, thus the attenuation of γ-photons is lower. Moving further away from the collimator, the efficiency starts to decrease again, as the solid angle covered by the BGO detector becomes smaller and smaller.

In order to take into account this strong variation of detection efficiency (and

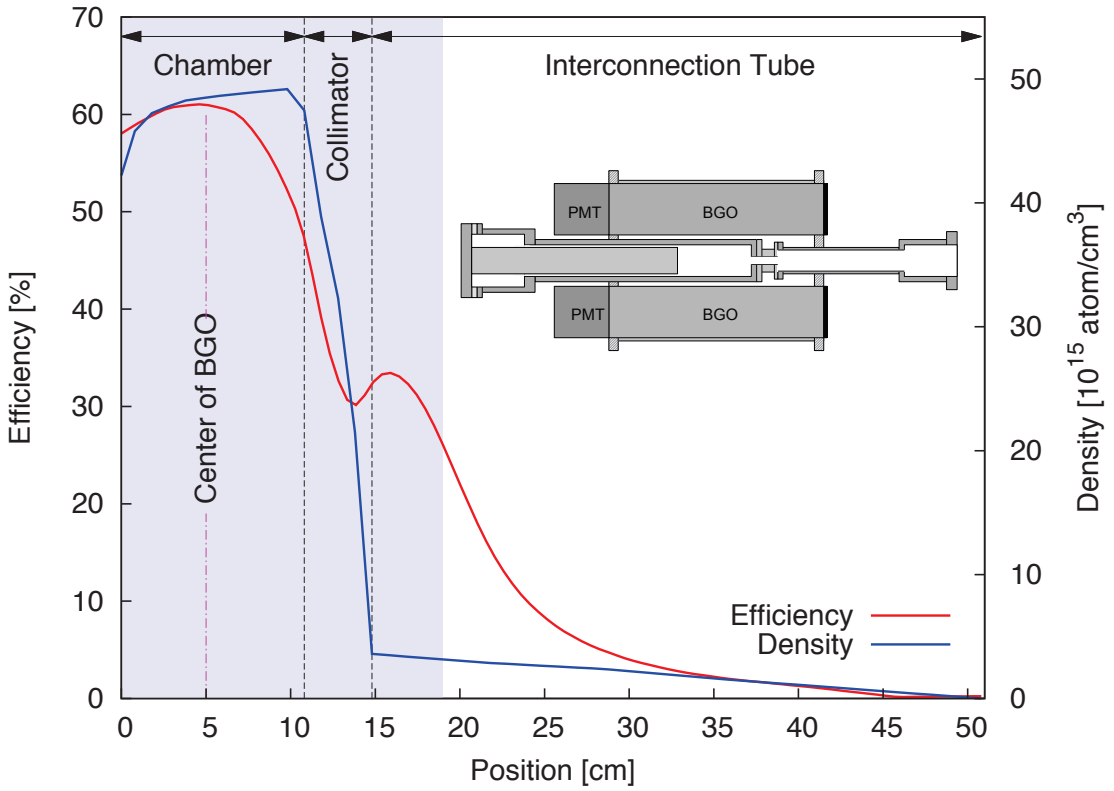

Figure 4.24: Simulated add-back detection efficiency for the direct capture process, shown along with the gas density as function of position. The position is measured from the hot side of the calorimeter towards the first pumping stage of the vacuum system. The shaded area represent the portion of the target chamber covered by the BGO detector. The basic design of the target chamber with BGO detector is also shown.

gas density) along the path of the beam, the following approach was implemented to determine the S-factor via numerical integration:

1. The total length of the gas target (including the chamber, collimator and interconnection tube) was divided into sections of 1 mm length. Within each section, the detection efficiency and the gas density were assumed to be constant.

2. The beam reaches the i-th section with initial energy E_i. Considering that the length of the section is L_i, the energy loss ΔE_i can be calculated as follows:

$$\Delta E_i = \epsilon_i(E_i) n_i L_i \tag{4.19}$$

   where n_i is the local gas density and $\epsilon_i(E_i)$ is the stopping power. Consequently, the outgoing beam energy will be

$$E_{i+1} = E_i - \epsilon_i n_i L_i \tag{4.20}$$

3. The contribution of i-th section to the total experimental yield is obtained by evaluating the integral of Eq. 4.17 numerically in the energy range between E_i

and E_{i+1}

$$I_i = \eta_i^{\text{eff}} \sum_j \frac{1}{\epsilon(E_i^{\text{av}})} \frac{1}{E_{ij}} \exp\left(-2\pi\eta(E_{ij}) \right) \Delta E_{\text{incr}} \tag{4.21}$$

with $E_i^{\text{av}} = (E_i + E_{i+1})/2$ and $E_{ij} = E_i + j\Delta E_{\text{incr}}$. η_i^{eff} is the local detection efficiency in the ith section, and $\Delta E_{\text{incr}} = (E_{i+1} - E_i)/j$ is the energy step size.

4. Step 2 and 3 are then repeated for section i+1, with initial energy E_{i+1}.

5. The direct capture S-factor is assumed to be constant over the studied energy range, and thus it is obtained by dividing the experimentally measured yield based on number of counts in the ROI by the sum of all partial integrals I_i

$$S = Y_{\text{Exp}} / \sum_i I_i \tag{4.22}$$

6. Finally, the effective energy E_{eff} corresponding to the half of the yield was calculated according to Eq. 4.16.

The direct capture component was studied at four beam energies: $E_p^{\text{ini}} = 188.0$, 205.2, 250.1, and 310.0 keV. These energies were chosen so that within the energy range spanned by the beam in the target chamber no resonance of the ^{22}Ne(p,γ)^{23}Na reaction was excited.

At the lowest beam energy E_p^{ini}= 188.0 keV (see Fig. 4.25), the beam-induced background is almost exclusively due to the ^{11}B(p,γ)^{12}C reaction. Apart from the full energy add-back peak at 16.1 MeV, the 11.6 MeV and 4.4 MeV gammas from the $R \rightarrow 4438 \rightarrow 0$ transition, and 6.5 MeV peak from the $R \rightarrow 9641 \rightarrow 0$ transition are also visible. The wide peak around 7.5 MeV is possibly due to a minor contribution from ^{14}N(p,γ)^{15}O. Based on its Q-value ($Q = 7.551$ MeV), the ^{13}C(p,γ)^{14}N reaction is also a possible candidate .

Furthermore, it is worth to note, that for energies higher than 15 MeV, the matching between the Ne and Ar spectra is less good. The full energy add-back peak of the ^{11}B(p,γ)^{12}C reaction is somewhat wider for the Ne spectrum than for the one measured in argon. This could suggest a change in the resolution or the linearity of detector between the two measurements.

At E_p^{ini}=205.2 keV, in addition to previously described signature from the ^{11}B(p,γ)^{12}C reaction, a peak at 8.2 MeV appears due to the well-known ^{18}O(p,γ)^{19}F resonance at E_p^{lab}=151 keV [57]. The fact that this resonance only becomes apparent at higher beam energies, suggest that the contamination is not in the gas, but implanted in either the collimator or the calorimeter. As can be seen in Fig. 4.26, the region affected by the ^{18}O(p,γ)^{19}F reaction is very close to the ^{22}Ne ROI.

With further increase in the beam energy, at E_p^{ini}=250.1 keV (see Fig. 4.27), the ^{19}F$(p, \alpha\gamma)^{16}$O reaction [58] becomes the dominant source of beam induced background. Fluorine is a common component of heat conducting pastes, therefore the ^{19}F is most likely localised on the calorimeter. Its resonance at $E_p^{\text{lab}} = 223.9$ keV populates the level at 13.086 MeV in ^{20}Ne, from where the reaction proceeds with emission of an α-particle to the 6.130 MeV excited level of ^{16}O. Thus, differently from the (p, γ) reactions, ^{19}F$(p, \alpha\gamma)^{16}$O does not show up at its Q-value (8.114 MeV) in the add-back spectrum, but registers at 6.1 MeV.

For the experimental spectrum taken at $E_p^{\rm ini}$=310.0 keV (see Fig. 4.28), the beam induced background is determined by the ^{19}F$(p,\alpha\gamma)^{16}$O and the ^{14}N$(p,\gamma)^{15}$O reactions. In case of the latter one, not all decays are summed into the add-back peak and the individual γ-lines at 6.79 and 5.18 MeV are also visible.

As it was described in Sec. 4.1, the beam-induced background was studied in $^{\rm nat}$Ar gas at the same beam energy as with ^{22}Ne gas. However, in case of last experiment at $E_p^{\rm ini}$=310.0 keV, the original background spectrum was showing considerably higher levels of ^{18}O contamination, affecting also the experimental ROI. Therefore, the Ar spectrum had to be discarded. Unfortunately, due to beamtime constraints the measurement could not be repeated.

On the other hand, it was found that the beam induced background in the ^{22}Ne(p,γ)^{23}Na ROI can be reliably approximated by using another spectrum taken at $E_p^{\rm ini} = 282.6$ keV in $^{\rm nat}$Ar. This measurement has lower statistics, because it was originally intended to study the nitrogen content of the $^{\rm nat}$Ar gas by exciting the strong ^{14}N$(p,\gamma)^{15}$O resonances at $E_p^{\rm lab} = 278$ keV. Because of this, the add-back peak of ^{14}N$(p,\gamma)^{15}$O is stronger in the background spectrum. On the other hand, by looking at Fig. 4.28 it is evident that with respect to the ^{19}F$(p,\alpha\gamma)^{16}$O and ^{11}B(p,γ)^{12}C regions the two spectra are properly matched. Moreover, at the higher edge of the ^{22}Ne(p,γ)^{23}Na ROI a good agreement is achieved between the trend in the background and ^{22}Ne spectra.

With respect to the low energy edge of the ROI, however, one has to be more careful, because the ^{14}N$(p,\gamma)^{15}$O peak is not properly matched in case of the two spectra. Consequently, the trend seen in the Ar spectrum might not properly describe the actual background inside the ROI. Therefore, the number of background events inside the ROI was also calculated by assuming a constant background based on the average counting rate on the right hand side of the ROI. The difference between the two background approximation methods was taken as uncertainty on the background rate.

The NET counting rates within the ^{22}Ne(p,γ)^{23}Na ROI were used to determine the corresponding S-factors. Furthermore, one can extend the information on direct capture to lower energies, by using the results from Sec. 4.2.1 and 4.2.2: Since no clear evidence was found for the tentative 71 and 105 keV resonances, the yields can be also interpreted as results of a non-resonant process (direct capture or tail contribution from wide resonances). In this sense, the obtained upper limits on the counting rate were used to determine upper limits for the S-factor at the corresponding beam energies. The results are summarized in Table 4.13.

It is important to note, that measured non-resonant yields can be affected by the tails of broad resonances. Therefore, the contribution of these resonances has to be subtracted in order to obtain the "pure" direct capture S-factor. In this respect, the importance of the $E_x = 8664$ keV ($E_{\rm res}^{\rm cm} = -130$keV, sub-threshold resonance) and $E_x = 8664$ keV ($E_{\rm res}^{\rm cm} = 35$ keV) levels were already pointed out by Görres *et al.* [40].

Their contribution to the non-resonant cross section was calculated using the single-level Breit-Wigner formula (see Eq. 1.18), where the energy dependence of the partial proton Γ_p and gamma Γ_γ widths was taken into account and s-wave resonant capture was assumed. The adopted input parameters are summarised in Table 4.14. For more details, refer to Appendix A.

Since both states are known to have $1/2^+$ spin and parity [32,43], the total cross

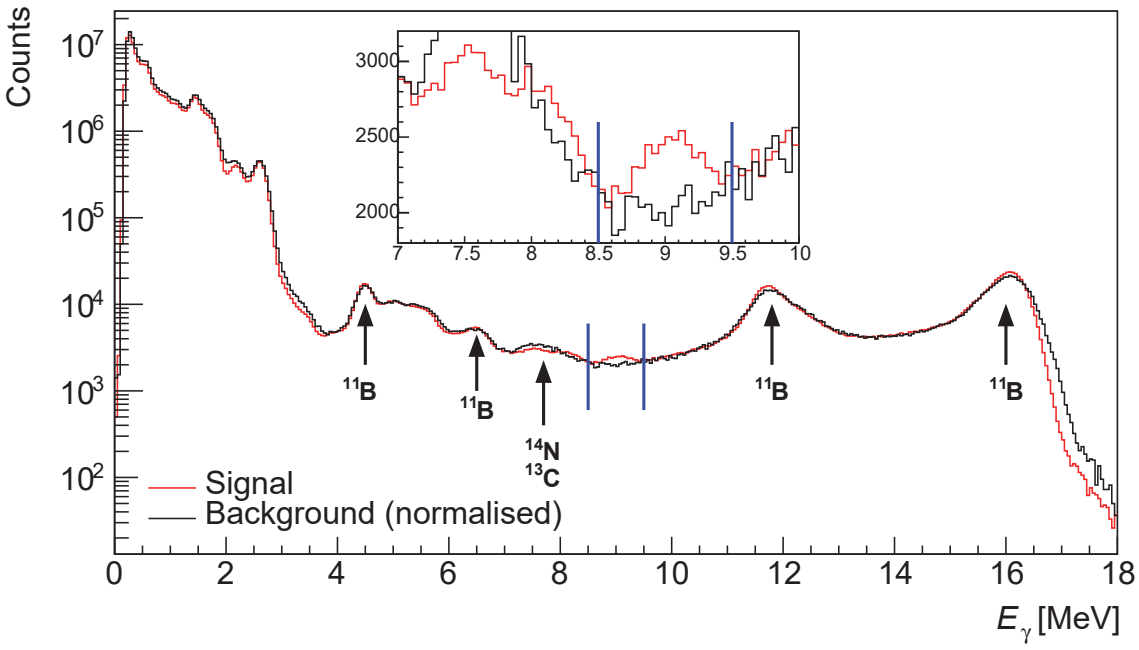

Figure 4.25: Experimental spectrum at $E_p^{\text{ini}} = 188.0$ keV

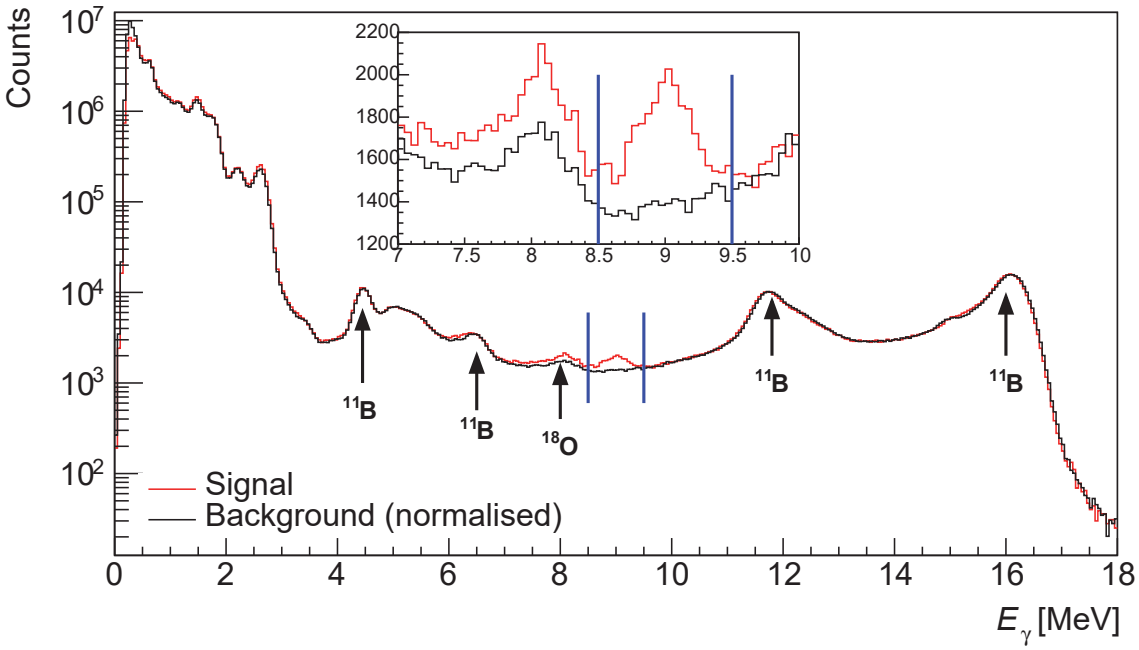

Figure 4.26: Experimental spectrum at $E_p^{\text{ini}} = 205.0$ keV

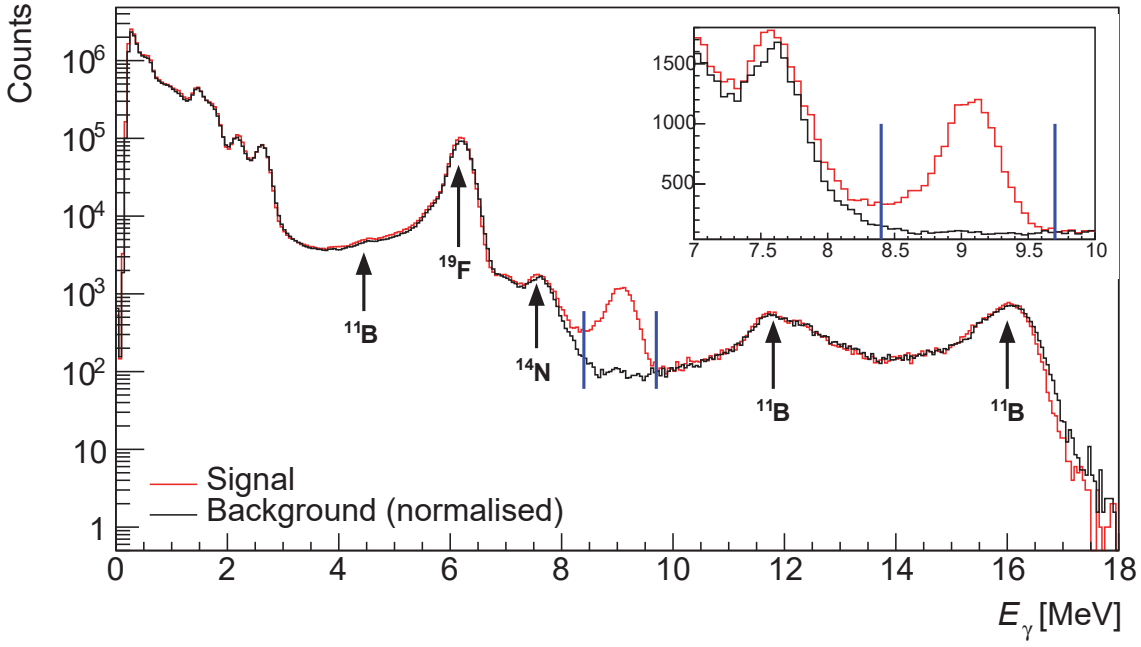

Figure 4.27: Experimental spectrum at $E_p^{\text{ini}} = 250.0$ keV

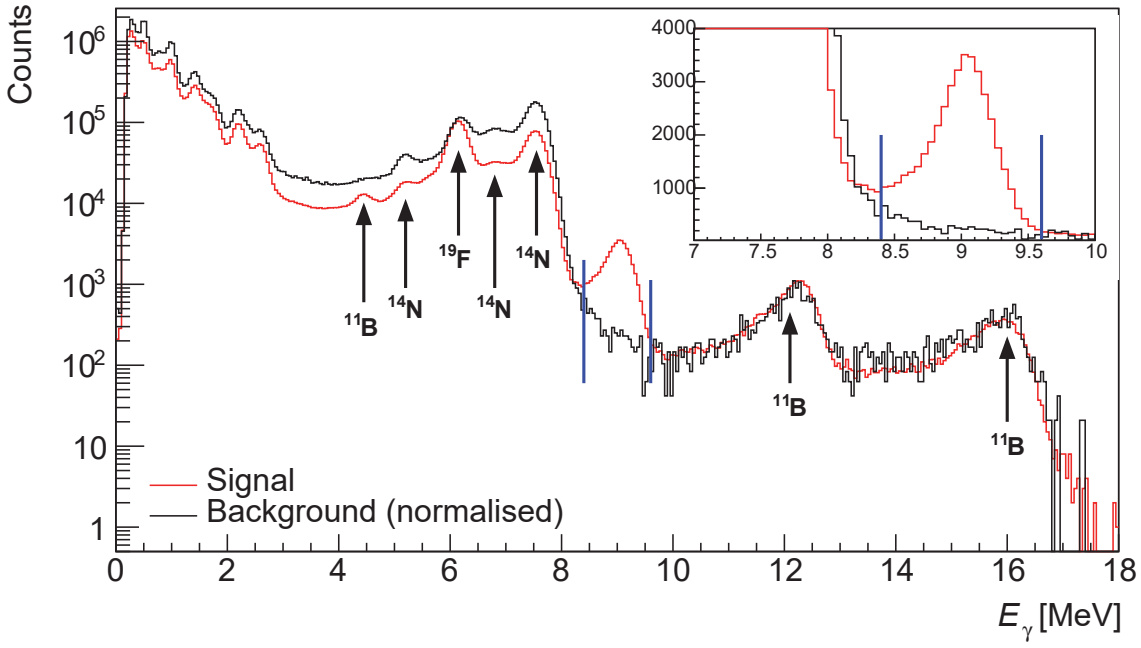

Figure 4.28: Experimental spectrum at $E_p^{\text{ini}} = 310.0$ keV. The beam induced background was taken at $E_p^{\text{ini}} = 282.6$ keV.

Table 4.13: ^{22}Ne(p,γ)^{23}Na non-resonant S-factor

$E_p^{\rm ini}$ [keV]	$E_{\rm eff}^{\rm lab}$ [keV]	S-factor [keV b] Present, experimental	Predicted*
72.1	$68.4^{+3.7}_{-5.8}$	≤ 751674	650 ± 270
74.0	$70.2^{+3.8}_{-5.8}$	≤ 81983	615 ± 250
76.0	$72.1^{+3.9}_{-5.8}$	≤ 87238	580 ± 230
80.3	$76.2^{+4.0}_{-5.8}$	≤ 97779	520 ± 200
105.5	$100.8^{+4.6}_{-5.2}$	≤ 686	320 ± 100
110.5	$105.6^{+4.8}_{-5.3}$	≤ 380	295 ± 90
115.5	$110.6^{+4.9}_{-5.1}$	≤ 186	275 ± 85
188.0	$182.9^{+5.1}_{-4.5}$	$[104.5 \pm 7.6_{\rm stat} \pm 8.5_{\rm sys}]$	124 ± 32
205.2	$200.2^{+5.0}_{-4.3}$	$[85.9 \pm 3.8_{\rm stat} \pm 6.9_{\rm sys}]$	108 ± 28
250.1	$245.3^{+4.8}_{-4.0}$	$[70.1 \pm 0.8_{\rm stat} \pm 5.6_{\rm sys}]$	76 ± 18
310.0	$305.5^{+4.5}_{-3.6}$	$[53.6 \pm 4.8_{\rm stat} \pm 4.3_{\rm sys}]$	52 ± 12

* based on previous information on broad resonances (Table 4.14)

Table 4.14: Parameters of the resonances near the proton threshold

$E_{\rm res}^{\rm cm}$		Görres et al. [40]	Assumed here	Ref.
-130 keV	J^π	$\frac{1}{2}^+$	$\frac{1}{2}^+$	[32]
	Γ_γ	4.7 ± 1.0 eV	5.1 ± 0.6 eV	[32]
	C^2S	0.30 ± 0.04	0.58	[59]
	θ^2	(1) [a]	0.68	[60]
35 keV	J^π	$\frac{1}{2}^+$	$\frac{1}{2}^+$	[32]
	Γ_γ	0.5 eV [b]	2.2 ± 1.0 eV	[41]
	Γ_p	6.8×10^{-15} eV	$(3.1 \pm 1.2) \times 10^{-15}$ eV	[41]

[a] assumed

[b] Γ_{γ_0}, with 36 ± 10 % of the transitions to the ground state

section was calculated considering interference effects:

$$\sigma(E) = \sigma_1(E) + \sigma_2(E) + 2\sqrt{\sigma_1(E)\sigma_2(E)}\cos(\delta_1 - \delta_2) \tag{4.23}$$

where the quantity δ_i represents phase of resonance i, determined by its resonance energy E_{Ri} and total width Γ_i.

$$\delta_i = \arctan\Big(\frac{\Gamma_i}{2(E - E_{Ri})}\Big) \tag{4.24}$$

In Fig. 4.29, the experimentally measured data points are consistent with the predicted trend of the S-factor within their error bars. The upper limits obtained around 71 and 105 keV are also in agreement with the predictions. The only exception is the point corresponding to $E_{\rm eff}^{\rm lab} = 110.6$ keV, where the calculated upper limit is lower then the tail contribution from two low energy resonance discussed here. This is due to the background issue already discussed in Sec. 4.2.2.

In the measurements by Görres *et al.* [40] it was found that the observed $S(E)$ values are nearly energy independent. The data were extrapolated to zero energy based on the DC model, and a constant $S = 62$ keV b was suggested. The recent measurement by Kelly *et al.* [37] is consistent with this assumption.

The present data are, however, in disagreement with the results by both authors: The observed non-resonant yields are consistent with the expected tail contribution from the broad resonances near and under the proton threshold ($E_{\rm res}^{\rm cm} = 35$ and -130 keV). Therefore, no evidence was found for a direct capture process in the investigated energy range.

Still, the non-resonant contribution to the total experimental yield from these broad resonances had to be taken into account during the study of the resonant yields. Instead of using the predicted total S-factor curve from Fig. 4.29, the experimental points were fitted with a linear function (see Fig. 4.30). In this way, the estimation of non-resonant S-factor at different energies relies only on the experimental results, and no additional uncertainty is introduced due to theoretical considerations. The $\omega\gamma$ values in Sec. 4.2 have been corrected for the non-resonant contribution using the following parametrisation:

$$S = [-0.35 \pm 0.06] + [158.7 \pm 15.7]E_p \tag{4.25}$$

The necessary correction amounted typically 2% of the observed yield for resonances at $E_p^{\rm lab} = 156.2$, 189.5 and 259.7 keV. In case of the two putative resonances at $E_p^{\rm lab} = 71$ and 105 keV, no correction was applied in order to obtain more conservative upper limits on $\omega\gamma$.

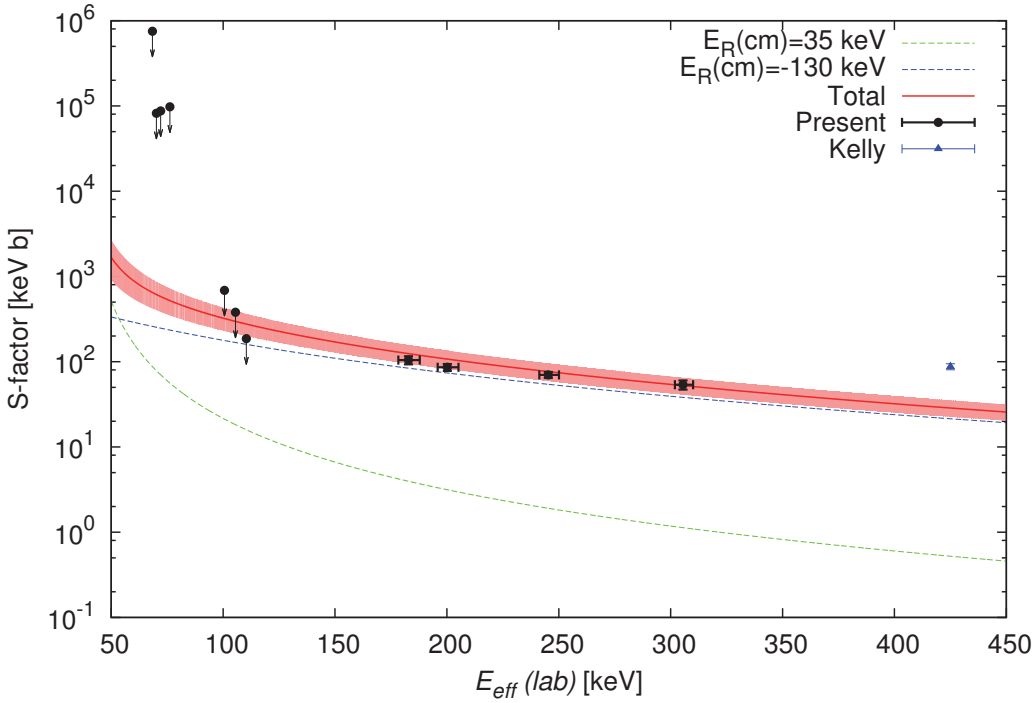

Figure 4.29: Contributions to the non-resonant S-factor from broad resonances near the proton threshold. The red curve shows the total contribution from these two resonances, while the shaded area corresponds to the uncertainty. The recent measurement by Kelly *et al.* [37] is also shown.

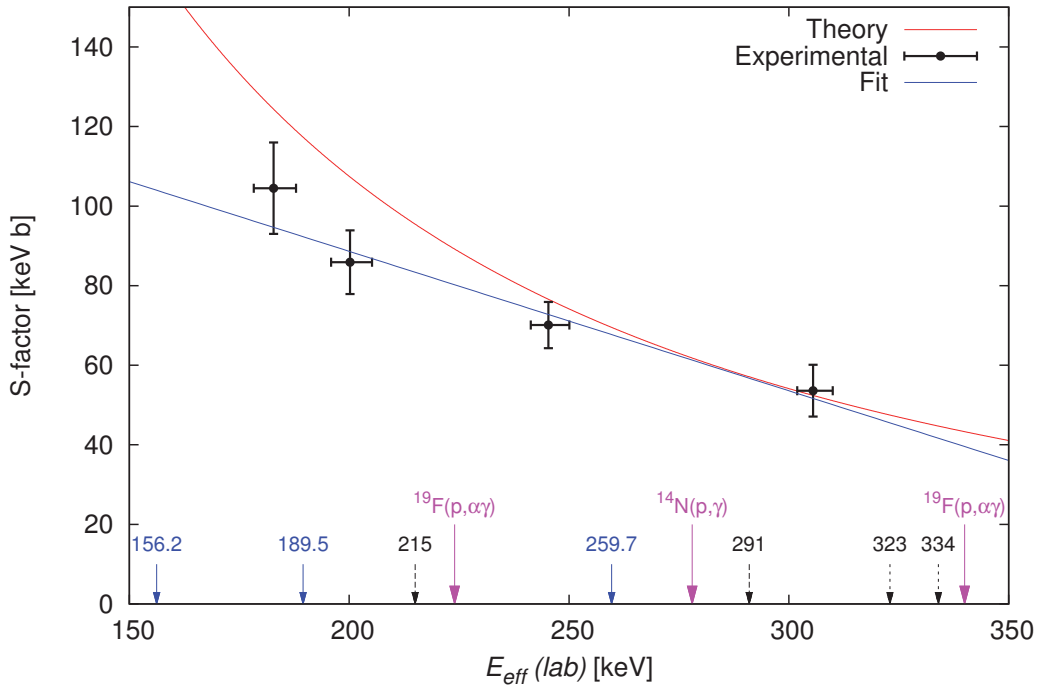

Figure 4.30: Non-resonant S-factors of the ^{22}Ne(p,γ)^{23}Na reaction from the present work. The blue line is a linear fit to the current experimental data, while the red curve corresponds to the theoretical prediction of the same color in Fig. 4.29. The arrows in blue represent the observed ^{22}Ne(p,γ)^{23}Na resonances, while the black ones are tentative ^{22}Ne resonances. Resonances of the ^{14}N(p,γ)^{15}N and ^{19}F(p,$\alpha\gamma$)^{16}O contaminant reactions are also shown.

4.4 Astrophysical reaction rate

In order to fully judge the astrophysical impact of the here derived new upper limits on the strength of the two tentative resonances at $E_p^{\mathrm{lab}} = 71$ and 105 keV, as well as the redetermined $\omega\gamma$ of the resonances at $E_p^{\mathrm{lab}} = 156.2$, 189.5 and 259.7 keV, and last but not least, the new information on the direct capture process, a recalculation of the thermonuclear reaction rate of ^{22}Ne(p,γ)^{23}Na was necessary. For the higher energy resonances not discussed here, the most recent $\omega\gamma$ values were adopted from the literature [30, 34, 35, 39, 41] with preference for direct measurements [34] whenever it was possible. A summary of the resonances included in the reaction rate calculation can be found in Table 4.15.

When studying nuclear fusion reactions, one should consider the fact that in the laboratory the target nuclei are surrounded by their atomic electron cloud. The negative charge of the electrons compensates to some degree the positive charge of the nucleus, which leads to a reduction of the Coulomb barrier experienced by the incident charged particle. This so called electron screening effect results in an enhancement of the reaction cross section over the fusion scenario of "bare" nuclei [61].

A similar effect occurs in astrophysical scenarios, because reactions in a stellar environment usually take place in plasma [62]. This results again in an enhancement of the reaction rate over the "bare" scenario. Thus, after correcting the experimental cross sections for the screening of atomic electrons, one has to apply a second (stellar) correction depending on the electron density of the plasma. The latter quantity is, however, strongly dependent on the astrophysical scenario used, and thus not a property of the nuclear reaction. Therefore, only the unscreened thermonuclear reaction rates are provided as input for stellar model calculations [21,39]. The stellar enhancement correction is then to be applied by the stellar modeler.

The atomic screening effect is characterised by the screening potential U_e. In the adiabatic limit [61], U_e is given by the difference between the total electron binding energy of neutral ^{22}Ne and onefold ionised ^{23}Na. Based on the tabulated electron binding energies for neutral atoms [63] and the first ionisation energy of ^{23}Na [64], the screening potenial is estimated to be

$$U_e = 0.903 \quad \mathrm{keV} \tag{4.26}$$

From Eq. 4.2 it is evident, that at astrophysical energies $\omega\gamma$ is directly proportional to the partial proton width Γ_p, which depends on the penetrability of the Coulomb barrier. This latter quantity, for a given energy E and angular momentum l, is characterised by the penetration factor $P_l(E)$. (For more detail see Appendix A).

The screening potential U_e can be interpreted as a small shift to the original collision energy E in the centre-of-mass frame, therefore the enhancement of the resonance strength can be expressed as follows:

$$f = \frac{\omega\gamma_{\mathrm{measured}}}{\omega\gamma_{\mathrm{bare}}} = \frac{P_l(E+U_e)}{E} \tag{4.27}$$

For low energies, where usually only the $l = 0$ case plays a role, f can be approximated as [62]

$$f = \left(\frac{E}{E+U_e}\right)^{1/2} \exp\Big[-2\pi\eta(E+U_e) + 2\pi\eta(E)\Big] \tag{4.28}$$

Table 4.15: Input for ^{22}Ne(p,γ)^{23}Na reaction rate calculation. In case of the resonances at $E_p^{\rm lab} = 71$ and 105 keV, a direct Monte Carlo sampling of the experimental data was used.

$E_{\rm res}^{\rm lab}$ [keV]			Adopted strength $\omega\gamma$ [keV b]	Ref.	Screening factor f
29	±	3	$\leq 2.6 \times 10^{-25}$	[41]	
37	±	0.7	$(3.1 \pm 1.2) \times 10^{-15}$	[41]	
71	±	5	$\leq 4.5 \times 10^{-11}$	present	1.270
105	±	5	$\leq 4.8 \times 10^{-11}$	present	1.142
156.2	±	0.7	$(1.84 \pm 0.09) \times 10^{-7}$	present	1.075
189.5	±	0.7	$(2.28 \pm 0.10) \times 10^{-6}$	present	1.056
215	±	10	$\leq 2.8 \times 10^{-8}$	[33]	1.046
259.7	±	0.5	$(8.74 \pm 0.39) \times 10^{-6}$	present	1.034
291	±	3	$\leq 2.2 \times 10^{-6}$	[35]	
323	±	3	$\leq 2.2 \times 10^{-6}$	[35]	
334	±	3	$\leq 3.0 \times 10^{-6}$	[35]	
369	±	5	$\leq 6.0 \times 10^{-4}$	[30]	
394	±	3	$\leq 6.0 \times 10^{-4}$	[30]	
436	±	0.8	0.0079 ± 0.006	[34]	1.015
479	±	1	0.594 ± 0.038	[34]	1.013
629.3	±	0.3	0.03 ± 0.01	[39]	
638.5	±	0.5	2.45 ± 0.18	[34]	1.008
660.1	±	0.5	0.032 ± 0.017	[34]	
724.8	±	0.8	0.15 ± 0.05	[39]	
850.7	±	0.2	8.2 ± 3.0	[39]	
896.3	±	1.0	2.1 ± 1.1	[39]	
900.2	±	1.0	1.22 ± 0.59	[39]	
919.5	±	1.0	0.93 ± 0.31	[39]	
928.6	±	0.4	0.41 ± 0.12	[39]	
947.5	±	1.0	7.0 ± 2.4	[39]	
980.5	±	0.13	0.47 ± 0.13	[39]	
1004.6	±	1.0	2.8 ± 0.9	[39]	
1067.4	±	0.4	1.0 ± 0.3	[39]	
1088.0	±	1.0	2.50 ± 0.69	[39]	
1103.2	±	0.5	2.50 ± 0.69	[39]	
1145.9	±	0.6	1.7 ± 0.5	[39]	
1173.2	±	0.6	0.7 ± 0.19	[39]	
1263.4	±	0.6	1.28 ± 0.37	[39]	
1277.4	±	0.4	12.2 ± 1.7	[39]	

One should note that the above equation is not applicable for indirect measurements, therefore in Table 4.15 the parameter f is only quoted for $\omega\gamma$ values which were obtained in direct experiments. In order to calculate the bare (unscreened) resonance strengths one has to divide the listed $\omega\gamma$ by f.

Then, the thermonuclear reaction rate of the ^{22}Ne(p,γ)^{23}Na was determined by a Monte Carlo based approach. The input parameters of the calculation were randomly sampled, where both the resonance energy and strength were assumed to have a Gaussian distribution except for the putative resonances at 71 and 105 keV.

In case of these two supposed resonances, the triple Poisson approach described in Sec. 4.2.1 was implemented, instead of directly using the upper limits on $\omega\gamma$. Thus, the distribution of the corresponding resonance strengths was determined based on the observed counting rates. As a second step, these histograms were randomly sampled to calculate the reaction rate.

In principle, it would have been more conservative to adopt the upper limits based on the Rolke approach [54] (see Tables 4.5 and 4.7). However, this would have made the random sampling of the input parameters problematic for the resonances at 71 and 105 keV, because the Rolke upper limit does not provide any information on the uncertainty of the $\omega\gamma$.

For each temperature the sampling was repeated 10000 times, and the total resonant reaction rate $N_A\langle\sigma v\rangle_R$ was calculated using the formula from [21]

$$N_A\langle\sigma v\rangle_{\rm R} = \frac{1.5399\times10^5}{(\mu T_9)^{3/2}}\sum_i \omega\gamma_i \exp\left[-11.605\frac{E_i^{\rm res}({\rm cm})}{T_9}\right] \qquad (4.29)$$

where T_9 is the temperature in GK, μ reduced mass in atomic mass units, $E_i^{\rm res}$(cm) the resonance energy in MeV of resonance i, and $\omega\gamma_i$ the corresponding resonance strength in eV, after correction for electron screening in the laboratory as described above.

Since in the previous chapter it was found that the direct capture contribution to the total cross section is negligible at low energies, the non-resonant part of the reaction rate $N_A\langle\sigma v\rangle_{\rm NR}$ was estimated based on the sub-threshold resonance at $E_{\rm R}^{\rm cm} = -130$ keV (blue curve in Fig. 4.29). It is important to note, that the contribution to the S-factor due to the tail of the resonance at $E_{\rm R}^{\rm cm} = 35$ keV ($E_p^{\rm lab} = 37$ keV) is not considered here, because it is included as a resonance in the reaction rate.

$N_A\langle\sigma v\rangle_{\rm NR}$ was then determined using the following numerical expression from [40]

$$N_A\langle\sigma v\rangle_{\rm NR} = 17.083\times10^9 S(E_0)T_9^{-2/3}\exp\left[-19.478T_9^{-1/3}\right] \qquad (4.30)$$

where the integration over the Gamow peak is already done. Therefore, the S-factor has to be evaluated for each temperature T_9 at the corresponding E_0 Gamow-energy (see Eq. 1.15). As a conservative estimate $\pm40\%$ uncertainty was assigned to the S-factor, following the approach of [30, 38, 39].

The resulting total reaction rate $N_A\langle\sigma v\rangle = N_A\langle\sigma v\rangle_{\rm R} + N_A\langle\sigma v\rangle_{\rm NR}$ is shown in Fig. 4.31. For each temperature, low, median and high rate values were determined based on the 0.16, 0.50 and 0.84 quantiles of the probability density function for the total rate. Following the approach used in the determination of the LUNA-HPGe reaction rate [38], the low rate for the tentative resonances at $E_p^{\rm lab} = 71$, 105 and 215 keV was set to zero with uncertainty zero. This assumption is also consistent with the STARLIB-2013 compilation [39].

In Fig. 4.32, the obtained reaction rate is shown normalised to the recommended rate from STARLIB-2013 [39]. The individual contributions to the total reaction rate are also shown separately: At the lowest temperatures, the rate and its uncertainty are determined by the resonance at $E_p^{\mathrm{lab}} = 37$ keV. The considerable increase in the rate uncertainty for the temperatures $0.04 \leq T_9 \leq 0.1$ is due to the 71 keV resonance, while the contribution of the 105 keV resonance is nearly negligible. The non-resonant rate due to the presence of the sub-threshold resonance $E_{\mathrm{res}}^{\mathrm{cm}} = -130$ keV also peaks around 0.8 GK, followed by a decreasing trend towards higher temperatures.

The following temperature region $0.1 \leq T_9 \leq 0.2$ is determined by the resonances at 156.2 and 189.5 keV. Interestingly, the 259.7 keV resonance, which is the strongest among the here measured resonance, has only a moderate contribution. At even higher temperatures, resonances at 436, 479 and 638.5 keV play the major role.

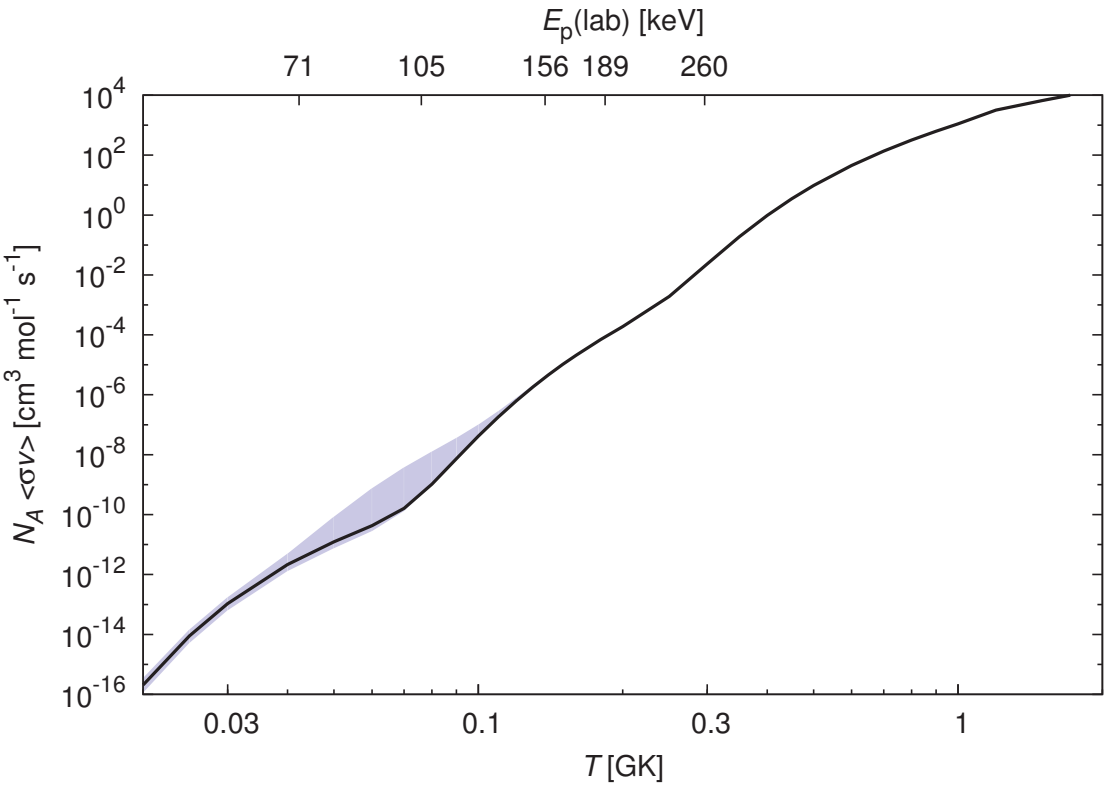

Figure 4.31: $^{22}\mathrm{Ne}(p,\gamma)^{23}\mathrm{Na}$ thermonuclear reaction rate calculated with the resonance strengths listed in Table 4.15

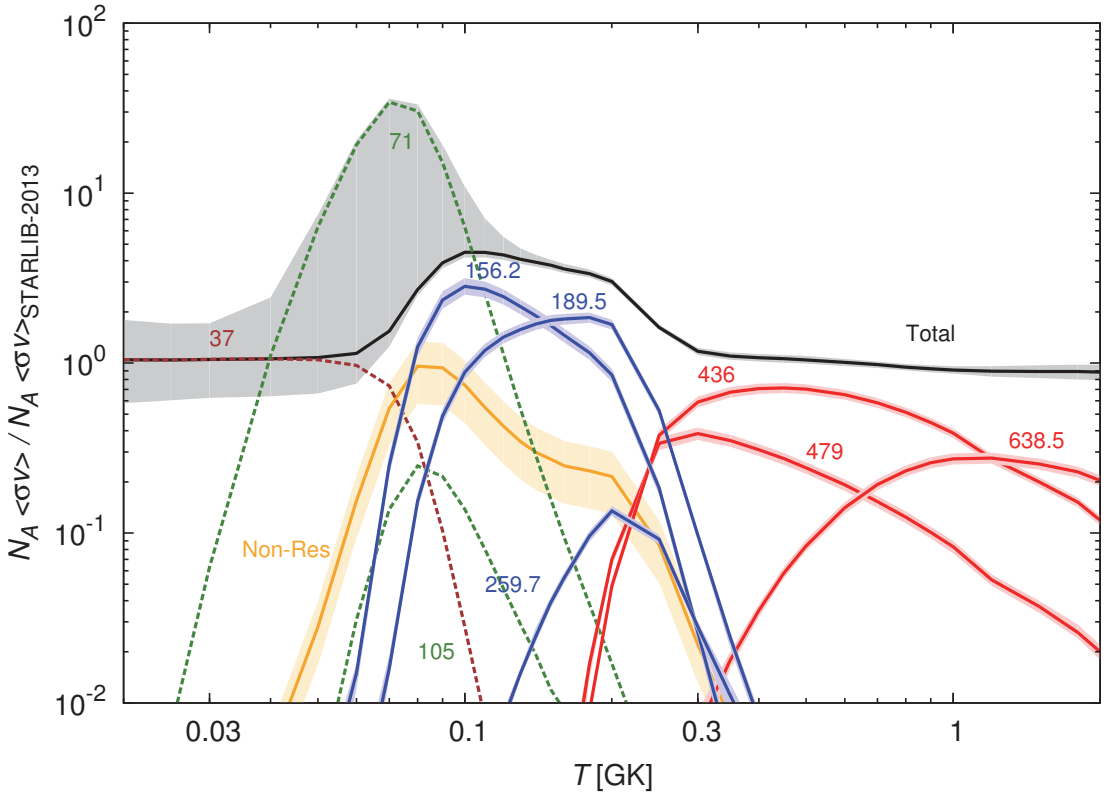

Figure 4.32: ^{22}Ne$(p,\gamma)^{23}$Na reaction rate from the LUNA-BGO phase, normalised to the STARLIB-2013 rate [39]. The total reaction rate is shown in black, with 1σ uncertainty indicated by the grey shaded area. The individual contributions form the most important resonances, and the non-resonant process (sub-threshold resonance, $E_{\rm res}^{\rm cm} = -130$ keV) are shown in color. In case of the 71 and 105 keV resonances, the dashed line corresponds to the high rate value determined from the upper limits.

4.5 Error analysis

In this section the various uncertainties propagating into the final resonance strength (Eq. 4.2) and S-factor values (Eq. 4.17) are discussed. Statistical and systematic sources of uncertainty are considered separately during the analysis, and a summary is given in Table 4.16 and 4.17.

4.5.1 Statistical uncertainties

As it is evident from Eq. 4.2 and 4.17, the yield is the directly measured quantity in case of the resonant and non-resonant capture reactions. Therefore, the statistical uncertainties are concentrated in the yield.

1. **Peak area**

   The uncertainty on the integrated number of events in the experimental ROI was estimated based on Poisson statistics. In case of the beam induced background, the uncertainty of the normalisation to spectra taken in ^{22}Ne was also included in the error budget. This later quantity was estimated based on the integrated number of counts in ROI 11-18 MeV in the spectra. (In the special case of the 71 and 105 keV resonances, only upper limits were derived on the counting rate, therefore this uncertainty is not applicable, see Sec. 4.2.1).

2. **Charge / Beam current**

   Due to the calorimetric measurement method adopted, the beam current is determined according to Eq. 3.3. Its uncertainty depends on the following three underlying quantities:

   - The deposited beam power $W_{beam} = W_0 - W_I$ was assigned a 0.2 Watt uncertainty, conservatively reflecting twice the statistical fluctuations affecting the measurements of W_0 and W_I.
   - The precision of the beam energy at the calorimeter $E_{\rm cal} = E_p^{\rm ini} - \Delta E$ is mainly limited by the uncertainty on the energy loss ΔE in the target gas, since the energy spread of the initial beam energy $E_p^{\rm ini}$ amounts less than 0.1 keV. The calculation of the energy loss with respect to the current measurement was based on Eq. 3.2.3. The reference target density and the effective target length were considered with 1.4% and 3.4% uncertainties respectively. Last but not least, the stopping power values from SRIM [56] have 1.7% uncertainty. Considering all theses components in quadrature, the beam energy loss ΔE was known at 4% level of precision. The total relative uncertainty of $E_{\rm cal}$ was about 1% depending on the beam energy.
   - Uncertainty due to the calorimeter calibration is considered systematic, see below.

   The statistical uncertainty of the charge / beam current was less than 2%, with exception of the resonance at 71 keV.

4.5.2 Systematic uncertainties

In case of the systematic uncertainties, one should differentiate between the $\omega\gamma$ and S-factor measurement, however, the first two sources of uncertainty were common for both cases:

1. **Calorimeter calibration**

   Due to the calibration of the calorimeter (see Eq. 3.2.2), there was an additional 1% systematic uncertainty in the integrated charge.

2. **Add-back efficiency**

   The uncertainty of the detector efficiency originates from two sources: The modelling of the BGO detector, and the branching ratios which are adopted for the determination of the add-back efficiency.

   - The simulation was able to reproduce the efficiency measurement with point-like sources (see Fig. 3.16). The overall agreement was on the level of 4%.
   - The uncertainty of the simulated add-back detection efficiency due to the decay scheme of the level under study was estimated based on different sets of branching ratios (see Tables 4.4, 4.8, 4.9, 4.10, and 4.12). This contribution was mainly important for the putative resonances at 71 and 105 eV, and direct capture process, amounting to 21%, 22%, and 5.7% respectively. For resonances at 156.2, 189.5 and 259.7 keV, the uncertainty in detection efficiency due to the branching ratios was less than 1.5%.

3. **Stopping power**

   The stopping powers were adopted from the SRIM compilation [56], thus their 1.7% uncertainty was considered as systematic uncertainty in the calculation of $\omega\gamma$.

4. **Resonance energy**

   The uncertainty of the resonance energy also affects the final value of $\omega\gamma$ via the de Broglie-wave length λ_r in Eq. 4.2. In case of the known resonances at 156.2, 189.5, and 259.7 keV, the resonance energies and their uncertainties were adopted from LUNA-HPGe phase [38, 50].

5. **Beam energy**

   The initial beam energy represents the upper limit of the non-resonant yield integration (Eq. 4.17). The systematic uncertainty of the beam energy was 0.3 keV, while the statistical uncertainty due to the beam spread was about 0.1 keV [46], adding up to a total 0.3 keV uncertainty. The non-resonant yield was thus also evaluated for the nominal beam energy $\pm$0.3 keV, and the half of the difference between the two values was taken as beam energy dependent uncertainty in the final S-factor.

6. **Density profile**

   The adopted density profile along the path of the beam plays an important role, because in case of non-resonant capture, the reaction can occur not only inside the target chamber, but also in the collimator and in the interconnection tube. The sensitivity of the S-factor on the density profile was tested by successively adopting three different density profiles. Moreover, one has to take into account variations in the room temperature, which result in a shift of the overall density profile. The overall uncertainty was estimated to be 3.4%.

7. **Beam heating correction**

   The beam heating effect plays an important role in the proper determination of the non-resonant yield. The uncertainty associated with the necessary beam heating correction (Eq. 3.2.4) amounted to $1.1 - 1.3\%$

Table 4.16: Overview of the statistical and systematic uncertainties for the resonance strengths

	Statistical		Systematic				
E_{res}(lab) [keV]	Peak area	Charge	Calo. calib.	Efficiency	Stopping power	Res. energy	Total
71	-	4.0%	1.0%	21.0%	1.7%	7.0%	22.9%
105	-	1.4%	1.0%	22.0%	1.7%	4.8%	22.8%
156.2	1.9%	1.0%	1.0%	4.2%	1.7%	0.4%	5.1%
189.5	0.3%	0.9%	1.0%	4.0%	1.7%	0.4%	4.6%
259.7	0.1%	0.4%	1.0%	4.0%	1.7%	0.2%	4.5%

Table 4.17: Overview of the statistical and systematic uncertainties for the derived S-factors

	Statistical			Systematic				
E_{eff}(lab) [keV]	Peak area	Charge	Calo. calib.	Efficiency	Beam energy	Density profile	Beam heating	Total
182.8	7.2%	0.7%	1.0%	7.0%	1.7%	3.4%	1.1%	10.9%
200.1	4.3%	1.0%	1.0%	7.0%	1.5%	3.4%	1.3%	9.3%
245.2	1.1%	0.5%	1.0%	7.0%	1.1%	3.4%	1.2%	8.1%
305.6	9.0%	0.4%	1.0%	7.0%	0.8%	3.4%	1.1%	12.0%

Chapter 5

Study of the *pp*-chain with the help of solar neutrinos

The Sun serves as the primary source of general information on all stars. Without a correct description of our own Sun, we cannot hope to achieve a general understanding of the stellar nucleosynthesis and energy generation.

Being a G-type main sequence star with effective surface temperature of approximately 6000 K, the Sun sustains itself against gravitational collapse by converting hydrogen into helium in its core. As it was already mentioned in the Chapter 1, there are two different modes of hydrogen burning: the *pp*-chain and the CNO-cycle (see Fig. 1.3 and 1.4). In case of our Sun, the presence of heavier elements in the solar interior makes in principle both processes possible. However, due to the moderate core temperature of $T_c = 16 \times 10^6$ K (or $T_9 = 0.016$ as it will be denoted here) the CNO-cycle is highly inefficient in the Sun. Therefore, approximately 99% of hydrogen fusion takes place via the *pp*-chain.

On the other hand, the astrophysical relevance of the *pp*-chain extends beyond the scope of stellar nucleosynthesis: some of the same reactions which allow a relatively slow conversion of hydrogen into helium in stars were also active during the Big Bang, setting the primordial abundances of the light elements.

Despite their paramount importance, a direct experimental study of these reactions is not feasible at energies relevant to the Sun. Thus, one has to extrapolate the trend of the astrophysical S-factor to the solar Gamow peak based on the data obtained at higher energies. Unfortunately, such extrapolations are not without ambiguities, often leading to considerable uncertainties in the resulting thermonuclear reaction rate.

Fortunately, neutrino astronomy opened up new possibilities to gather information on the solar interior. Both *pp*-chain and CNO-cycle give rise to several branches of solar neutrinos (see Fig. 5.1), providing a way to probe our understanding of the Sun, and the underlying nuclear processes. Based on this idea, in late 1960s Davis built an ambitious experiment in the Homestake Gold Mine (South Dakota, USA). The detection of solar neutrinos was based on their capture process on the ^{37}Cl isotope:

$$\nu_e \quad + \quad {}^{37}\mathrm{Cl} \quad \rightarrow \quad {}^{37}\mathrm{Ar} \quad + \quad e^- \tag{5.1}$$

At first it seemed, that something is completely wrong, because the theoretical description of our Sun developed by Bahcall, known as the standard solar model [65]

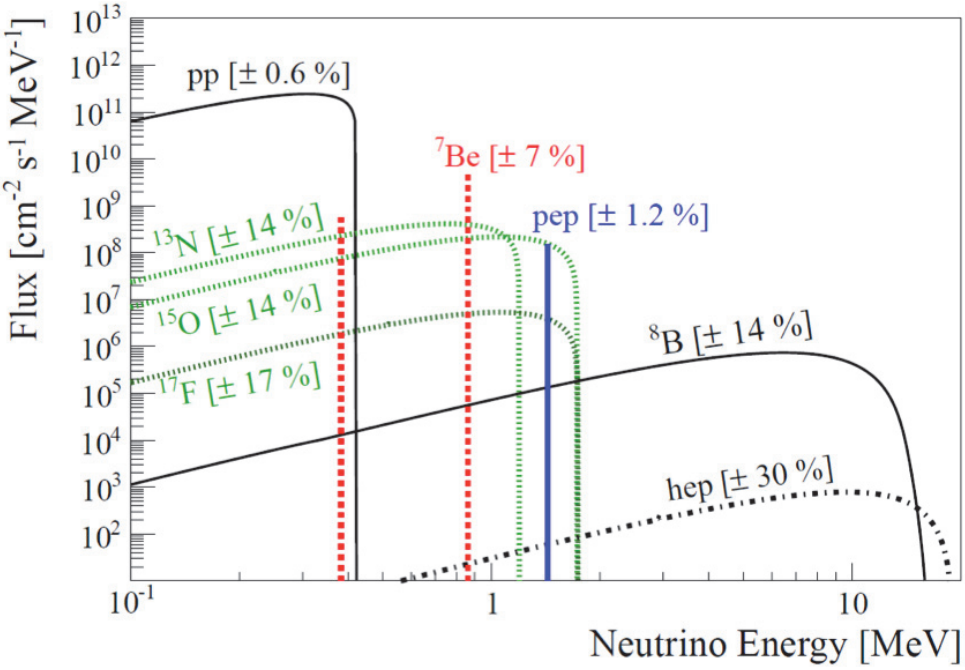

Figure 5.1: Energy spectrum of solar neutrinos from the SSM - adopted from arXiv:1405.7919

predicted approximately three times higher flux for the neutrinos [66] than it was actually observed by Davis [67] in the experiment. This puzzling finding became known as the solar neutrino problem. The solution for the missing neutrinos was provided by the discovery of neutrino flavour oscillations.

Since the 1960s, a number of new neutrino experiments has been built around the globe, and great precision has been reached in the detection of neutrinos originating from the decay of ^{7}Be and ^{8}B isotopes produced in the *pp*-chain. The Sudbury Neutrino Observatory (SNO) reports a ^{8}B solar neutrino flux of

$$\phi_{\mathrm{B}}^{\mathrm{exp}} = 5.25 \pm 0.16\ (\mathrm{stat})^{+0.11}_{-0.13}\ (\mathrm{sys}) \times 10^{6}\mathrm{cm}^{-2}\mathrm{s}^{-1} \tag{5.2}$$

taking into account the loss in the amount of electron neutrinos due to the mixing among the neutrino families [68]. This is equivalent to 3.9% precision (systematic and statistical uncertainties combined in quadrature) and consistent with the determination made by Super-Kamiokande [69].

The flux of ^{7}Be neutrinos was measured by BOREXINO [70], resulting in a value of

$$\phi_{\mathrm{Be}}^{\mathrm{exp}} = 4.75^{+0.26}_{-0.22} \times 10^{9}\mathrm{cm}^{-2}\mathrm{s}^{-1} \tag{5.3}$$

with 5.5% total uncertainty.

With this level of precision, the experimental fluxes of ^{7}Be and ^{8}B neutrinos can be used to directly constrain the S-factor of the underlying ^{3}He(α,γ)^{7}Be and ^{7}Be(p,γ)^{8}B reactions.

5.1 S-factor of the ^{3}He(α,γ)^{7}Be reaction

A number of recent determinations are available considering the S-factor of the ^{3}He(α,γ)^{7}Be reaction (denoted as $S_{34}(E)$ hereafter) at $E > 0.3\,\mathrm{MeV}$ [71–76]. How-

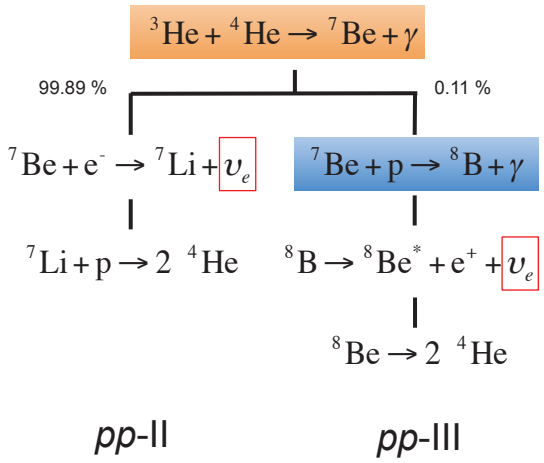

Figure 5.2: The ^{3}He(α,γ)^{7}Be reaction and resulting two branches of solar neutrinos

ever, as it is evident from Fig. 5.3, this abundance of recent experimental data covers only the upper third of the relevant energy range. At lower energy, the exceedingly low cross section is a challenge for experimentalists. As a consequence, recent data for $E \leq 0.3\,\mathrm{MeV}$ are available only from one experiment [77], performed by the LUNA collaboration.

It should be noted that $S_{34}(E)$ data reported in the period from the 1950s to the 1980s [78–84] are omitted from the present discussion, following the approach of a recent review [85]. These data [78–84] are usually less well documented than the more recent works [71–77] and have larger error bars.

The pressing need for low-energy data on $S_{34}(E)$ is addressed here based on the fact that actually the solar Gamow peak is rather narrow (see Fig. 5.3). This allows the determination of $S_{34}(E^{\mathrm{Sun}}_{\mathrm{Gamow}})$ from $N_{\mathrm{A}}\langle\sigma v\rangle_{34}(T^{\mathrm{Sun}})$ considering the latest solar neutrino data. The new data point then can be used to constrain the trend of the S-factor at energies corresponding to the BBN, thus place a better estimate on the primordial ^{7}Li production. A related idea has previously been explored by Cyburt et al. a decade ago [87]. That work was based on the neutrino data available at the time from the Sudbury Neutrino Observatory (SNO), and on the WMAP cosmological survey.

5.1.1 Determination of S_{34} at the solar core temperature

The approach presented here has the advantage that it does not require detailed solar model calculations. Instead, the already mentioned standard solar model developed by John Bahcall and co-workers is used, hereafter called SSM. The SSM uses a number of input parameters, including the solar age, luminosity, opacity, diffusion rate, the key thermonuclear reaction rates (herein called R_i, where i denotes the nuclear reaction under study), and the zero-age abundance of important elements (He, C, N, O, Ne, Mg, Si, S, Ar, Fe).

A change in one or several of these input parameters may cause a change in the predicted neutrino fluxes. The sensitivity of flux ϕ_i for a variation in an arbitrary parameter β_j can be expressed by the logarithmic partial derivatives $\alpha(i,j)$ given

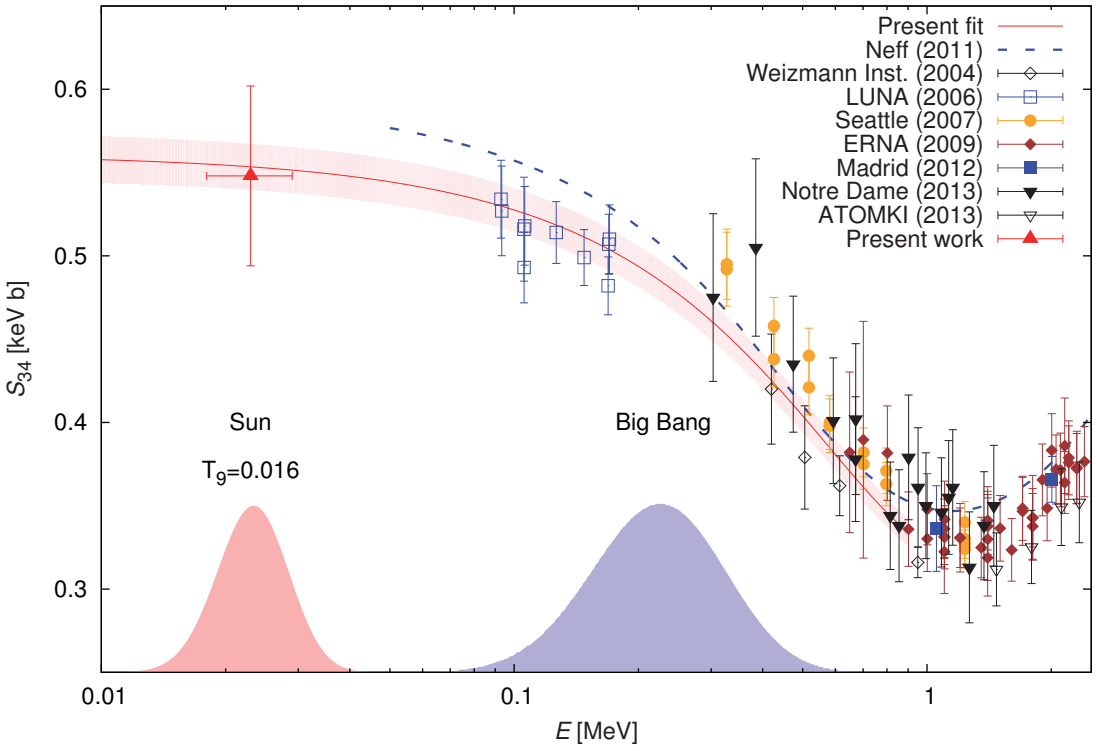

Figure 5.3: Experimental cross section of the ^{3}He(α,γ)^{7}Be reaction, parameterized as the astrophysical S-factor. The present new data point (red triangle) is plotted together with previous experimental data [71–77]. The previous theoretical curve (dashed blue curve, [86]), and the present new extrapolation (red curve, shaded area for the uncertainty) are shown. The solar Gamow peak and the relevant energy range for BBN are displayed at the lower end of the plot.

by the following relation:

$$\alpha(i,j) = \frac{\partial ln[\phi_i/\phi_i^{\mathrm{SSM}}]}{\partial ln[\beta_j/\beta_j^{\mathrm{SSM}}]} \tag{5.4}$$

where ϕ_i^{SSM} and β_j^{SSM} represent the best theoretical values from the SSM. The partial derivatives for the various SSM input parameters are available in tabulated form in the most recent SSM publication by Serenelli *et al.* [88] (see Table 5.1).

With help of these logarithmic partial derivatives one can approximate relatively small changes in the neutrino flux as a simple power law:

$$\frac{\phi_i}{\phi_i^{\mathrm{SSM}}} = \prod_j^N \Big(\frac{\beta_j}{\beta_j^{\mathrm{SSM}}}\Big)^{\alpha(i,j)} \tag{5.5}$$

The parameter of interest in the present work is the thermonuclear reaction rate of the ^{3}He$(\alpha,\gamma)^7$Be reaction, here denoted as R_{34}. Its strong effect on the ^{7}Be and ^{8}B neutrino fluxes is clearly reflected in partial derivatives that are close to unity: $\alpha(Be, S_{34}) \approx \alpha(B, S_{34}) \approx 0.8$.

Now, by fixing all parameters except for R_{34} at their SSM best-fit value, Eq. (5.5) is shortened to:

$$\frac{\phi_{\mathrm{Be}}^{\mathrm{exp}}}{\phi_{\mathrm{Be}}^{\mathrm{SSM}}} = \left(\frac{R_{34}^{\nu,\mathrm{Be}}}{R_{34}^{\mathrm{SSM}}}\right)^{\alpha(\mathrm{Be},S_{34}^{\mathrm{SSM}})} \tag{5.6}$$

when using the experimental flux of ^{7}Be neutrinos $\phi_{\mathrm{Be}}^{\mathrm{exp}}$. An analogous relation can be obtained based on the ^{8}B neutrino flux $\phi_{\mathrm{B}}^{\mathrm{exp}}$.

Solving for the thermonuclear reaction rate $R_{34}^{\nu,\mathrm{Be/B}}$, the following two relations are obtained:

$$R_{34}^{\nu,\mathrm{Be}} = \Big(\frac{\phi_{\mathrm{Be}}^{\mathrm{exp}}}{\phi_{\mathrm{Be}}^{\mathrm{SSM}}}\Big)^{\alpha^{-1}(\mathrm{Be},S_{34})} R_{34}^{\mathrm{SSM}} \tag{5.7}$$

$$R_{34}^{\nu,\mathrm{B}} = \Big(\frac{\phi_{\mathrm{B}}^{\mathrm{exp}}}{\phi_{\mathrm{B}}^{\mathrm{SSM}}}\Big)^{\alpha^{-1}(\mathrm{B},S_{34})} R_{34}^{\mathrm{SSM}} \tag{5.8}$$

It is important to note, that the nuclear reaction rate R_{34} used for Equations (5.6-5.8) applies to a certain range of temperatures. The emission of ^{7}Be neutrinos is known to originate from a narrow burning zone at the center of the Sun, at radii below $0.15R_\odot$ (where $R_\odot$ is the solar radius), with a temperature $T_9 = 0.011$-0.016, close to the nominal central temperature. The ^{8}B neutrino emission originates from an even narrower burning zone, below $0.10R_\odot$.

Therefore, it can be assumed that to good approximation the relevant temperature for the ^{3}He$(\alpha,\gamma)^7$Be reaction is the central temperature of the Sun, $T_9 = 0.016$. Thus, equations (5.6-5.8) apply to the nuclear reaction rate in the energy range of the solar Gamow peak (Fig. 5.3). The value of the reaction rate at energies that lie outside the Gamow peak does not affect solar fusion.

Table 5.1 lists the most important logarithmic partial derivatives $\alpha(\mathrm{Be/B}, j)$ discussed here. In addition, the table also includes the contribution of each parameter to the SSM error budget. Values and errors are taken from the recent SSM paper by Serenelli *et al.* [88]. Two parameters merit a more detailed discussion:

First is the elemental composition of the Sun. It has undergone a significant revision from the GS98 [89] to the AGSS09 [90] abundance compilations. The

Table 5.1: Logarithmic partial derivatives $\alpha(\mathrm{Be}, j)$ and $\alpha(\mathrm{B}, j)$, as defined by Eq. (5.4) and their contributions to the total uncertainty of the predicted SSM flux. Values and uncertainties are taken from [88], except for the solar composition (see text).

Parameter	$\alpha(\phi_{\mathrm{Be}}, j)$	$\frac{\Delta\phi_{\mathrm{Be}}}{\phi_{\mathrm{Be}}}(\%)$	$\alpha(\phi_{\mathrm{B}}, j)$	$\frac{\Delta\phi_{\mathrm{B}}}{\phi_{\mathrm{B}}}(\%)$
Luminosity	3.434	1.4	6.914	2.8
Opacity	1.210	3.0	2.611	6.5
Age	0.760	0.3	1.345	0.6
Diffusion	0.126	1.9	0.267	4.0
R_{11} - p+p	-1.024	1.0	-2.651	2.6
R_{33} - ^{3}He +^{3}He	-0.428	2.2	-0.405	2.1
R_{34} - ^{3}He +^{4}He	0.853	(4.6)	0.806	(4.3)
R_{17} - p +^{7}Be	-	-	1.000	7.7
R_{e7} - e +^{7}Be	-	-	-1.000	2.0
Composition*	-	4.6	-	9.7
Total uncertainty		6.5		15.3

determination of the abundance of a given element requires the modelling of the related absorption lines in the solar spectrum thus modelling the solar atmosphere. In the time interval from 1998 to 2005/2009, the modelling of the solar atmosphere was updated from a one-dimensional, time-independent, hydrostatic [89] to a three-dimensional, time-dependent hydrodynamical model [90].

The adoption of three-dimensional modeling in AGSS09, however, led to a significant downward revision of the abundances of the so-called "metals" - the name given in solar physics to all elements that are heavier than helium. The mass fraction Z for "metals" in the Sun changed from 0.0169 [89] to 0.0134 [90]. The carbon and nitrogen abundances decreased by 19%, and the oxygen abundance even by 28% from GS98 to AGSS09.

These significant revisions in the abundances of important elements lead to a contradiction between SSM predictions and helioseismological observations [91], when the new abundances are incorporated in the SSM. For the present purposes, the problem of the elemental abundances must be set aside. This is accomplished by adopting the average of the two different SSM predictions (the first one based on GS98, the second one based on AGSS09) as value, and half the difference as uncertainty (Table 5.2). In this manner, within their 1σ error bars the present conclusions apply to both the GS98 and AGSS09 elemental abundances.

Second is the astrophysical reaction rate of the ^{3}He(α,γ)^{7}Be reaction, R_{34}. The value of R_{34} taken in the SSM calculations followed here [88] is the recommended curve by the "Solar Fusion cross sections II" review [85]. However, in order to avoid double counting, the uncertainty of R_{34} is left out when computing the total uncertainty (Table 5.1). Instead, this parameter and its uncertainty are re-determined here based on all the other parameters.

With these two modifications, the total uncertainty of the flux prediction is 6.5%

Table 5.2: Predicted solar neutrino fluxes from the SSM for two different elemental abundances, taken from [88]. The average adopted here includes both results with its error bar.

Elemental comp.	$\phi(^7\mathrm{Be})$	$\phi(^8\mathrm{B})$	Ref.
GS98 [89]	5.00	5.58	[92]
AGSS09 [90]	4.56	4.59	[92]
Average	4.78 ± 0.22	5.09 ± 0.49	Adopted here

for $\phi_{\mathrm{Be}}^{\mathrm{SSM}}$ and 15.3% for $\phi_{\mathrm{B}}^{\mathrm{SSM}}$. If one were to select just one of the two solar elemental compositions, the total error would decrease to 4.5% and 11.9%, respectively.

The thermonuclear reaction rate R_{34} is directly proportional to the astrophysical S-factor S_{34} (Eq. 1.14) in the relevant energy range. Therefore, one can express the same equation (see Eq. 5.7 and 5.8) also with S_{34}. As the best SSM recommendation for the S-factor, the "Solar Fusion II" parametrization was accepted [85]. The new $S_{34}(E_{\mathrm{gamow}})$ is found to be

$$S_{34}^{^7\mathrm{Be}}(23^{+6}_{-5}\,\mathrm{keV}) = 0.548 \pm 0.054\ \mathrm{keV\ b} \quad (5.9)$$

$$S_{34}^{^8\mathrm{B}}(23^{+6}_{-5}\,\mathrm{keV}) = 0.58 \pm 0.11\ \mathrm{keV\ b} \quad (5.10)$$

The two data points are in good agreement with each other. Most of the contributions to the error budget that are common to both data points are from factors such as the elemental abundances that affect both the ^{7}Be and ^{8}B fluxes in the same direction, and at the same time affect the ^{8}B-based result more strongly than the ^{7}Be-based one. Therefore, an averaging of the two numbers actually leads to a higher total uncertainty than the error bar of the ^{7}Be-based value. Therefore, $S_{34}^{^7\mathrm{Be}}(23^{+6}_{-5}\,\mathrm{keV})$ is adopted as the final result here.

5.1.2 Implications for the BBN reaction rate and production of ^{7}Li

As can bee seen in Fig. 5.3, the $S_{34}^{^7\mathrm{Be}}(23^{+6}_{-5}\,\mathrm{keV})$ value confirms that the shape of the "Solar Fusion II" recommended S-factor curve is correct at low energy . However, the present new data point cannot be directly compared to the theory curve by Neff, which does not extend to such low energies for numerical reasons [86].

As a next step, the combined analysis of all experimental data points is carried out, repeating the approach of "Solar Fusion II" but adding the present new neutrino-based data point and the new data set from the University of Notre Dame that became available in the meantime [76]. The same analytical function as in "Solar Fusion II" is again used here, namely

$$S_{34}(E) = S_{34}(0)\exp(-0.580E)(1 - 0.4054E^2 + 0.577E^3 - 0.1353E^4) \quad (5.11)$$

This curve is based on the microscopic model by Nollett (Kim A potential) [95] and was already used for fitting the experimental data [85]. For the analysis, each

Table 5.3: Determination of $S_{34}(0)$ from recent experimental data, using Eq. (5.11) as fit function. See text for details.

Reference	$S_{34}(0)$ [keV b]	Inflation factor
Weizmann [71]	0.538±0.015	1.00
LUNA [77, 93, 94]	0.550±0.017	1.06
Seattle [72]	0.598±0.019	1.15
ERNA [73]	0.582±0.029	1.03
Notre Dame [76]	0.593±0.048	1.00
Present work	0.556±0.055	1.00
Combined result	0.561±0.011	1.32

experimental data set [71–73, 76, 77, present] was fitted with this analytical function (5.11) in the energy range $0 \leq E \leq 1.002$ MeV, and a value of $S_{34}(0)$ is then found for this particular data set.

The data from Madrid and from ATOMKI [74, 75] are excluded, because for those two cases all of the data points fall outside the energy range of applicability of Eq. (5.11). However, these data [74, 75] are in good agreement with other data sets which include data points both in the Madrid/ATOMKI energy range and in the range of applicability of the fit [73, 76]. Therefore, no bias is introduced by the necessary omission of Refs. [74, 75]. For each fitted data set, an inflation factor is determined from the goodness of the fit to the data, again following ref. [85].

The resulting $S_{34}(0)$ values for each data set are then again fitted together in order to obtain one combined value. As it can be seen, all the previous experimental data [71–73, 76, 77] lie near the recommended new curve (Fig. 5.3) with

$$S_{34}(0) = 0.561 \pm 0.014_{\text{stat}} \text{ keV b} \tag{5.12}$$

where the uncertainty was obtained by multiplying the raw uncertainty resulting from the fit with the inflation factor. This can be compared with the "Solar Fusion II" result of $S(0) = (0.56 \pm 0.02_{\text{stat}} \pm 0.02_{\text{syst}})$ keV b [85].

In "Solar Fusion II", the systematic uncertainty results from the extrapolation from the energies where many different experiments are available to the solar Gamow peak. For the purposes of BBN, instead of an extrapolation only an interpolation is needed (Fig. 5.3). Therefore, this latter error bar can be omitted here.

This result is lower than $S_{34}(0) = 0.580 \pm 0.043$ keV b, the previously evaluated value by [96] that has been used in several BBN calculations [97–99]. When converting to the peak of the BBN sensitivity range, from the present work a value of $S_{34}(226\,\text{keV}) = 0.485 \pm 0.012$ keV b is found, very close to the previous 0.487 ± 0.036 keV b [96] but more precise.

The increase in precision is due to three factors. First, the adoption of the "Solar Fusion II" approach that gives prominence to the fact that $S_{34}(E)$ has been measured in a number of independent precision experiments, with mutually consistent results. Second, the addition of new data points, including the present one, since 2008. Third, the theory error used in "Solar Fusion II" is not applicable here, as no

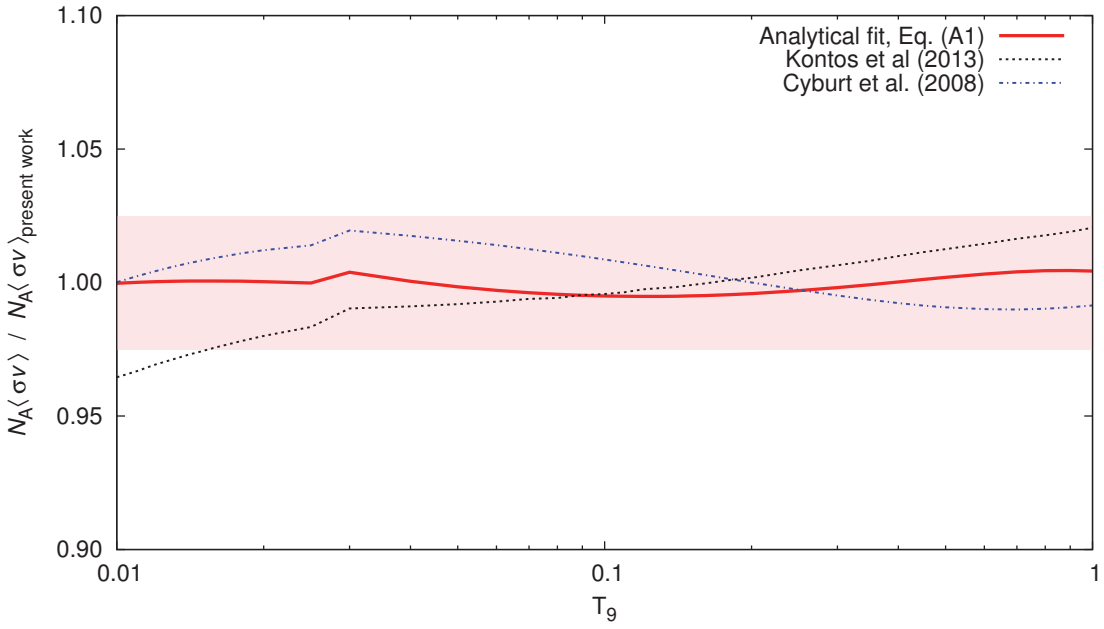

Figure 5.4: Thermonuclear reaction rate of the ^{3}He$(\alpha,\gamma)^7$Be reaction, relative to the present rate, by Kontos *et al.* (black dashed curve, [76]) and by Cyburt *et al.* (blue dot-dashed curve, [96]). The analytical fit function from Eq. (C.1) is also shown (red full curve).

extrapolation is needed.

The S-factor curve resulting from the combined fit described in the previous section (Fig. 5.3) has subsequently been used to compute the thermonuclear reaction rate R_{34} for its range of applicability, i.e. for $0.001 \leq T_9 \leq 1.0$, which includes the relevant temperature range for BBN (see Fig. 5.4). The range is estimated here by measuring the effect of a small change in the assumed S-factor at one given energy on the final ^{7}Li abundance at the end of BBN, following the approach of Nollett and Burles [100]. The relevant energy range is found to be E = 0.1-0.5 MeV (Fig. 5.3), which is consistent with the previous result [100]. Subsequently, also the relevant temperature range for ^{7}Be production in BBN is determined by arbitrarily setting R_{34} to zero above a certain temperature, resulting in T_9=0.30-0.65, if a relevant effect is defined as a 2.5% contribution on the ^{7}Be yield. When converting these temperatures to Gamow energies, the resultant relevant energy range is consistent with the one based on the Nollett and Burles [100] approach, adopted here.

For higher temperatures $T_9 > 1.0$, the conclusions depend on the slope of the excitation function above 1 MeV. Different theoretical papers give different slopes for $E > 1$ MeV [86, 95, 101, 102]. However, this temperature range is irrelevant for BBN, and thus excluded from consideration here. The tabulated reaction rate and an analytical fitting function can be found in the Appendix C.

The new rate was then used as input in the PArthENoPE BBN code [103]. Among publicly available codes [103, 104], PArthENoPE incorporates the most recent reaction rate data. Besides the rate of the ^{3}He$(\alpha,\gamma)^7$Be reaction, the baryonic density ($\Omega_b h^2$), and the lifetime of the neutron (τ_n) are also important parameters. Therefore, the PArthENoPE code was updated based on the most recent measure-

ments by the Planck mission [105]

$$\Omega_b h^2 = 0.02205 \pm 0.00028 \tag{5.13}$$

and the latest recommendation from the Particle Data Group [106]

$$\tau_{\rm n} = 880.3 \pm 1.1 \text{ s} \tag{5.14}$$

It is worth to note, that the lifetime of the neutron varied considerably (878-885 s) in the last years. Fortunately, the primordial ^{7}Li abundance is far more sensitive for changes in the other two parameters.

With these parameters the resulting BBN lithium abundance was found to be

$$^7\text{Li/H} = 5.0 \times 10^{-10} \tag{5.15}$$

By repeating the BBN calculation with the upper and lower limits given by the error on R_{34}, it is found that the present 2.5% error for R_{34} contributes just 2.4% uncertainty to the error budget of ^{7}Li/H. This value is to be compared with a previous contribution of 5.3% that can be estimated by using the previous R_{34} error [96] and the previous correlation coefficient [99]. The total uncertainty of ^{7}Li/H has previously been estimated to be 8% [99]. When subtracting the previous R_{34} contribution in quadrature and adding the present, new R_{34} contribution, a new total relative uncertainty of 6% can be estimated for ^{7}Li/H, leading to a final value of $^7\text{Li/H} = (5.0 \pm 0.3) \times 10^{-10}$. However, this estimated total uncertainty still needs to be borne out in a full BBN calculation re-analysing in detail also the error budget contributions by parameters other than R_{34}.

The present ^{7}Li/H value is well above the so-called Spite plateau of lithium abundances [107], and even further above the lithium values or limits found in extremely metal-poor stars [108, e.g.]. The recent predicted lithium isotopic ratio [109] does not change outside the error bar with the present new ^{7}Li/H result, it remains $^6\text{Li}/^7\text{Li} = (1.5 \pm 0.3) \times 10^{-5}$.

5.2 S-factor of the ^{7}Be$(p,\gamma)^8$B reaction

The ^{7}Be$(p,\gamma)^8$B reaction is the leading reaction of the *pp*-III branch of hydrogen burning in the Sun [85]. Its contribution to the total ^{4}He and energy production is very small, but a branch of solar neutrinos emerges from the decay of ^{8}B [110–112]. The flux of these neutrinos is well-measured (see Eq. 5.2). Moreover, a number of recent experimental determinations of $S_{17}(E)$ are available at $E > 100$ keV [113–122] (see Fig. 5.5). However, the energy of the solar Gamow window, which lies near 20 keV, was not reached by any of the experiments.

The lack of experimental data in the low-energy region can be addressed with the help of the experimentally measured flux of solar neutrinos, taking advantage of the fact that the ^{7}Be$(p,\gamma)^8$B reaction governs the production of the ^{8}B solar neutrinos. In the previous chapter, the aim was to constrain the primordial production of ^{7}Li by determining the thermonuclear reaction rate of ^{3}He$(\alpha,\gamma)^7$Be at energies relevant to the BBN. From this reason the exact knowledge of the central temperature of the Sun played a less important role in the analysis, and it was assumed to be $T_9 = 0.016$.

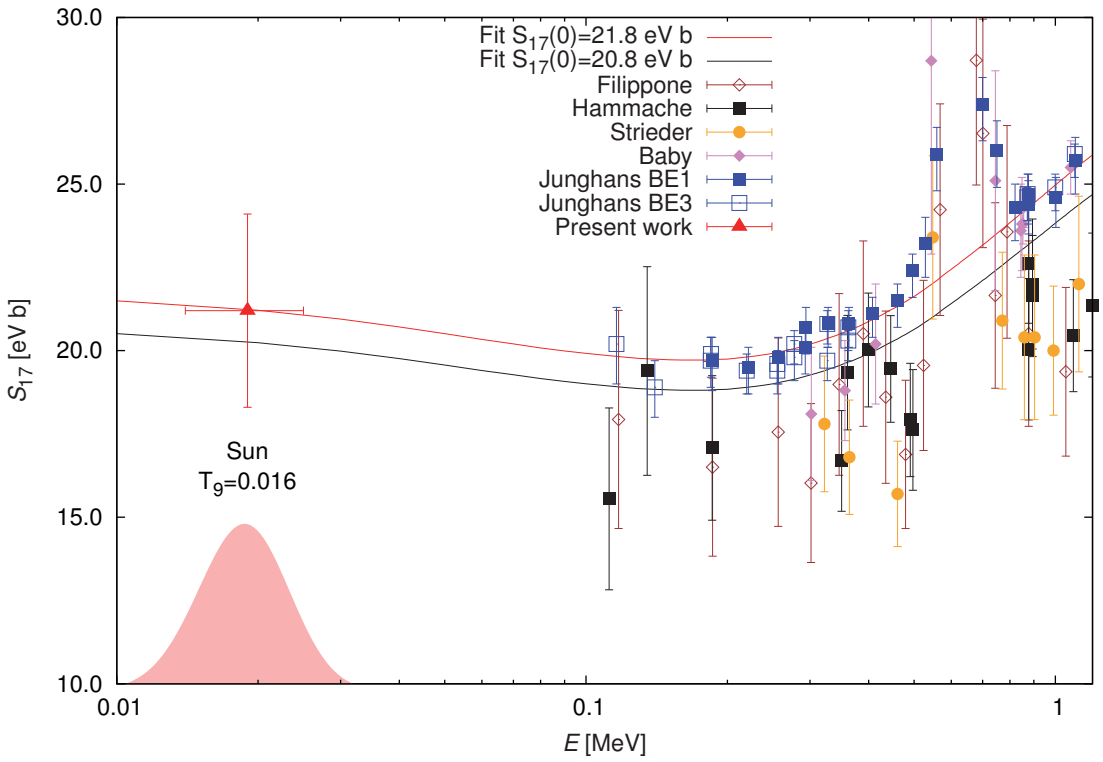

Figure 5.5: Experimental cross sections of the ^{7}Be$(p,\gamma)^8$B reaction, parametrized as the astrophysical S-factor.

In contrast to this, the present chapter provides an evaluation of the S-factor of the ^{7}Be$(p,\gamma)^8$B reaction with emphasis on the Sun. Consequently, the question of the solar core temperature requires a more careful treatment. With respect to the SSM, T_c is not an input parameter, but a result of the calculation, determined by more fundamental parameters of the model. Nevertheless, its value is strongly correlated with other output parameters of the model calculation, such as the solar neutrino fluxes [123]:

$$\phi(^7\mathrm{Be}) \propto T_c^{11} \tag{5.16}$$

$$\phi(^8\mathrm{B}) \propto T_c^{25} \tag{5.17}$$

As it can be seen, the correlation is significantly stronger for ^{8}B, than for ^{7}Be. From this reason, instead of adopting the method used in the previous chapter, a modified approach, proposed by Serenelli *et al.* [88], is used here.

The easiest way to decrease this strong ($\phi_i \propto {T_c}^{a_i}$) dependence on the T_c is to take Eq. (5.5) for two different branches of solar neutrinos and form a weighted ratio of them: ϕ_1/ϕ_2^b, where the exponent b can be approximated as $b \approx a_1/a_2$. However, one has to take into account the correlations between the neutrino fluxes ϕ_1 and ϕ_2 [88]. Therefore, b is to be determined by minimizing the dependence of the flux ratio on the net logarithmic derivatives instead [124].

The parameter of interest in the present work is the S-factor of the ^{7}Be$(p,\gamma)^8$B reaction, here denoted as S_{17}. By using the corresponding logarithmic partial derivatives from Table 5.4, one finds the following relation (where all S-factors are considered as normalized to their SF-II recommended value):

$$\frac{\phi_{\mathrm{Be}}^{\mathrm{exp}}}{\phi_{\mathrm{Be}}^{\mathrm{SSM}}} \Bigg/ \left[\frac{\phi_{\mathrm{B}}^{\mathrm{exp}}}{\phi_{\mathrm{B}}^{\mathrm{SSM}}}\right]^{0.465} = \left[L^{0.219} O^{0.002} A^{0.135} D^{-0.004}\right] \times \left[S_{11}^{0.209} S_{33}^{-0.240} S_{34}^{0.478} S_{17}^{-0.465} S_{e7}^{0.465} S_{114}^{-0.004}\right] \times \left[x_{\mathrm{C}}^{-0.011} x_{\mathrm{N}}^{-0.002} x_{\mathrm{O}}^{-0.003} x_{\mathrm{Nr}}^{0.004} x_{\mathrm{Mg}}^{0.007} x_{\mathrm{Si}}^{0.015} x_{\mathrm{S}}^{0.011} x_{\mathrm{Ar}}^{0.003} x_{\mathrm{Fe}}^{-0.026}\right] \tag{5.18}$$

The right hand side of the equation is dominated by the nuclear input parameters, while the influence of the solar elemental composition was effectively eliminated. Solving for the astrophysical S-factor S_{17}, the following relation is obtained

$$S_{17} = S_{34}^{1.028} S_{e7} \left[\frac{S_{11}^{0.449}}{S_{33}^{0.516}}\right] F_{SSM}^{2.151} \frac{\phi_{\mathrm{B}}^{\mathrm{exp}}}{\phi_{\mathrm{B}}^{\mathrm{SSM}}} \Bigg/ \left[\frac{\phi_{\mathrm{Be}}^{\mathrm{exp}}}{\phi_{\mathrm{Be}}^{\mathrm{SSM}}}\right]^{2.151} \tag{5.19}$$

where the remaining contributions from non-nuclear parameters were collected into F_{SSM}

$$F_{SSM} = \left[L^{0.219} O^{0.002} A^{0.135} D^{-0.004}\right] \times \left[x_{\mathrm{C}}^{-0.011} x_{\mathrm{N}}^{-0.002} x_{\mathrm{O}}^{-0.003} x_{\mathrm{Nr}}^{0.004} x_{\mathrm{Mg}}^{0.007} x_{\mathrm{Si}}^{0.015} x_{\mathrm{S}}^{0.011} x_{\mathrm{Ar}}^{0.003} x_{\mathrm{Fe}}^{-0.026}\right] \tag{5.20}$$

and the negligible dependence on S_{114} was disregarded.

With respect to the nuclear input in Eq. 5.19, the S-factors of the ^{3}He$(\alpha,\gamma)^7$Be and ^{3}He(^{3}He,$2p$)^{4}He reactions come with the largest uncertainties. However, due to the difference in their exponent, the nuclear error budget is dominated by S_{34}. Originally this uncertainty was estimated 5.4% by [88], however, this value can be reduced by extending the compilation of 'Solar Fusion II" [85] with the most recent experimental data from the University of Notre Dame [76]. Unfortunately, the result from the previous chapter cannot be used, because it would introduce a circular logic into the evaluation.

By following the same fitting approach as in [85] to obtain $S_{34}(0)$, one finds:

$$S_{34}(0) = 0.561 \pm 0.014_{expt} \pm 0.02_{theor} \tag{5.21}$$

where the experimental error includes both statistical and systematic uncertainties related to the experiments, while the theoretical error arises from the fact the experimental results had to be extrapolated to the solar Gamow peak with the help of a theoretical model. This means that the total uncertainty on S_{34} is reduced to 4.3%. Adding this value in quadrature to the uncertainty of S_{11}, S_{33} and S_{e7}, the total nuclear contribution to the error budget amounts to 5.6%.

Last, one has to take into account the solar neutrino flux observations. At the first, one may expect that this part of the total error budget is mainly governed by the ^{8}B neutrino flux, due to its direct link to the ^{7}Be$(p,\gamma)^8$B reaction. In reality however, the dominant role is played by the ^{7}Be neutrino flux via the preceding ^{3}He$(\alpha,\gamma)^7$Be reaction. This is reflected in its exponent of 2.151, which considerably inflates the 5.5% uncertainty of ^{7}Be neutrino flux. Therefore, this part of the equation will contribute 12.5% towards the total error.

Table 5.4: Estimated 1σ uncertainties of SSM model parameters and computed logarithmic partial derivatives for the $\phi_{\mathrm{Be}}/\phi_{\mathrm{B}}^{0.465}$ ratio as defined by Eq. (5.4). The logarithmic partial derivatives for ϕ_{Be} and ϕ_{B} (listed in Table 5.1) are repeated here. The values are taken from [88], except for the uncertainty of S_{34}, which was calculated based on Table 5.3. See the text for details.

Parameter β_j	$\frac{\Delta\beta_j}{\beta_j}(\%)$	$\alpha(\phi_{\mathrm{Be}}, j)$	$\alpha(\phi_{\mathrm{B}}, j)$	$\alpha(\frac{\phi_{\mathrm{Be}}}{\phi_{\mathrm{B}}^{0.465}}, j)$
Luminosity	0.4	3.434	6.914	0.219
Opacity	2.5	1.210	2.611	0.002
Age	0.44	0.760	1.345	0.135
Diffusion	15.0	0.126	0.267	-0.004
S_{11} - p+p	1.0	-1.024	-2.651	0.209
S_{33} - ^{3}He +^{3}He	5.2	-0.428	-0.405	-0.240
S_{34} - ^{3}He +^{4}He	4.3*	0.853	0.806	0.478
S_{17} - p +^{7}Be	7.7	0.000	1.000	-0.465
S_{e7} - e +^{7}Be	2.0	0.000	-1.000	0.465
S_{114} - p +^{1}4N	7.5	-0.001	0.007	-0.004
C	24.6	0.002	0.027	-0.011
N	24.6	0.001	0.007	-0.002
O	35.0	0.062	0.139	-0.003
Ne	45.3	0.055	0.109	0.004
Mg	11.8	0.050	0.092	0.007
Si	11.8	0.104	0.192	0.015
S	13.8	0.076	0.140	0.011
Ar	34.9	0.019	0.035	0.003
Fe	11.8	0.207	0.502	-0.026

Summing up the contributions of all three main sources of error, one finds that the method followed here provides an estimate on S_{17} with total uncertainty of 13.7%.

Despite the fact the most of the dependence on the solar elemental abundance was removed from Eq. 5.19, the result is still slightly influenced by the choice of neutrino flux prediction: GS98 suggest an upward revision of 5.1% compared to the 'Solar Fusion II" recommendation, while AGSS09 values result in a correction of 4.8%. As a conservative assumption, the average of the two flux recommendations (see Table 5.2) was used.

The S-factor of the ^{7}Be$(p,\gamma)^8$B reaction was then redetermined in the solar Gamow peak by accepting the previous "Solar Fusion II" recommendation [85], and rescaling according to Eq. 5.19:

$$S_{17}(19^{+6}_{-5}) = 21.2 \pm 2.9 \text{ eV b} \tag{5.22}$$

Following the "Solar Fusion II" approach, the energy dependence of the S-factor was assumed to be described by the "Minnesota" calculation by Descouvemont [125]. By fitting the "Minnesota" curve to the current new data point (red curve in Fig. 5.5), $S_{17}(0)$ was found to be

$$S_{17}(0) = 21.8 \pm 3.0 \text{ eV b} \tag{5.23}$$

As it can be seen from Table 5.5, the resulting $S_{17}(0)$ is in good agreement with the previously reported values. However, it is worth to note, that the rescaled "Minnesota" curve seems to favour the results by Junghans *et al.* [120–122] (Fig. 5.5), which are systematically higher than the values observed in other experiments [113–119].

As a next step, an analysis of all experimental data points was carried out including the new data point using again the "Minnesota" fit. The resulting combined average was

$$S_{17}(0) = 20.8 \pm 0.6_{\text{stat}} \text{ eV b} \tag{5.24}$$

where the uncertainty was obtained by multiplying the raw uncertainty of the fitting approach with the inflation factor reported in Table 5.5.

Compared to the previous "Solar Fusion II" value of $20.8 \pm 0.7_{\text{expt}} \pm 1.4_{\text{theor}}$ eV b for $E \leq 475$ keV, it is evident that the uncertainty is greatly reduced. This is due to the fact, that the current approach directly estimates the S-factor of ^{7}Be$(p,\gamma)^8$B in the relevant astrophysical energy range (solar Gamow window), thus there is no need for extrapolation. Consequently, the corresponding error bar ($\pm 1.4_{\text{theor}}$ eV b) can be omitted. The precision of this solar neutrino based approach is expected to increase in the future with more precise measurements of the solar ^{7}Be flux [126].

Table 5.5: Determination of $S_{17}(0)$ from recent experimental data, using the Minnesota calculation by Descouvemont [125] as fit function.

Reference	$S_{17}(0)$ [eV b]	Inflation factor
Filippone [113]	19.4 ± 2.4	
Hammache [114, 115]	19.3 ± 1.1	
Strieder [116]	17.2 ± 1.7	
Baby [117–119]	20.2 ± 1.4	
Junghans [120–122]	21.6 ± 0.5	
Present work	21.8 ± 3.0	
Combined result	20.8 ± 0.6	1.48

Chapter 6

Discussion

6.1 Discussion of the present new LUNA results

The resonance strengths obtained in the BGO phase of the LUNA ^{22}Ne$(p,\gamma)^{23}$Na experiment are listed in Table 6.1 along with their values from the literature.

The newly obtained upper limits on the putative resonances at $E_p^{\rm lab} = 71$ and 105 keV are in a good agreement both with the data from indirect [30], and direct measurements [35, 38]. Compared to the previous upper limits reported by LUNA [38], a two orders of magnitude reduction was achieved owing to the greatly increased sensitivity of the BGO detector over the previous HPGe based setup.

The agreement between the new data and the previous direct upper limits form Görres *et al.* [35] is reasonably good for the three higher energy resonances discussed here. The observed strength of the resonance at $E_p^{\rm lab} = 259.7$ keV is somewhat higher than expected, but the LUNA-HPGe results also suggested a higher $\omega\gamma$ value [38].

In case of the indirect upper limits by Hale *et al.* [30], the agreement is not good: For the resonance at $E_p^{\rm lab} = 156.2$ keV ($E_x = 8943.5$ keV), the indirect measurement predict an $\omega\gamma$ which is at least two orders of magnitude lower than the one observed in the present (and also in the previous) LUNA experiment. However, the indirect upper limit was based purely on the spin/parity assignment ($E_x = 8945$ keV, $7/2^-$) [30], since the resonance was not actually observed. On the other hand, the experiment by Jenkins *et al.* [31] suggests the existence of a doublet state instead of one level at the excitation energy of $E_x = 8944$ keV, with tentative spin/parity assignments of $3/2^+$ and $7/2^-$ respectively (see Fig. 2.2).

Therefore, it is likely that the present resonance strength and the upper limit by Hale *et al.* are actually derived for different members of the doublet: For the low proton energies used here, the population of the low spin $3/2^+$ level is much more probable due to the angular momentum barrier. The derived decay scheme of the level (both from the BGO and HPGe phase) is in a good agreement with the branching reported for $3/2^+$ [31], while none of the γ-transitions assigned to the $7/2^-$ level were observed (see Table 6.2).

In case of the resonance at $E_p^{\rm lab} = 189.5$ keV ($E_x = 8975.3$ keV), the present measured resonance strength is in agreement with the previous indirect upper limit [30]. The agreement may be explained by the fact, that this level was found to be a single level with $5/2^+$ [31]. On the other hand, in Ref. [31], only the transition R$\rightarrow$ 2982 was considered. This is in contradiction both with the current experiment

and the latest direct data from the literature [37,38], which suggest a more detailed decay scheme. The partial resonance strength observed in the present experiment for the R→ 2982 transition is 7.2×10^{-8} eV, which is two orders of magnitude lower than indirect upper limit [30].

Similar to the first resonance, the $E_x = 9042.4$ keV level corresponding to the resonance at $E_p^{\mathrm{lab}} = 259.7$ keV is again believed to be part of a doublet [31], which might explain the discrepancy between the direct $\omega\gamma$ values and the indirect upper limits by [30]. As can be seen in Table 6.2, neither of the LUNA experiments could observe the transitions assigned to the $15/2^+$ doublet member. On the other hand, the transitions to 440 and 2076 keV levels were both detected, suggesting that in the present experiment the level with $7/2^+$ (or $9/2^+$) was populated. This assumption is again further supported by the high angular momentum barrier in case of the $15/2^+$ level. The branching ratios from [31] do not seem to reflect properly the actual decay scheme.

Considering only the data from direct measurements, it is evident that there is tension between the LUNA-HPGe and LUNA-BGO data (Table 6.1 and Fig. 6.1). The new resonance strengths for all three resonances are higher than the previously reported ones. Moreover, in case of the 156.2 keV and 189.5 keV resonances, the branching ratios observed in the present experiment are different from the ones that had been found in the LUNA-HPGe phase (see Table 6.2).

The 156 keV resonance seems to have 5% decay probability to the ground state, which transition was not detected previously due to the limited efficiency of the HPGe detector for high energy photons. Similarly, in case of the 189 keV resonance, the 2.2% contribution from the transition to the $E_x = 3678$ keV state was not observed in the previous phase. The determination of the resonance strength with a HPGe detector is based on the individual detection of each primary γ-transitions from the excited state, and the precise knowledge of their branching ratios. In contrast to this, the measurements with the summing BGO detector are based on the detection of the add-back peak in the spectrum, thus the resulting $\omega\gamma$ value is less sensitive to the branching ratios. The difference in the branching ratios can partly account for the observed discrepancy in the strength of the resonances at 156.2 and 189.5 keV. In case of the resonance at 259.7 keV, the present experiment confirmed the previous decay scheme.

The discrepancy HPGe-BGO can be also due to systematic differences in the detector type and data acquisition mode used: While in most cases the high efficiency and large volume of the BGO detector is advantageous, it can also have certain drawbacks. For example random summing events in the detector can create an additional background contribution to the experimental ROI. Moreover, it is also possible that add-back peaks of contaminant reactions with similar Q-value as the ^{22}Ne(p,γ)^{23}Na reaction, such as the ^{18}O(p,γ)^{19}F (Q=7.993 MeV) or ^{22}Na(p,γ)^{23}Mg (Q=7.580 MeV) reactions, are not resolved properly and partly summed into the ROI. However, no contaminant peaks were found in the gated single sum spectra created from add-back events remaining in the ROI after background subtraction. Therefore, it is believed that the beam induced background was properly estimated by the in-beam spectra measured in argon at the same beam energy.

The previous LUNA phase using two HPGe detectors at different angles (90° and 55°) observed an isotropic distribution of γ-rays emitted during the resonant capture reactions [38]. Nevertheless, if there is some angular correlation, which is

uncorrected for, the $\omega\gamma$ values derived in the HPGe-phase would be more sensitive to it than the present ones, since the BGO detector covers a near 4π solid angle.

The new $\omega\gamma$ values for resonances at 156.2 and 189.5 keV are in fact closer to data obtained by Kelly *et al.* [37]. However, the reported branching ratios fit the present BGO-phase data worse, than the previous recommendation by LUNA. Similarly to the LUNA-HPGe data, no ground state transition was observed by Kelly *et al.* for the 156.2 keV resonance. However, in this case the inclusion of the missing strength increases the discrepancy to LUNA-BGO, since the $\omega\gamma$ values from TUNL are generally higher than the ones seen in the present experiment.

Unfortunately, the TUNL group did not report any strength for the resonance at 259.7 keV. Thus, the only available information is from the two consecutive phases of the LUNA experiment. The $\omega\gamma$ value is 27% higher than the previous one, however, the values are consistent with each other on 2σ level. In this case, no considerable difference was seen between the branching ratios observed in BGO and the HPGe phases. The difference in the observed strengths has to originate from an other reason.

Nevertheless, by comparing the quoted uncertainties for the experiments (TUNL, LUNA-HPGe, LUNA-BGO), the advantage of the LUNA approach is clearly visible: Due to its exposed location, the measurements at TUNL had to rely on an active muon veto to reduce the background generated by cosmic muons. In LUNA, the muon induced background is passively reduced by six orders of magnitude [45] due to the 1400m rock overburden. This not only allows a less complicated experimental design, but also offers an increase in counting statistics, since the use of an active veto inevitably leads to losses also in valuable events. While in the LUNA-BGO experiment even the weaker transitions from the decay of the three here discussed resonances could be directly identified in the spectra, the TUNL group had to rely on a more complex method in order to evaluate their spectra: for each possible γ-transition a Monte Carlo generated templates was created. These templates were then included in a complicated Markov-chain based fitting procedure to reproduce the experimental spectra. This approach is in principle feasible, but can also have its pitfalls: the strength of the 156.2 keV was originally estimated three times higher in Kelly's PhD thesis [36] than it was reported in the final publication [37].

With respect to the non-resonant S-factor, the present experiment did not find any evidence for a direct capture process for $E_p^{\rm ini} \leq 310$ keV. The observed non-resonant yields are consistent with the expected tail contribution from the broad resonances near and under the proton threshold ($E_{\rm res}^{\rm cm} = 35$ and -130 keV). Thus, the present results did not confirm the previous $S = const = 62$ keV b value, which was suggested by Görres *et al.* [40].

The impact of the new data on the thermonuclear reaction rate is illustrated in the Figures 6.2, 6.3 and 6.4. Compared only to the LUNA-HPGe rate (Fig. 6.2), the effect of the new upper limits on resonance 71 and 105 keV is evident: the median rate is decreased for $0.04 \leq T_9 \leq 0.15$. The rate uncertainty is also considerably reduced. On the other hand, the somewhat higher $\omega\gamma$ values for the resonances at 156.2, 189.5 and 259.7 keV leads to an almost negligible increase in the rate for temperatures around 0.2 GK. The rate uncertainty at low energies is determined by the resonances at 37 and 71 keV.

The improvement granted by the higher luminosity of the BGO is clearly reflected in the new reaction rate in case of the resonances at 71 and 105 keV. The new upper

Table 6.1: Comparison of the most recent low energy $\omega\gamma$ values

E_p^{lab} [keV]	Resonance strength $\omega\gamma$ [eV]				
	Literature indirect	Literature direct			Present
	Hale *et al.* [30]	Görres *et al.* [35]	Kelly *et al.* [37]	LUNA-HPGe [38, 50]	LUNA-BGO
71	$\leq 1.9 \times 10^{-10}$	$\leq 3.2 \times 10^{-6}$		$\leq 1.5 \times 10^{-9}$	$\leq 5.8 \times 10^{-11}$
105	$\leq 1.4 \times 10^{-7}$	$\leq 0.6 \times 10^{-6}$		$\leq 7.6 \times 10^{-9}$	$\leq 7.0 \times 10^{-11}$
156.2	$\leq 9.2 \times 10^{-9}$	$\leq 1.0 \times 10^{-6}$	$(2.03 \pm 0.18_{\mathrm{stat}} \pm 0.35_{\mathrm{sys}}) \times 10^{-7}$	$(1.48 \pm 0.09_{\mathrm{stat}} \pm 0.04_{\mathrm{sys}}) \times 10^{-7}$	$(1.84 \pm 0.04_{\mathrm{stat}} \pm 0.09_{\mathrm{sys}}) \times 10^{-7}$
189.5	$\leq 3.4 \times 10^{-6}$	$\leq 2.6 \times 10^{-6}$	$(2.32 \pm 0.12_{\mathrm{stat}} \pm 0.30_{\mathrm{sys}}) \times 10^{-6}$	$(1.87 \pm 0.03_{\mathrm{stat}} \pm 0.05_{\mathrm{sys}}) \times 10^{-6}$	$(2.28 \pm 0.02_{\mathrm{stat}} \pm 0.10_{\mathrm{sys}}) \times 10^{-6}$
259.7	$\leq 1.3 \times 10^{-7}$	$\leq 2.6 \times 10^{-6}$		$(6.89 \pm 0.07_{\mathrm{stat}} \pm 0.15_{\mathrm{sys}}) \times 10^{-6}$	$(8.74 \pm 0.03_{\mathrm{stat}} \pm 0.39_{\mathrm{sys}}) \times 10^{-6}$

Table 6.2: Branching ratios for the resonances at $E_p^{\mathrm{lab}} = 156.2$, 189.5, and 259.7 keV

$E_{\mathrm{res}}^{\mathrm{lab}}$	J_{res}^{π}	γ-transition	Branching [%]			
			Jenkins *et al.* [31]	Kelly *et al.* [37]	LUNA-HPGe [38]	Present
156.2 keV	$3/2^+$	R$\rightarrow$ 0				5 (1)
	$7/2^-$	R$\rightarrow$ 2076	47 (4)			
	$7/2^-$	R$\rightarrow$ 2703	12 (2)			
	$3/2^+$	R$\rightarrow$ 2391	39 (6)	20 (4)	23 (4)	32 (3)
	$3/2^+$	R$\rightarrow$ 3914	61 (30)	80 (6)	77 (4)	63 (3)
	$7/2^-$	R$\rightarrow$ 6353	10 (2)			
	$7/2^-$	R$\rightarrow$ 7125	31 (2)			
189.5 keV	$5/2^+$	R$\rightarrow$ 0		5.3 (1.4)		
	$5/2^+$	R$\rightarrow$ 440		37.7 (1.5)	42.8 (0.9)	38.0 (0.9)
	$5/2^+$	R$\rightarrow$ 2076		39.8 (1.3)	47.9 (0.9)	50.6 (0.9)
	$5/2^+$	R$\rightarrow$ 2982	100	5.0 (0.8)	3.7 (0.5)	3.2 (0.5)
	$5/2^+$	R$\rightarrow$ 3678		2.2 (0.8)		2.2 (0.2)
	$5/2^+$	R$\rightarrow$ 3914		3.1 (0.6)	1.1 (0.3)	2.0 (0.5)
	$5/2^+$	R$\rightarrow$ 4775		≤ 3.0	1.8 (0.2)	1.6 (0.2)
	$5/2^+$	R$\rightarrow$ 6618		4.7 (0.9)	2.7 (0.2)	2.4 (0.2)
259.7 keV	$7/2^+$ $9/2^+$	R$\rightarrow$ 440	16 (4)		45.4 (0.9)	46.0 (0.9)
	$7/2^+$ $9/2^+$	R$\rightarrow$ 2076	84 (4)		18.7 (0.6)	18.9 (0.6)
	$7/2^+$ $9/2^+$	R$\rightarrow$ 2704			10.9 (0.5)	11.0 (0.5)
	$7/2^+$ $9/2^+$	R$\rightarrow$ 3848			13.3 (0.5)	13.5 (0.5)
	$7/2^+$ $9/2^+$	R$\rightarrow$ 3914			1.8 (0.4)	1.8 (0.4)
	$15/2^+$	R$\rightarrow$ 5533	12 (2)			
	$7/2^+$ $9/2^+$	R$\rightarrow$ 5927			3.6 (0.2)	3.0 (0.2)
	$7/2^+$ $9/2^+$	R$\rightarrow$ 6042			2.6 (0.2)	2.0 (0.2)
	$7/2^+$ $9/2^+$	R$\rightarrow$ 6355			1.5 (0.2)	1.5 (0.2)
	$7/2^+$ $9/2^+$	R$\rightarrow$ 6820			2.2 (0.2)	2.2 (0.2)
	$15/2^+$	R$\rightarrow$ 6234	76 (5)			
	$15/2^+$	R$\rightarrow$ 7267	12 (5)			

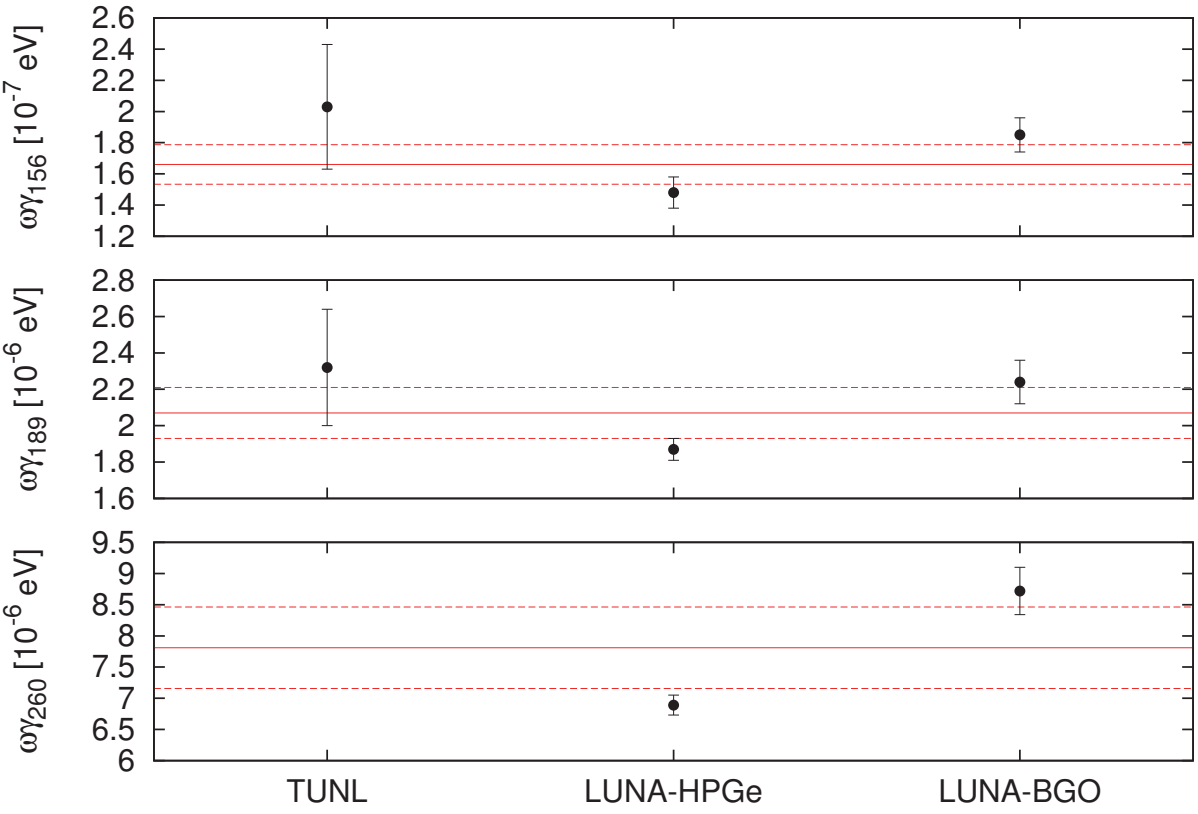

Figure 6.1: Comparison of the experimental resonances strengths for the resonances at $E_p^{\text{lab}} = 156.2$, 189.5 and 260 keV including data from TUNL [37], the previous, HPGe based [38], and the present, BGO based experiments at LUNA. The red line corresponds to a simple average of the LUNA $\omega\gamma$ values.

limits compared to the ones from the HPGe phase are more robust against small statistical fluctuations in the counting rate.

As can be seen in Fig. 6.3, the median of the new reaction rate is almost identical to the one by TUNL [37]. The LUNA-BGO rate however, is slightly lower for temperatures $0.1 \leq T_9$, due to the differences in the strengths of the resonances at 156.2 and 189.5 keV. Similar to the STARLIB-2013 [39] rate, the new TUNL rate does not consider the resonances at 71 and 105 keV. Their strength is simply set to zero, along with the associated uncertainty. This explains why, the LUNA rate have significant uncertainty below 0.1 GK.

Last, but not least, Fig. 6.4 compares the present and all available other rate compilations from the literature [21,37,38], normalised to STARLIB-2013 [39]. Compared to NACRE [21], the rate is decreased by more than two orders of magnitude in the temperature range $0.03 \leq T_9 \leq 0.3$, which can be seen as a success of underground nuclear astrophysics. The enhancement over the STARLIB-2013 rate in the same energy range is due to the resonances at 156.2 and 189.5 keV. In STARLIB-2013, the resonance at 156.2 keV is still considered with the strength from the indirect measurement of Hale *et al.* [30], while in case of the resonance at 189.5 keV the upper limit provided by Görres *et al.* [40] is used.

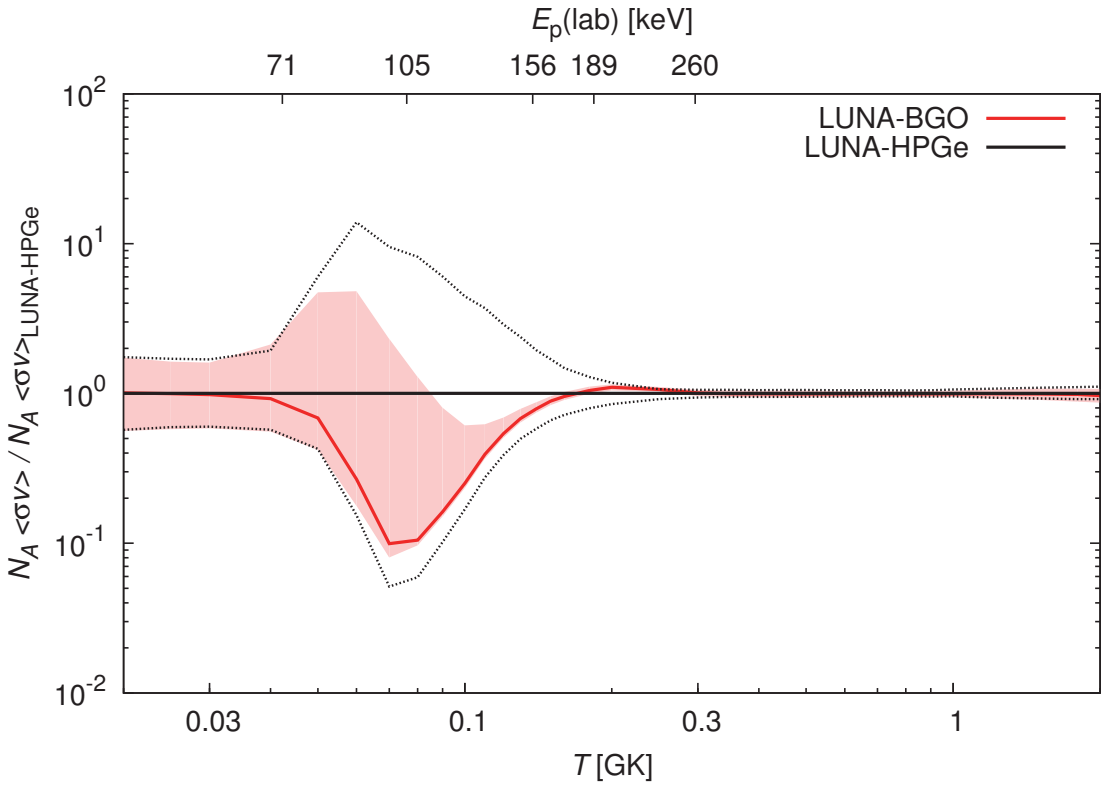

Figure 6.2: Comparison of the LUNA-BGO [38] and LUNA-HPGe reaction rate.

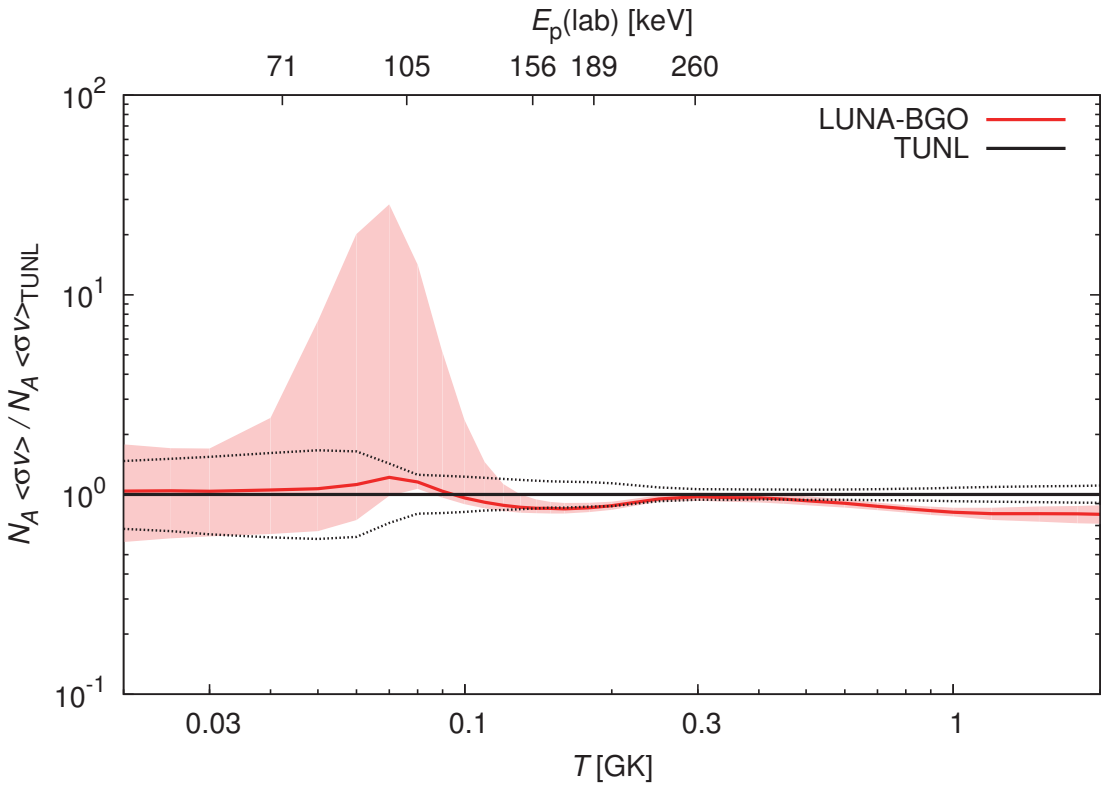

Figure 6.3: Comparison of the TUNL [37] and LUNA-HPGe reaction rate.

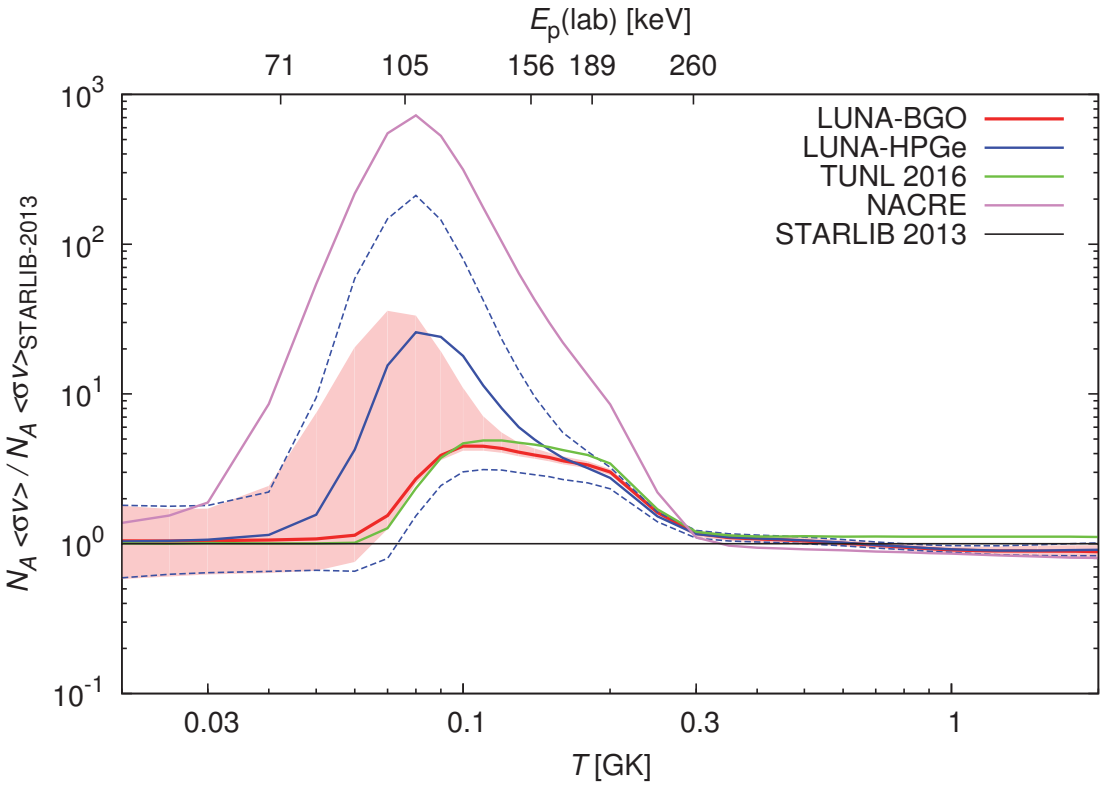

Figure 6.4: Comparison of the LUNA-BGO ^{22}Ne$(p,\gamma)^{23}$Na reaction rate to the previous compilations, normalised to the STARLIB-2013 rate. In case of the LUNA-BGO rate, the red area represents the rate uncertainty, while in case of the LUNA-HPGe [38], it is indicated by the dashed blue lines. For NACRE [21], STARLIB-2013 [39] and TUNL [37] the rate uncertainty is not shown.

6.2 Discussion of solar neutrino based results

As it was demonstrated in Chapter 5, the flux measurement of the solar ^{7}Be and ^{8}B neutrinos reached such precision, that they can provide additional information on the underlying nuclear reactions of the solar hydrogen-burning. In contrast to the "classical" experimental approach, the solar neutrino based determination of the S-factor has the advantage that the deduced values of S_{34} or S_{17} per definition correspond to the astrophysically relevant energies. Therefore, no extrapolation is necessary to the solar Gamow peak in contrast to the experimental data obtained at higher energies.

However, both versions of the method used here rely on the assumption, that the standard solar model (SSM) is correct. This assumption has the disadvantage that the measured fluxes cannot be used at the same time to check the validity of the description of the Sun. Furthermore, the results considering S_{34} cannot be taken into account during the determination of S_{17}, and vice versa.

Last, but not least, the on-going discussion regarding the elemental composition of the Sun affects the predictive power of the SSM, and thus the uncertainty on the S-factor, until the contradiction between the GS98 [89] and AGSS09 [90] elemental abundances is resolved.

Chapter 7

Summary

The ^{22}Ne$(p,\gamma)^{23}$Na reaction has been studied with a direct experiment at LUNA in the energy range relevant to AGB stars and classical novae. As a follow up to the previous LUNA experiment [38], the aim of the present work was to investigate the tentative resonances at $E_p^{\rm lab} = 71$ and 105 keV, and to study the direct capture component of the reaction rate below 400 keV.

The experimental setup was based on a differentially pumped, windowless gas-target system circulating enriched ^{22}Ne gas. The detection of γ-rays was done by a large, segmented bismuth germanate (BGO) detector surrounding the target chamber. The signals from each segment were read out separately and recorded in list-mode by a CAEN V1724 digitizer card. The intense proton beam necessary for the experiment was provided by the LUNA-400 electrostatic accelerator located deep underground.

The density profile of the target gas was determined by measuring the temperature and the pressure inside the target chamber as function of the position. The efficiency of the BGO detector was studied with point-like radioactive sources and the well-known ^{14}N(p,γ)^{15}O resonance at $E_p^{\rm lab} = 278$ keV. The data were used to validate the GEANT4 simulation of the detector, which was, in turn, later used to calculate the add-back detection efficiency.

Much effort was devoted to the study of the resonances at $E_p^{\rm lab} = 71$ and 105 keV, by collecting statistics at several beam energies near their nominal energy. No clear signature of a resonance was observed. However, owing to the improved sensitivity, the upper limits by the previous LUNA phase were reduced by two orders of magnitude, to the 10^{-11} eV level.

Furthermore, the strengths of resonances at $E_p^{\rm lab} = 156.2$, 189.5 and 259.7 keV were remeasured, and the decay schemes of the corresponding levels were studied. The new strengths were found to be 20% higher than the values previously reported by the LUNA-HPGe phase. Possible origins of this discrepancy have been discussed.

The direct capture process was studied at $E_p^{\rm ini}$= 188.0, 205.2, 250.1, and 310.0 keV. The obtained S-factors were consistent with the non-resonant contribution from the sub-threshold resonance at $E_{\rm res}^{\rm cm} = -130$ keV, and from the low energy resonance at $E_{\rm res}^{\rm cm} = 35$ keV. Therefore, in contrast to the previous measurement by Görres *et al.* [40], the present experiment did not confirm the existence of a separate direct capture component at all.

Based on the new results, the thermonuclear reaction rate of ^{22}Ne$(p,\gamma)^{23}$Na was redetermined. The new rate is consistent with the previous LUNA-HPGe rate, but

its uncertainty was greatly reduced for temperatures from 0.04 to 0.2 GK, because of the new upper limits. The rate is also consistent with the recent determination from the TUNL group [37].

In addition to the experimental work at LUNA, the ^{3}He(α,γ)^{7}Be and ^{7}Be(p,γ)^{8}B reactions of the *pp*-chain hydrogen-burning were studied using the most recent solar neutrino flux data from the Borexino [70] and SNO experiments [68]. Based on the standard solar model [65], and the experimentally measured flux of the ^{7}Be and ^{8}B branches of solar neutrinos, the corresponding S-factors S_{34} and S_{17} were obtained at energies of the solar Gamow peak.

Acknowledgement

I am very grateful to PD Dr. Daniel Bemmerer and Prof. Dr. Kai Zuber, who introduced me to the world of underground nuclear astrophysics, and supervised my work at the Helmholtz-Zentrum Dresden-Rossendorf and at the TU Dresden, which led eventually to this dissertation.

I am indebted to Alba Formicola, Matthias Junker, and Paolo Prati for welcoming me as a member of the LUNA Collaboration and making it possible for me to perform all the necessary measurements for the present work. I enjoyed the stimulating atmosphere within the LUNA gas target group, and thank in particular Antonio Caciolli and Federico Ferraro. However, the experiments for the present study would not have been completed without the cooperation from all the other members of the LUNA Collaboration.

Last, but not least, I would like to acknowledge the financial support of the Helmholtz Association through the Nuclear Astrophysics Virtual Institute (NAVI, HGF VH-VI-417), and the Graduate Academy of TU Dresden.

Appendix A

Tail contributions to the non-resonant S-factor

The following formalism was developed based on the corresponding chapters of [1], considering single-level, s-wave resonances of Breit-Wigner shape for (p, γ) reactions, where only two reactions channels are open.

A.1 Breit-Wigner cross section for sub-threshold resonances

$$\sigma_{BW}(E) = \pi\lambda^2 \frac{2J+1}{(2j_p+1)(2j_t+1)}(1+\delta_{12})\frac{\Gamma_p(E)\Gamma_\gamma(E)}{(E-E_R-\Delta)^2+(\Gamma(E)/2)^2} \tag{A.1}$$

where λ is the de Broglie wavelength and j_p, j_t, J are the spins of the bombarding proton, the target nucleus, and resonant state respectively.

In case of s-wave protons ($j_p = 0$), the energy dependence of the gamma-width $\Gamma_\gamma(E)$ is given by the following expression

$$\Gamma_\gamma(E) = \left[\frac{E+Q}{E_R+Q}\right]^3 \Gamma_\gamma(E_R) \tag{A.2}$$

where Q is the Q-value of the reaction and $\Gamma_\gamma(E_R)$ the value of the gamma width at the resonance energy E_R.

The energy dependence of the proton width is determined by the s-wave penetration factor $P_{l=0}(E)$

$$\Gamma_p(E) = 2P_{l=0}(E)\gamma^2_{p,l=0} \tag{A.3}$$

where the reduced proton width $\gamma^2_{p,l=0}$ can be expressed as function of the spectroscopic factor C^2S and the single particle proton width $\theta^2_{l=0}$

$$\gamma^2_{p,l=0} = \frac{\hbar^2}{\mu R^2} C^2 S \theta^2_{l=0} \tag{A.4}$$

with μ as the rudced mass of the target-projectile system, and R interaction radius. The energy dependence of the total width is simply given by $\Gamma(E) = \Gamma_p(E) + \Gamma_\gamma(E)$:

Last, but not least the shift correction Δ to the resonance energy can be calculated from the reduced proton width $\gamma^2_{p,l=0}$ and the shift factor $S_{l=0}(E)$

$$\Delta = -\Big[S_{l=0}(E) - S_{l=0}(E_R)\Big]\gamma^2_{p,l=0} \tag{A.5}$$

A.2 Breit-Wigner cross section for broad resonances above the Coulomb threshold

$$\sigma_{BW}(E) = \pi\lambda^2 \frac{2J+1}{(2j_p+1)(2j_t+1)}(1+\delta_{12})\frac{\Gamma_p(E)\Gamma_\gamma(E)}{(E-E_R)^2+(\Gamma(E)/2)^2} \tag{A.6}$$

$$\Gamma_\gamma(E) = \left[\frac{E+Q}{E_R+Q}\right]^3 \Gamma_\gamma(E_R) \tag{A.7}$$

$$\Gamma_p(E) = \frac{P_{l=0}(E)}{P_{l=0}(E_R)}\Gamma_p E_R \tag{A.8}$$

where $\Gamma_p(E_R)$ the value of the proton width at the resonance energy.

A.3 Determination of $P_l(E)$ and $S_l(E)$

The penetration $P_l(E)$ and shift $S_l(E)$ can be determined with help of the regular $F_l(E)$ and irregular $G_l(E)$ Coulomb wave-functions

$$P_l(E) = R\left(\frac{k}{F_l(E)^2+G_l(E)^2}\right)_{r=R} \tag{A.9}$$

$$S_l(E) = R\left(\frac{F_l(E)\frac{\partial F_l(E)}{\partial r}+G_l(E)\frac{\partial G_l(E)}{\partial r}}{F_l(E)^2+G_l(E)^2}\right)_{r=R} \tag{A.10}$$

where k is the wave-number. In both expressions, $F_l(E)$ and $G_l(E)$ have to be evaluated at radius R

$$R = 1.25\mathrm{fm}\left(\mathrm{A_t^{1/3}}+\mathrm{A_p^{1/3}}\right) \tag{A.11}$$

where A_p and A_t are the atomic mass of projectile and target.

Appendix B

^{22}Ne$(p,\gamma)^{23}$Na reaction rate (tabulated)

T_9	$N_A\langle\sigma v\rangle$ [cm^{3}s^{-1}mole^{-1}]		
	Low rate	Median rate	High rate
0.01	2.86×10^{-25}	7.01×10^{-25}	1.67×10^{-24}
0.011	1.10×10^{-23}	2.55×10^{-23}	5.68×10^{-23}
0.012	2.28×10^{-22}	5.03×10^{-22}	1.07×10^{-21}
0.013	2.92×10^{-21}	6.22×10^{-21}	1.26×10^{-20}
0.014	2.59×10^{-20}	5.31×10^{-20}	1.04×10^{-19}
0.015	1.71×10^{-19}	3.39×10^{-19}	6.41×10^{-19}
0.016	8.86×10^{-19}	1.70×10^{-18}	3.15×10^{-18}
0.018	1.34×10^{-17}	2.47×10^{-17}	4.40×10^{-17}
0.02	1.15×10^{-16}	2.07×10^{-16}	3.55×10^{-16}
0.025	5.24×10^{-15}	9.06×10^{-15}	1.48×10^{-14}
0.03	6.36×10^{-14}	1.07×10^{-13}	1.75×10^{-13}
0.04	1.30×10^{-12}	2.16×10^{-12}	4.96×10^{-12}
0.05	7.60×10^{-12}	1.24×10^{-11}	8.57×10^{-11}
0.06	2.83×10^{-11}	4.26×10^{-11}	7.66×10^{-10}
0.07	1.31×10^{-10}	1.62×10^{-10}	3.77×10^{-09}
0.08	9.61×10^{-10}	1.04×10^{-09}	1.28×10^{-08}
0.09	6.83×10^{-09}	7.35×10^{-09}	3.64×10^{-08}
0.1	3.85×10^{-08}	4.14×10^{-08}	1.01×10^{-07}
0.11	1.68×10^{-07}	1.80×10^{-07}	2.85×10^{-07}
0.12	5.87×10^{-07}	6.27×10^{-07}	8.01×10^{-07}
0.13	1.72×10^{-06}	1.83×10^{-06}	2.12×10^{-06}
0.14	4.36×10^{-06}	4.62×10^{-06}	5.11×10^{-06}
0.15	9.80×10^{-06}	1.04×10^{-05}	1.12×10^{-05}
0.16	2.00×10^{-05}	2.11×10^{-05}	2.26×10^{-05}
0.18	6.67×10^{-05}	7.01×10^{-05}	7.42×10^{-05}
0.2	1.81×10^{-04}	1.90×10^{-04}	1.99×10^{-04}
0.25	1.85×10^{-03}	1.91×10^{-03}	1.99×10^{-03}
0.3	2.21×10^{-02}	2.32×10^{-02}	2.43×10^{-02}
0.35	1.81×10^{-01}	1.90×10^{-01}	2.00×10^{-01}
0.4	9.22×10^{-01}	9.72×10^{-01}	1.02×10^{00}

T_9	$N_A\langle\sigma v\rangle$ [cm^{3}s^{-1}mole^{-1}]		
	Low rate	Median rate	High rate
0.45	3.30×10^{00}	3.48×10^{00}	3.66×10^{00}
0.5	9.20×10^{00}	9.68×10^{00}	1.02×10^{01}
0.6	4.29×10^{01}	4.51×10^{01}	4.72×10^{01}
0.7	1.31×10^{02}	1.37×10^{02}	1.43×10^{02}
0.8	3.06×10^{02}	3.20×10^{02}	3.34×10^{02}
0.9	6.01×10^{02}	6.31×10^{02}	6.61×10^{02}
1	1.05×10^{03}	1.10×10^{03}	1.16×10^{03}
1.2	2.95×10^{03}	3.17×10^{03}	3.39×10^{03}
1.5	6.11×10^{03}	6.69×10^{03}	7.27×10^{03}
1.8	1.04×10^{04}	1.16×10^{04}	1.27×10^{04}
2	1.57×10^{04}	1.75×10^{04}	1.94×10^{04}
2.5	2.77×10^{04}	3.11×10^{04}	3.45×10^{04}
3	3.97×10^{04}	4.46×10^{04}	4.96×10^{04}
3.5	5.02×10^{04}	5.65×10^{04}	6.29×10^{04}
4	5.89×10^{04}	6.62×10^{04}	7.36×10^{04}

Appendix C

^{3}He$(\alpha,\gamma)^7$Be reaction rate (tabulated)

The reaction rate (Table C.1) is reproduced within $\pm 0.5\%$ for $0.01 < T_9 < 1.0$ (Fig. 5.4) by the following analytical function:

$$\begin{aligned} R_{34} &= p_1 {T_9}^{-\frac{2}{3}} \exp(p_2 {T_9}^{-\frac{1}{3}}) \times \\ &\quad (1 + p_3 T_9 + p_4 T_9^2 + p_5 T_9^3 + p_6 T_9^4) \end{aligned} \tag{C.1}$$

$$\begin{aligned} p_1 &= 5.497 \times 10^6 \\ p_2 &= \text{-}1.281 \times 10^1 \\ p_3 &= \text{-}2.335 \times 10^{-1} \\ p_4 &= 5.108 \times 10^{-2} \\ p_5 &= \text{-}1.672 \times 10^{-3} \\ p_6 &= \text{-}4.724 \times 10^{-4} \end{aligned}$$

Table C.1: $^3\mathrm{He}(\alpha,\gamma)^7\mathrm{Be}$ reaction rate in $\mathrm{cm}^3\mathrm{s}^{-1}\mathrm{mole}^{-1}$.

T_9	Reaction rate	T_9	Reaction rate
0.001	1.339×10^{-47}	0.07	1.013×10^{-6}
0.002	2.475×10^{-36}	0.08	3.581×10^{-6}
0.003	7.147×10^{-31}	0.09	1.038×10^{-5}
0.004	1.975×10^{-27}	0.10	2.589×10^{-5}
0.005	5.518×10^{-25}	0.11	5.747×10^{-5}
0.006	4.040×10^{-23}	0.12	1.162×10^{-4}
0.007	1.243×10^{-21}	0.13	2.178×10^{-4}
0.008	2.096×10^{-20}	0.14	3.832×10^{-4}
0.009	2.279×10^{-19}	0.15	6.398×10^{-4}
0.010	1.778×10^{-18}	0.16	1.021×10^{-3}
0.011	1.071×10^{-17}	0.18	2.331×10^{-3}
0.012	5.240×10^{-17}	0.20	4.731×10^{-3}
0.013	2.166×10^{-16}	0.25	1.936×10^{-2}
0.014	7.789×10^{-16}	0.30	5.619×10^{-2}
0.015	2.490×10^{-15}	0.35	1.306×10^{-1}
0.016	7.203×10^{-15}	0.40	2.606×10^{-1}
0.018	4.712×10^{-14}	0.45	4.652×10^{-1}
0.020	2.372×10^{-13}	0.50	7.636×10^{-1}
0.025	6.018×10^{-12}	0.60	1.714×10^{0}
0.03	7.019×10^{-11}	0.70	3.243×10^{0}
0.04	2.515×10^{-9}	0.80	5.454×10^{0}
0.05	3.177×10^{-8}	0.90	8.422×10^{0}
0.06	2.184×10^{-7}	1.00	1.220×10^{1}

Appendix D

Certificate of the ^{22}Ne target gas

SIGMA-ALDRICH®

sigma-aldrich.com

3050 Spruce Street, Saint Louis, MO 63103, USA
Website: www.sigmaaldrich.com
Email USA: techserv@sial.com
Outside USA: eurtechserv@sial.com

Certificate of Analysis

Product Name:
Neon-^{22} Ne - 99.9 atom %, 99.995% (CP)

Product Number:	**601721**
Batch Number:	**MBBB0147V**
Brand:	ALDRICH
CAS Number:	13886-72-1
Formula:	22Ne
Formula Weight:	21.99 g/mol
Quality Release Date:	07 AUG 2013

^{22}Ne

Test	Specification	Result
Purity (GC)	≥ 99.995 %	99.999 %
Ar/O2		1.1 ppm
N2		0.2 ppm
CO		< 0.1 ppm
CO2		< 0.1 ppm
Hydrogen (H)		< 0.1 ppm
CH4+ C2H6		< 0.2 ppm
Mass Spectrometry	≥ 99.9	99.9

P. Sudhakar

Sudhakar Parthasarathy, Scientist
Quality Control
Miamisburg, Ohio US

Bibliography

[1] C. Iliadis, *Nuclear Physics of Stars* (Wiley-VCH Verlag GmbH, 2015), ISBN 9783527336487

[2] G. Gamow, Zeitschrift für Physik **51**, 204 (1928)

[3] C.E. Rolfs, W.S. Rodney, *Cauldrons in the Cosmos* (University of Chicago Press, 1988), ISBN 0226724573

[4] E.M. Burbidge, G.R. Burbidge, W.A. Fowler, F. Hoyle, Rev. Mod. Phys. **29**, 547 (1957)

[5] C.F. von Weizsäcker, Physikalische Zeitschrift **38**, 176 (1937)

[6] H.A. Bethe, C.L. Critchfield, Phys. Rev. **54**, 248 (1938)

[7] H.A. Bethe, Phys. Rev. **55**, 434 (1939)

[8] C.F. von Weizsäcker, Physikalische Zeitschrift **39**, 633 (1938)

[9] C.R. Rolfs, W.S. Rodney, Astrophys. J. Lett. **194**, L63 (1974)

[10] R.G. Gratton, E. Carretta, A. Bragaglia, Astron. Astrophys. Revs. **20**, 1 (2012)

[11] M.J. Cordero, C.A. Pilachowski, C.I. Johnson, E. Vesperini, The Astrophysical Journal **800**, 3 (2015)

[12] Carretta, E. et al., Astron. Astrophys. **505**, 117 (2009)

[13] Prantzos, N., Charbonnel, C., Iliadis, C., Astron. Astrophys. **470**, 179 (2007)

[14] P. Ventura et al., The Astrophysical Journal Letters **761**, L30 (2012)

[15] P. Ventura, M. Di Criscienzo, R. Carini, F. DAntona, Monthly Notices of the Royal Astronomical Society **431**, 3642 (2013)

[16] C.L. Doherty et al., Monthly Notices of the Royal Astronomical Society **437**, 195 (2014)

[17] Decressin, T. et al., Astron. Astrophys. **464**, 1029 (2007)

[18] P.A. Denissenkov et al., Monthly Notices of the Royal Astronomical Society **448**, 3314 (2015)

[19] de Mink, S. E., Pols, O. R., Langer, N., Izzard, R. G., Astron. Astrophys. **507**, L1 (2009)

[20] Garcia-Hernandez, D. A. et al., Astron. Astrophys. **555**, L3 (2013)

[21] C. Angulo et al., Nuclear Physics A **656**, 3 (1999)

[22] Izzard, R. G. et al., Astron. Astrophys. **466**, 641 (2007)

[23] A.L. Sallaska et al., Phys. Rev. Lett. **105**, 152501 (2010)

[24] D.D. Clayton, *Handbook of Isotopes in the Cosmos: Hydrogen to Gallium* (Cambridge University Press,, 2003), ISBN 0521823811

[25] C. Iliadis et al., The Astrophysical Journal Supplement Series **142**, 105 (2002)

[26] D.A. Chamulak, E.F. Brown, F.X. Timmes, K. Dupczak, The Astrophysical Journal **677**, 160 (2008)

[27] Parikh, A., José, J., Seitenzahl, I. R., Röpke, F. K., Astron. Astrophys. **557**, A3 (2013)

[28] M. Pignatari et al., The Astrophysical Journal Letters **808**, L43 (2015)

[29] J.R. Powers, H.T. Fortune, R. Middleton, O. Hansen, Phys. Rev. C **4**, 2030 (1971)

[30] S.E. Hale et al., Phys. Rev. C **65**, 015801 (2001)

[31] D.G. Jenkins et al., Phys. Rev. C **87**, 064301 (2013)

[32] R. Firestone, Nuclear Data Sheets **108**, 1 (2007)

[33] F. Cavanna et al. (The LUNA Collaboration), Phys. Rev. Lett. **115**, 252501 (2015)

[34] R. Depalo et al., Phys. Rev. C **92**, 045807 (2015)

[35] J. Görres et al., Nuclear Physics A **385**, 57 (1982)

[36] K.J. Kelly, Ph.D. thesis, University of North Carolina (2016)

[37] K.J. Kelly et al., Phys. Rev. C **95**, 015806 (2017)

[38] R. Depalo et al., Phys. Rev. C **94**, 055804 (2016)

[39] A.L. Sallaska et al., The Astrophysical Journal Supplement Series **207**, 18 (2013)

[40] J. Görres et al., Nuclear Physics A **408**, 372 (1983)

[41] C. Iliadis, R. Longland, A. Champagne, A. Coc, Nuclear Physics A **841**, 251 (2010)

[42] M. Meyer, J. Smit, Nuclear Physics A **205**, 177 (1973)

[43] P. Endt, Nuclear Physics A **521**, 1 (1990)

[44] K.J. Kelly, A.E. Champagne, R. Longland, M.Q. Buckner, Phys. Rev. C **92**, 035805 (2015)

[45] T. Szücs et al., The European Physical Journal A **51**, 33 (2015)

[46] A. Formicola et al., Nucl. Instr. Meth. Phys. Res. A **507**, 609 (2003)

[47] J. Görres, K. Kettner, H. Kräwinkel, C. Rolfs, Nucl. Instr. Meth. **177**, 295 (1980)

[48] D. Bemmerer et al., Nuclear Physics A **779**, 297 (2006)

[49] M. Marta et al., Nucl. Instr. Meth. Phys. Res. A **569**, 727 (2006)

[50] Cavanna, F. et al., Eur. Phys. J. A **50**, 179 (2014)

[51] J. Osborne et al., Nuclear Physics A **419**, 115 (1984)

[52] C. Casella et al., Nucl. Instr. Meth. Phys. Res. A **489**, 160 (2002)

[53] S. Agostinelli et al., Nucl. Instr. Meth. Phys. Res. A **506**, 250 (2003)

[54] W.A. Rolke, A.M. López, J. Conrad, Nucl. Instr. Meth. Phys. Res. A **551**, 493 (2005)

[55] R. Brun, F. Rademakers, Nucl. Instr. Meth. Phys. Res. A **389**, 81 (1997)

[56] J.F. Ziegler, M. Ziegler, J. Biersack, Nucl. Instr. Meth. Phys. Res. B **268**, 1818 (2010), 19th International Conference on Ion Beam Analysis

[57] M. Wiescher et al., Nuclear Physics A **349**, 165 (1980)

[58] H. Herndl et al., Phys. Rev. C **44**, R952 (1991)

[59] A. Terakawa et al., Phys. Rev. C **48**, 2775 (1993)

[60] F. Barker, Nuclear Physics A **637**, 576 (1998)

[61] H.J. Assenbaum, K. Langanke, C. Rolfs, Zeitschrift für Physik A Atomic Nuclei **327**, 461 (1987)

[62] D.D. Clayton, *Principles of stellar evolution and nucleosynthesis* (University of Chicago Press, 1983), ISBN 0226109534

[63] K.N. Huang et al., Atomic Data and Nuclear Data Tables **18**, 243 (1976)

[64] M. Ciocca, C.E. Burkhardt, J.J. Leventhal, T. Bergeman, Phys. Rev. A **45**, 4720 (1992)

[65] J.N. Bahcall, Nuclear Physics B - Proceedings Supplements **118**, 77 (2003)

[66] J.N. Bahcall, *Neutrino Astrophysics* (Cambridge University Press, 1989), ISBN 9780521379755

[67] R. Davis, Rev. Mod. Phys. **75**, 985 (2003)

[68] B. Aharmim et al. (SNO Collaboration), Phys. Rev. C **88**, 025501 (2013)

[69] M. Smy, Nucl. Phys. B **235236**, 49 (2013), the {XXV} International Conference on Neutrino Physics and Astrophysics

[70] G. Bellini et al. (Borexino Collaboration), Phys. Rev. D **89**, 112007 (2014)

[71] B.S.N. Singh, M. Hass, Y. Nir-El, G. Haquin, Phys. Rev. Lett. **93**, 262503 (2004)

[72] T.A.D. Brown et al., Phys. Rev. C **76**, 055801 (2007)

[73] A. Di Leva et al., Phys. Rev. Lett. **102**, 232502 (2009)

[74] M. Carmona-Gallardo et al., Phys. Rev. C **86**, 032801 (2012)

[75] C. Bordeanu et al., Nucl. Phys. A **908**, 1 (2013)

[76] A. Kontos et al., Phys. Rev. C **87**, 065804 (2013)

[77] D. Bemmerer et al. (LUNA Collaboration), Phys. Rev. Lett. **97**, 122502 (2006)

[78] H.D. Holmgren, R.L. Johnston, Phys. Rev. **113**, 1556 (1959)

[79] P.D. Parker, R.W. Kavanagh, Phys. Rev. **131**, 2578 (1963)

[80] K. Nagatani, M. Dwarakanath, D. Ashery, Nucl. Phys. A **128**, 325 (1969)

[81] H. Kräwinkel et al., Z. Phys. A **304**, 307 (1982)

[82] J.L. Osborne et al., Phys. Rev. Lett. **48**, 1664 (1982)

[83] T. Alexander et al., Nucl. Phys. A **8427**, 526 (1984)

[84] M. Hilgemeier et al., Zeitschrift für Physik A Atomic Nuclei **329**, 243 (1988)

[85] E.G. Adelberger et al., Rev. Mod. Phys. **83**, 195 (2011)

[86] T. Neff, Phys. Rev. Lett. **106**, 042502 (2011)

[87] R.H. Cyburt, B.D. Fields, K.A. Olive, Phys. Rev. D **69**, 123519 (2004)

[88] A. Serenelli, C. Peña Garay, W.C. Haxton, Phys. Rev. D **87**, 043001 (2013)

[89] N. Grevesse, A. Sauval, Space Science Reviews **85**, 161 (1998)

[90] M. Asplund, N. Grevesse, J. Sauval, P. Scott, Annu. Rev. Astron. Astroph. **47**, 481 (2009)

[91] A.M. Serenelli, S. Basu, J.W. Ferguson, M. Asplund, Astrophys. J. Lett. **705**, L123 (2009)

[92] A.M. Serenelli, W.C. Haxton, C. Peña-Garay, Astrophys. J. **743**, 24 (2011)

[93] G. Gyürky et al. (LUNA Collaboration), Phys. Rev. C **75**, 035805 (2007)

[94] F. Confortola et al. (LUNA Collaboration), Phys. Rev. C **75**, 065803 (2007)

[95] K.M. Nollett, Phys. Rev. C **63**, 054002 (2001)

[96] R.H. Cyburt, B. Davids, Phys. Rev. C **78**, 064614 (2008)

[97] M. Pospelov, J. Pradler, Annu. Rev. Nucl. Part. Sci. **60**, 539 (2010)

[98] M. Kusakabe, A. Balantekin, T. Kajino, Y. Pehlivan, Phys. Lett. B **718**, 704 (2013)

[99] A. Coc, J.P. Uzan, E. Vangioni, J. Cosmol. Astropart. Phys. **2014**, 050 (2014)

[100] K.M. Nollett, S. Burles, Phys. Rev. D **61**, 123505 (2000)

[101] T. Kajino, Nucl. Phys. A **460**, 559 (1986)

[102] T. Mertelmeier, H. Hofmann, Nucl. Phys. A **459**, 387 (1986)

[103] O. Pisanti et al., Comput. Phys. Commun. **178**, 956 (2008)

[104] M.S. Smith, L.H. Kawano, R.A. Malaney, Astrophys. J. Suppl. Ser. **85**, 219 (1993)

[105] Planck Collaboration et al., A&A **571**, A16 (2014)

[106] K. Olive, P.D. Group, Chin. Phys. C **38**, 090001 (2014)

[107] B.D. Fields, Annu. Rev. Nucl. Part. Sci. **61**, 47 (2011)

[108] E. Caffau et al., Nature **113**, 042501 (2011)

[109] M. Anders et al. (LUNA Collaboration), Phys. Rev. Lett. **113**, 042501 (2014)

[110] Y. Fukuda et al. (Super-Kamiokande Collaboration), Phys. Rev. Lett. **81**, 1562 (1998)

[111] Q.R. Ahmad et al. (SNO Collaboration), Phys. Rev. Lett. **87**, 071301 (2001)

[112] Q.R. Ahmad et al. (SNO Collaboration), Phys. Rev. Lett. **89**, 011301 (2002)

[113] B.W. Filippone, A.J. Elwyn, C.N. Davids, D.D. Koetke, Phys. Rev. C **28**, 2222 (1983)

[114] F. Hammache et al., Phys. Rev. Lett. **80**, 928 (1998)

[115] F. Hammache et al., Phys. Rev. Lett. **86**, 3985 (2001)

[116] F. Strieder et al., Nucl. Phys. A **696**, 219 (2001)

[117] L.T. Baby et al. (ISOLDE Collaboration), Phys. Rev. C **67**, 065805 (2003)

[118] L.T. Baby et al. (ISOLDE Collaboration), Phys. Rev. Lett. **90**, 022501 (2003)

[119] L.T. Baby et al. (the ISOLDE Collaboration), Phys. Rev. C **69**, 019902 (2004)

[120] A.R. Junghans et al., Phys. Rev. Lett. **88**, 041101 (2002)

[121] A.R. Junghans et al., Phys. Rev. C **68**, 065803 (2003)

[122] A.R. Junghans et al., Phys. Rev. C **81**, 012801 (2010)

[123] J.N. Bahcall, A. Ulmer, Phys. Rev. D **53**, 4202 (1996)

[124] W.C. Haxton, A.M. Serenelli, The Astrophysical Journal **687**, 678 (2008)

[125] P. Descouvemont, Phys. Rev. C **70**, 065802 (2004)

[126] G. Testera (Borexino Collaboration), talk at Topics in Astroparticle and Undergound Physics (TAUP2015), 7-11 September 2015, Torino, Italy

ERKLÄRUNG

Hiermit versichere ich, dass ich die vorliegende Arbeit ohne unzulässige Hilfe Dritter und ohne Benutzung anderer als der angegebenen Hilfsmittel angefertigt habe; die aus fremden Quellen direkt oder indirekt übernommenen Gedanken sind als solche kenntlich gemacht. Die Arbeit wurde bisher weder im Inland noch im Ausland in gleicher oder ähnlicher Form einer anderen Prüfungsbehörde vorgelegt.

Die vorliegende Arbeit wurde am Institut für Kern- und Teilchenphysik der Technische Universität Dresden und am Helmholtz-Zentrum Dresden-Rossendorf unter der wissenschaftlichen Leitung von Prof. Dr. Kai Zuber und PD Dr. Daniel Bemmerer angefertigt. Ich versichere, dass es keine frühere erfolglose Promotionsverfahren gab.

Mit dem Einreichen an der Fakultät Mathematik und Naturwissenschaften der Technischen Universität Dresden erkenne ich die bestehende Promotionsordnung vom 23.02.2011 an.

Marcell Péter Takács
Dresden, 24. April 2017

HZDR
HELMHOLTZ
ZENTRUM DRESDEN
ROSSENDORF

Bautzner Landstr. 400
01328 Dresden, Germany
Tel. +49 351 260-3581
Fax +49 351 260-13581
d.bemmerer@hzdr.de
http://www.hzdr.de